Ultra-Lightweight Nanorelief Networks:

Photopatterned Microframes

by

Taeyi Choi

B.S. School of Materials Science and Engineering
Korea Advanced Institute of Science and Technology, 2002

Submitted to the Department of Materials Science and Engineering
in Partial Fulfillment of the Requirements for the Degree of
Doctor of Philosophy in Polymers
at the
Massachusetts Institute of Technology
September, 2007

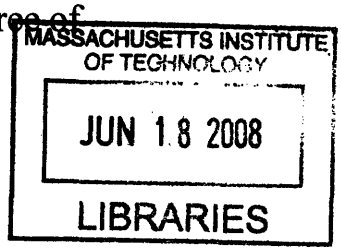

Signature of Author.....
Department of Materials Science and Engineering
June 29th, 2007

Certified by.....
Edwin L. Thomas
Morris Cohen Professor of Materials Science and Engineering
Head of Department in Materials Science and Engineering
Thesis Advisor

Accepted by.....
Samuel M.Allen
POSCO Professor of Physical Metallurgy
Chair, Departmental Committee on Graduate Studies

Ultra-Lightweight Nanorelief Networks: Photopatterned Microframes

by

Taeyi Choi

Submitted to the Department of Materials Science and Engineering on June 29th, 2007 in Partial Fulfillment of the Requirements for the Degree of Doctor of Philosophy in Polymers

Abstract

Lightweight nano-network structures in polymers have been fabricated and investigated for their mechanical properties. Fabrication techniques via holographic interference lithography and phase mask lithography were implemented for periodic and quasiperiodic bicontinuous polymer-air structures on the submicrometer length scale. For 3D quasiperiodically nanostructured materials, quasicrystalline phase mask lithography utilizing 2D quasiperiodic phase mask was successfully employed. 2D hexagonal arrays of air cylinders in SU8 polymer films and 3D four-beam connected (3- $R\bar{3}m$) and octagonal quasicrystalline SU8 films were fabricated and analyzed in this thesis.

For investigating the mechanical properties of various nano-network structures, three different methods of mechanical characterization were applied. Atomic force microscopy with its nanometer scale resolution was adopted to conduct force measurements to probe local elastic properties of the sample. Templated by the light intensity distribution from three-beam interference, the spatial distribution of elastic modulus was observed in the pattern of 2D hexagonal air-cylinder and a uniform SU8 polymer film by AFM nanoindentation. A second method for mechanical characterization, the microtensile tester enabled us to evaluate a symmetry effect on the elastic and plastic properties of the polymer fibers and thin films. Large plastic deformation of 200nm-diameter struts comprising the 3D periodic and quasiperiodic microframes of the normal brittle bulk polymer was discovered and is an example of length-scale dependent mechanical behavior. Crack propagation and energy absorption were guided along the symmetry directions in the periodic structures. However, there was found no preferred direction of crack propagation in quasicrystalline nanostructures due to the absence of translational symmetry. The third method, Brillouin light scattering (BLS) allowed estimation of the phonon properties in the structured films and the associated mechanical properties. The BLS measurements also confirmed the isotropy of modulus with the symmetry of the structures.

The length scale dependence, the effect of structural symmetry and the processing dependence of the mechanical behavior of the various nanostructures in SU8 polymer films were observed. The hundred-nanometer length scale of 3D nanostructures induces plastic deformation of struts under an applied force, which makes the film tougher and energy absorbing. The symmetry of the structured films determines the preferred

direction of crack propagation and following fracture behavior. Octagonal-patterned (*8mm*) quasicrystalline films via quasicrystalline phase mask lithography (QCPML) exhibit higher specific toughness and fracture strength with the unit mass than uniform solid films.

Thesis supervisor: Edwin L. Thomas
Title: Department Head of Materials Science and Engineering and Morris Cohen Professor of Materials Science and Engineering

Acknowledgement

First of all, I would like to thank professor Ned Thomas, my wonderful advisor, for his insight, inspiration and enthusiasm on learning and understanding science. Having an advisor like professor Thomas is such a blessing in my graduate life. I am very thankful to professor Van Vliet and professor Roylance in my thesis committee for their valuable comments, suggestions and guidance during my Ph.D. study.

I give thanks to my great colleagues: Dr. Ji-Hyun Jang for her excellence and diligence for research. Without her consistent help, I would have not been able to experience the art of interference lithography. Thanks to Dr. Ion Bita, I learned about the quasicrystals and phase mask lithography, which opened my eyes wide. I would like to thank Taras Gorishnyy and CheongYang (Henry) Koh for not only collaboration of BLS measurements but also enriching my MIT life by hanging out with them. I thank Dr. Chaitanya Ullal for his patience when I first stepped in the area of interference lithography. I give my thanks to professor Tsukruk and Dr. Melbs LeMieux for teaching me how to do AFM nanoindentation. I thank Dr. Lifeng Wang and professor Mary Boyce for their great micromechanical modeling which demonstrated and explained so well our observations and guided us how to interpret them. I thank Dr. Steve Kooi for his diligent and humble guidance and help on every instrument at the

Institute for Soldier Nanotechnologies. Give thanks to all ELT group members: Woosoo, Jongseung, Joe, Raf, Nick, Cheng-yen, Rachel, Naan, and far more great researchers!

I would love to thank Rev. Tae Whan Kim for his consistent supports, encouragements and prayers for me during last five years. Without his powerful messages and prayers, I could not finish this study. I thank pastor David Choi for his guidance and caring; he has been a great mentor for me. I thank Meekyung, Soonmin and all my friends in love and grace of God, thank them for their warm cares and love.

My parents, my sister and new brother-in-law, I thank them for their unchanging love, trust and happiness in the famly. My love and husband (in three days!), Dongeung Kim, I thank him for his understanding, encouragement and love. Without him, I can't imagine how I could have lived at MIT and in Boston.

Above all, all the glories and blessings to my Heavenly Father, my one and only Savior and Lord, Jesus Christ.

By the grace of God I am what I am.

Soli Deo Gloria.

Table of Contents

List of Figures

promote cationic polymerization of crosslinked network, (d) Developing and drying (supercritical CO_2 drying in some cases). After the procedure, hardbaking is done for certain investigations.

Figure 2-10. A few SU8 microstructures fabricated via IL. (a) The three-term level set diamond-like structure, 3-$R\bar{3}m$ made by the exposure of the four beam interference pattern in SU8. View: off the threefold axis. Refraction of the incident beams is compensated for by using the index-matched prism configuration shown in the inset; (b) The same 3-$R\bar{3}m$ structure from plan view (see details in chapter 4); (c) P structure from the view of [111] axis and (d) 2D periodic biomimetic microlens arrays with hexagonal air cylinders.

Figure 2-11. (a) Lloyd's mirror interference lithography setup and (b) Controlling the period of the recorded fringes by rotating the sample holder with regard to the incoming beam direction. (c) Fabrication process for 2D QC PDMS phase masks. PR = photoresist, BARL = bottom antireflection layer. These setup and experiments were done in Nano Structure Laboratory of professor H.I. Smith in the Department of Electrical Engineering and Computer Science, MIT.

Figure 2-12. Schematic illustration of procedures for using a conformable and elastomeric phase mask to produce 3D quasicrystalline nanostructures: 2D octagonal QC phase mask and cross-section of 3D QC nanostructures.

Figure 2-13. Schematic force-distance curve in the approaching-retracting mode with the cantilever shapes: (a) Approach, (b) Jump into contact with jump-in point (A), (c) Load with deflection, (d) Unload and (e) Jump-off contact with pull-off point (B).

geometry the phonon wave vector does not depend on the refractive index of the sample.

Figure 3-1. Stress-strain curves for SU8 film at different stages of processing.[1] The free standing samples peeled off from the substrate were tested under a tensile force. Without the post-exposure bake, SU8 glassy monomer film exhibits a fairly large strain at fracture (~30%). With post-exposure bake and hardbake, the film becomes stiffer and more brittle.

Figure 3-2. . 2D light intensity distribution for three-beam interference used for the fabrication of the patterned specimen along with primary lattice vectors for corresponding 2D lattice; **N** stands for the regions of nodes having highest-intensity and **B** stands for the regions of beams having slightly lower intensity than nodes (see Figure 3-5).

Figure 3-3. AFM data for uncured SU8 film: (a) AFM topography image with 0.3 nm RMS roughness. A white spot in the lower left is a dirt particle. (b) The surface distribution of the elastic modulus from 16x16 force measurements (3x3 μm^2). (c) The histogram of the elastic modulus distribution.

Figure 3-4. AFM data for cured SU8 film: (a) AFM topography image with 0.9nm RMS roughness. (b) The surface distribution of the elastic modulus from 16x16 force measurements (2x2 μm^2). (c) The histogram of the elastic modulus distribution.

Figure 3-5. (a) 2D light intensity distribution for three-beam IL used for the fabrication of the patterned specimen along with (inset) primary lattice vectors for corresponding 2D lattice; **B** and **N** stand for regions of beams and nodes of lattice. (b) Scanning electron microscopy (SEM) image shows long-range ordered 2D hexagonal lattice; (c) One-dimensional light intensity distribution

normal to the (0001) plane of the microframe structure. The colors correspond to struts at c/3, 2c/3and c. (c) Views normal to the (1 1 $\bar{2}$ 0) and (1 0 $\bar{1}$ 0) planes of the microframe structure. (d) Perspective view of the structure with the basic four-functional element as the inset. The sub cell dimensions are ~ 1400 nm x 1000 nm x 870 nm. The three thinner struts have a diameter about 200 nm and length of 640 nm and the thicker vertical post has a diameter of 500 nm and length of 1100 nm. (e) SEM image of the 3D-microframe fabricated in SU8. The insets show magnified views of the top (lower right) and cross sectional (upper right) surfaces corresponding to the schematic views in b and c.

Figure 4-2. SEM images of fracture within the polymer microframe. (a) Region where cracks are guided by planes of easy fracture. (b) View showing a region with intersecting {1 1 $\bar{2}$ 0} facets with an apex angle of 60 degrees. (c) Region where surface-initiated cracks penetrate towards the substrate.

Figure 4-3. SEM images of the microframe structure showing plastic deformation. (a) Area with a microframe bridge extending from one side of a crack to the other. The inset shows extensive shear, bending and microplastic deformation of the structure near the left terminus of the bridge. (b) Evidence of tensile deformation and fracture of transverse struts with up to several hundred % strain (e.g. circled strut) in the vicinity of a crack. The local strain can be estimated based on the departure of the strut and node pattern from the initial undeformed unit cell structure (right side of image). (c) Portion of film that was compressed, showing the collapsed microframe region at left. (d) (left) Cross section of a region of the film where the structure has been plastically deformed. (right) Fibrils formed

due to peeling of microframe from substrate. (e) Schematic depicting how long fibrils form via stretch-alignment of vertical and transverse struts.

Figure 4-4. (a) A Representative Volume Element (in the center box) of the 3D microframe for applying 2D micromechanical model with periodic boundary conditions under multiaxial loading. (b) The predicted deformation under a tension along the thick post direction (0°). (c) The predicted deformation under a tension along the perpendicular to the thick post (90°). (d) The predicted deformation under a compression explains the observed SEM micrograph with the many deformed RVEs. (e) Applying shear to the RVE represents the deformation of elongated fibrils. Arrows in each figure show the loading direction. Modeling conducted by Dr. Lifeng Wang in professor Mary C. Boyce in mechanical engineering at MIT.

Figure 4-5. SEM micrographs of multiaxial loading on the 3D periodic microframe; most of predicted deformations from 2D micromechanical modeling were observed in a single SEM image. (a) In this SEM image SU8 microframe exhibits strut-stretching and contraction after break (black circles), penny-shape crack formation (white ellipses) where has extended, broken, bent and contracted struts, neck-forming (white circles and ellipses) by overall tension. (b) Compression, shear (black circles) and residual pillars adhered to the substrate were shown in the SEM micrograph.

Figure 5-1. (a) SEM image of a 2D octagonal quasiperiodic PDMS phase mask, and (b) corresponding diffraction pattern produced by a laser beam (355nm) at normal incidence. (c) Cross-sectional SEM image of the 3D nanostructured quasiperiodic scaffold recorded in SU-8 by an expanded, flat-top 364nm laser

beam passing through the phase mask in (a), and (d) corresponding plane-view SEM of its surface. Yellow box in (d) shows the diffraction pattern of the *~1x2cm* size 3D QC. (e) Magnified area from (d), showing sub-surface structured details. The red lines in the structure represent 3-connected or 4-connected at nodes in plane.

Figure 5-2. Confocal microscopy images of the 3D quasiperiodic SU8 scaffold shown in Figure 5-1(d) taken in fluorescent mode using a 488nm Ar-ion laser. Brighter regions correspond to air channels in the original SU-8 structure. The octagonal quasicrystalline symmetry is preserved throughout the thickness of the structured film. The plan-view SEM picture of the SU8 scaffold surface is given as a reference for the $z = 0$ location.

Figure 5-3. The computation of diffraction efficiencies in a set of 2D gratings for the octagonal QC structure from the 2D octagonal phase mask which has 300nm periodicity, 60% volume faction with 364 nm exposure wavelength and the refractive index of 1.62 from SU8. (a) SEM micrograph of QC structure. (b) The calculated model corresponds very well with the resultant structure in the SEM. (c) The top half of the structure in plane at -0.5 μm. (d) The bottom half of the structure which is staggered to the top layer at -4.0 μm. (e) The top layer (blue) and the bottom layer (yellow) shown at the same time of z range from -0.5 μm to -4.0 μm. Courtesy of CheongYang Koh. (DMSE, MIT).

Figure 5-4. (a) BLS measurements were conducted with six different orientations of an azymuthal angle (φ) in plane from 0 (on a mirror axis) to 22.5° counter-clockwise at a fixed wave vector, k. (b) BLS spectrum taken at 24 ° for the k

scattering angle (k = 4.9 μm^{-1}) and 0° orientation shows peaks from SU8 QC structure (at f =1.79 GHz) and from glass (at f = 4.52 GHz).

Figure 5-5 (a) Plot of frequency dispersion measured in six different orientations in plane (0°, 5°, 10°, 15°, 20° and 22.5°) at three different scattering angles (20°, 24° and 28°), which provide sufficient information for all directions associated with 8-fold rotational symmetry. The slopes represent the sound velocity in glass (upper line) and in SU8 QC PEB film (lower line): the average sound velocity in SU8 QC PEB film is 2300 m/s. (b) Azimuthal plot of sound velocity of SU8 QC PEB film. With the proportional relationship between the sound velocity and the modulus, this plot shows the isotropy of the in-plane modulus in the SU8 QC structure. Using the measurements from 6 directions, the other values are replicated by applying rotational symmetry.

Figure 5-6. Stress-strain curves of freestanding polymer films from the micro-tensile testing. Black curves: uniform SU8 5.5 μm-thick films. The three nearly linear curves show brittle fracture with elastic properties having average E = 1.72±0.27 GPa and toughness = 0.96±0.10 MPa. Red curves: SU8 octagonal QC films of polymer-air composite have average E = 0.85±0.13 GPa and toughness = 0.98±0.56 MPa.

Figure 5-7. DMA curve of SU8 unstructured film with heating rate of 3 °C/min at frequency 1 Hz. The storage modulus is 1.65 GPa at room temperature (green curve) and the glass transition temperature is about 200 °C from the peak of tan delta (brown curve). Multiple DMA scans were conducted and values are similar with a narrow range.

Figure 5-8. BLS spectra (frequency vs intensity) at a fixed scattering angle and an orientation show phonon peaks from SU8 QC structures shift from 1.79 GHz (PEB only, green) to 2.18 GHz (PEB+HB, red). This shows the increase in the elastic modulus by hardbaking SU8 QC film.

Figure 5-9. (a) Plot of frequency dispersion measured in five different angles (0°, 5°, 10°, 15° and 20°), which provide sufficient information for all directions associated with 8-fold rotational symmetry. The slopes represent the sound velocity in glass (upper) and in SU8 QC hardbaked film (lower): the average sound velocity in SU8 QC HB film is 2950 m/s. (b) Plot of sound velocity of SU8 QC PEB film (black) and SU8 QC PEB+HB film (blue). The average velocity of SU8 QC PEB film is 2300 m/s and the velocity of SU8 QC PEB+HB film is 2950 m/s. The associated bulk moduli for QC film without hardbaking and with hardbaking are 6.07 GPa and 10.0 GPa, respectively.

Figure 5-10. Stress-strain curves of freestanding SU8 films from the micro-tensile testing. Black curves represent the mechanical behavior of SU8 unstructured films. SU8 octagonal QC PEB films in red curves have E = 0.85±0.13 GPa and toughness = 0.98±0.56 MPa. (b) SU8 octagonal QC PEB+HB films have E = 0.41±0.11 GPa and toughness= 2.92±1.52 MPa.

Figure 5-11. SEM plan-view micrographs of fracture surfaces in (a-e) SU8 QC PEB+HB films by microtensile testing and (f) QC PEB only films deformed by peel test. Red arrows show the direction of crack propagation. (a-b) Crack propagation from the fracture surface with the absence of translational symmetry, (c) Crack stoppage (upper) with the propagation direction by red arrows from the fracture surface and initiation of another crack (down) near the stopped crack.

(d-f) Substantial plastic deformation of thin struts in the structure: (d) and (e) deformed by tensile testing and (f) deformed by complicated force from sticky tape peeling.

Figure 5-12. SEM micrographs of the side-view of fracture surfaces in SU8 thin films by tensile testing. (a-b) Fracture surfaces of unstructured SU8 films. The surfaces show brittle fracture with no significant plastic deformation. (c-e) Fracture surfaces of SU8 QC PEB+HB films exhibiting elongated struts comprising the pattern. Comparing struts A and B from (e), the elongated strut B is longer than stretched strut A by 330 %. This quantitative extension ratio represents the large deformation takes place under the deformation in microscopic ranges. The delamination between the structured film and thin solid buffer layer is also observed in (d-e).

Figure 6-1. (a) The deformation under a tension of a Representative Volume Element (RVE) of the 3D periodic microframe by 3D micromechanical model. (b) The deformation under a shear of an RVE by 3D micromechanical model. Dashed circles in each figure show the size reduction of thin struts by elongation. The thinning and break of the struts might cause the localization of deformation and macroscopic brittle behavior. In strut deformation, red indicates materials deforming and blue indicates material not deforming. Modeling done by Dr. Lifeng Wang in Professor Mary C. Boyce group in mechanical engineering at MIT.

Figure 6-2. (a) 2D quasiperiodic PDMS phase mask with 60% volume fraction. (b) 2D quasiperiodic PDMS phase mask with 70% volume fraction. (c) 3D octagonal QC structure fabricated via quasicrystalline phase mask lithography (QCPML)

List of Tables

Chapter 1. Thesis Overview

We are familiar with truss structures[1] in bridges and buildings on a large scale and in certain animal exoskeletons on a microscopic scale for lightweight and strong materials. From what we know about the characteristics of truss structures, we expect that such nano-scale structures in thin films will affect the mechanical properties.

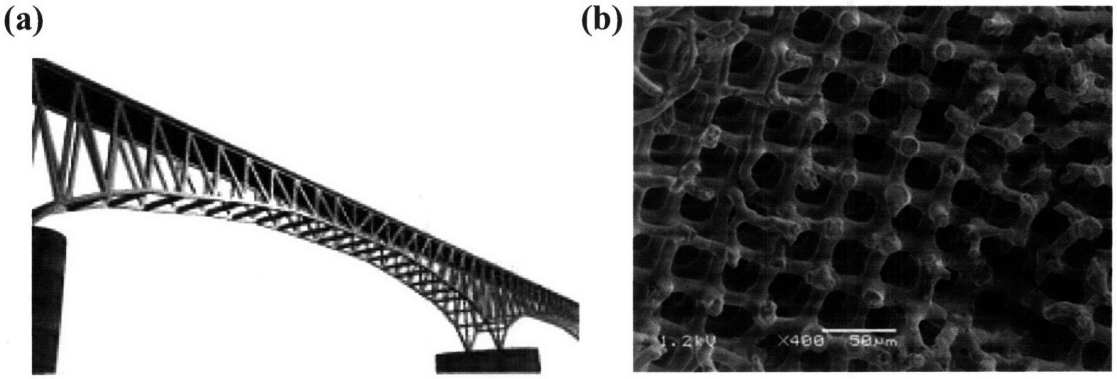

Figure 1-1. (a) Creating optimized models of truss structures.[1] Truss structures are composed of straight struts forming a set of triangular units for various load-bearing applications. (b) An SEM micrograph of the exoskeletons of a sea urchin (e.g. cidaris cidaris) exhibiting 6 strut-connectivity at a node point.

In this thesis, structures with sub-micrometer length scales will be investigated in terms of the elastic modulus, plasticity and toughness. There are two main issues explored in this thesis: (1) *methods to fabricate* nano-network structures and (2) *characterization of the mechanical properties* of the nano-network structures in terms of their elastic, plastic and fracture properties.

Chapter 2 discusses the background theories and experimental methods for creation of microtrusses, the fabrication tools for nano-network structures such as

holographic interference lithography (IL) and phase mask lithography (PML), the mechanical testing methods of nanoindentation using Atomic Force Microscopy (AFM) for local mechanical properties, microtensile testing and Brillouin Light Scattering (BLS) for the properties of polymer structures as a whole.

In Chapter 3, a two-dimensional (2D) hexagonal air-cylinder and polymer structure of SU8 made by three-beam IL was examined via AFM for local elastic properties. The intensity pattern from the interference of three beams and the corresponding crosslink density determine the spatial distribution of elastic modulus in the pattern. The measured moduli vary between locations within the structure. Such non-uniform elastic modulus via systematic variation of crosslink density suggests that the intensity-dependent approach could be utilized for designing a deformation path along the less stiff regions for certain applications. In terms of large strain behavior of the air-cylinder and polymer structure, the SU8 nanostructured films are capable of high plastic behavior with significant local deformation of individual cells and large scale deformation of the whole net. We can speculate that precise control of the non-uniform internal elastic properties within IL-microfabricated polymer structures makes these structures highly deformable and opens potential paths for photopatterned polymeric materials with efficient energy absorption on a submicrometer scale. Chapter 3 is based

on a publication done in collaboration with Dr. Ji-Hyun Jang, Dr. Chaitanya K. Ullal, Dr. Melburne C. LeMieux and Professor Vladimir V. Tsukruk at Georgia Institute of Technology, and appeared in *Adv. Func. Mater.* **16**, 1324-1330 (2006).[2]

In Chapter 4 the length scale dependent mechanical behavior with intermediate crosslink density is demonstrated for a SU8 3D periodic microframe fabricated by four-beam IL. This microframe structure is composed of three thin beams and one thick post and has a polymer volume fraction of ~ 0.3. The symmetry of the microframe guides crack propagation. Moreover, the thin struts exhibit very high (~300%) plastic deformation compared to the brittle behavior ($\varepsilon_f \leq 10$ %) in bulk SU8. The applied force for this behavior is complicated from the peeling of a sticky tape on the structure. The 2D and 3D micromechanical modeling predicts the deformation behavior of the microframe under multiaxial loading and the modeling results of tension, compression and shear well correspond to the deformation behavior observed in SEM micrographs. In order to understand fundamental mechanics of nanostructured films, there is a need to develop systematic mechanical testing for thin films and to make freestanding films. Chapter 4 is based on a publication done in collaboration with Dr. Ji-Hyun Jang, Dr. Chaitanya K. Ullal, Dr. Melburne C. LeMieux and Professor Vladimir V. Tsukruk at Georgia Institute of Technology, and appeared in *Adv. Mater.* **18**, 2123-2127 (2006).[3]

In Chapter 5, we fabricated 3D octagonally quasicrystalline (QC) films by quasicrystalline phase mask lithography (QCPML) utilizing 2D octagonal QC phase mask, and inspected the unusual mechanical behavior of energy propagation and absorption from microtensile testing. The struts in the QC films are deformed to several hundred-percent strain as in the 3D periodic microframe. Explaining a highly local plastic deformation (~300 %) but macroscopic brittle behavior (up to 20 %), we speculate that the localization of deformation takes place due to the small diameter of struts range of 100-400nm. In addition, due to the complicated geometry of quasicrystals, the tremendous plastic deformation on small scales does not induce large macroscopic plastic behavior. BLS measurements on the octagonal QC structure show the isotropic in-plane elastic modulus which is expected from the theory.[4] Fabrication of 3D QC nanostructured films in Chapter 5 is based on a publication done in collaboration with Dr. Ion Bita, Dr. Michael E. Walsh and Professor Henry I. Smith at Massachusetts Institute of Technology, and appeared in *Adv. Mater.* **19**, 1403-1407 (2007).[5] Mechanical characterization of 3D QC films is based on another publication in preparation.[6]

In Chapter 6 we summarize the accomplishments and conclude with remarks and future work from what we have learned in the dissertation. Small strain behavior

with the elastic modulus and large strain behavior of plasticity and crack propagation are summarized with the previous investigations such as submicron-sized feature size dependent mechanical behavior and the symmetry effects compared to observations on bulk SU8 polymer. By the microtensile testing for examining thin film properties, the stress-strain curves of the structured polymer films give us insights for the elastic and plastic mechanical behavior of the 3D nanostructured scaffolds.

1.1 References

1. Smith, J., Hodgins, J., Oppenheim, I. and Witkin, A., "Creating Models of Truss Structures with Optimization", *ACM Trans. Graph.* **21**, 295-301 (2002).
2. Choi, T., Jang, J. H., Ullal, C. K., LeMieux, M. C., Tsukruk, V. V. and Thomas, E. L., "The elastic properties and plastic behavior of two-dimensional polymer structures fabricated by laser interference lithography", *Adv. Funct. Mater.* **16**, 1324-1330 (2006).
3. Jang, J. H., Ullal, C. K., Choi, T. Y., Lemieux, M. C., Tsukruk, V. V. and Thomas, E. L., "3D polymer microframes that exploit length-scale-dependent mechanical behavior", *Adv. Mater.* **18**, 2123-+ (2006).
4. Christensen, R. M., "Sufficient Symmetry Conditions for Isotropy of the Elastic-Moduli Tensor", *J. Appl. Mech.-Trans. ASME* **54**, 772-777 (1987).
5. Bita, I., Choi, T., Walsh, M. E., Smith, H. I. and Thomas, E. L., "Large Area 3D nanostructures with Octagonal Quaasicrystalline Symmetry via Phase Mask Lithography", *Adv. Mater.* **19**, 1403-1407 (2007).
6. Choi, T., Bita, I., Koh, C. Y. Gorishnyy, T., Thomas, E.L., "Novel deformation behavior in the polymeric quasicrystalline structures with their disorder", *in preparation* (2007).

Chapter 2. Background of Experimental Methods

In this chapter we discuss the background theories and experimental methods for creation of microtrusses, the fabrication techniques for nano-network structures such as holographic interference lithography (IL) and phase mask lithography (PML), the mechanical testing methods of nanoindentation using Atomic Force Microscopy (AFM) for local mechanical properties, microtensile testing and Brillouin Light Scattering (BLS) for the properties of polymer structures as a whole.

2.1 Microtrusses: Structure-Property Relationship

Lightweight materials are important for a member of applications: load-sustaining structures of unmanned aerial vehicles (UAVs), satellites, fuel-efficient vehicles, body armor for protecting soldiers, packaging foams, thermal and electronic insulators and so on. Considering the competing factors of performance and manufacturing cost with lightness, topology is a crucial element to optimize for obtaining lightweight structures with outstanding mechanical properties.[1] Lightweight structures consist of stiff load bearing connections made using as little material as possible. Depending on how the connected struts are structured and how they behave under the load, the lattice-structured (beam-connected) materials are categorized into

two different types, bending-dominated and stretch-dominated[2] (See Fig. 2-1). A **truss** is defined as a static framework of rigid members pin-jointed into triangular units with axial forces only, which is another name of a stretch-dominated structure.[3]

When the structure is connected with b struts and j frictionless joints, according to Maxwell's stability criterion the structure is determined to be bending-dominated or stretch-dominated. Maxwell's stability criterion, M is described as $M = b - 2j + 3$ in

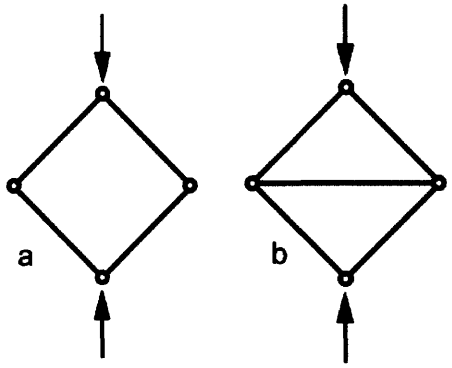

Figure 2-1. (a) A *mechanism* in 2D: in compression, the struts rotate (if the joints are not frozen) or bend (if they are frozen); (b) A *structure* in 2D: in compression the struts are either in tensile load or compressive load[2].

two-dimensional (2D) space and $M = b - 3j + 6$ in three-dimensional (3D) space where the sign of M determines whether the structures are bending-dominated under the deformation ($M < 0$) (Fig. 2-1(a)); or they are stretch-dominated ($M \geq 0$) (Fig. 2-1(b)).[2, 4]

In 3D, the stretch-dominated structures satisfying Maxwell's stability criterion are the tetrahedron and the octahedron shown in Figure 2-2. By itself each structure

cannot fill 3D space but their combination fills space. The necessary and sufficient condition for stretch-dominated structures in 3D space is that the connectivity should be 12. The 12 nearest neighbors in the face centered cubic (fcc) structure lie along <110> directions and the octet-truss lattice is shown in Figure 2-3.[5]

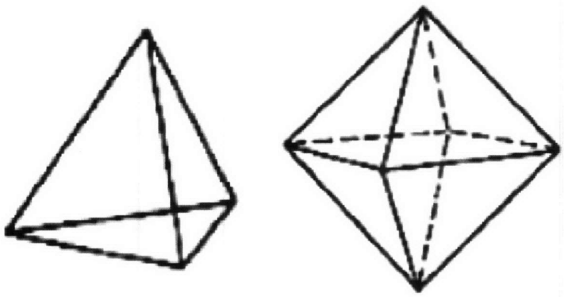

Figure 2-2. Three-dimensional cells that satisfy the Maxwell's criterion for stretch-dominated structures: tetrahedron (left) and octahedron (right).[2]

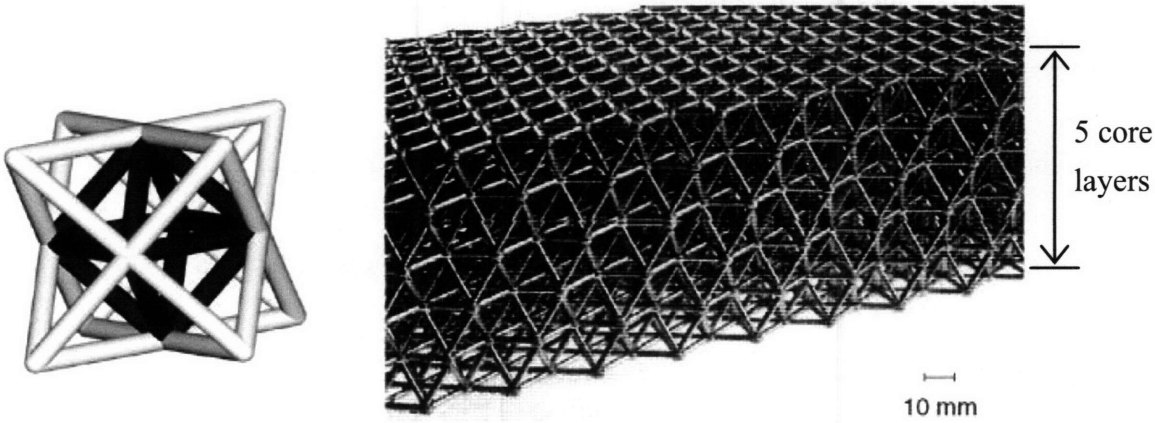

Figure 2-3. A unit structure of octet-truss lattice material with M > 0 (left). Photograph of the octet-truss lattice material made from a cast aluminum alloy: five tetrahedral core layers separated by triangulated layers. Triangulated layers and tetrahedral cores were injection-molded in polystyrene and then the octet-truss structure was constructed by adhering triangulated layers with alternating layers of tetrahedral core. This polystyrene lattice was used as a template to produce the cast aluminum alloy lattice in a "lost-wax" investment casting process. (Right).[5]

The relative modulus $\tilde{E}$ ($\frac{E_{cell}}{E_{bulk}}$) and the relative initial collapse strength $\tilde{\sigma}$ ($\frac{\sigma_{cell}}{\sigma_{bulk}}$) according to the relative density are described in log-log graphs in Figure 2-4(a) and 2-4(b), respectively.[6, 7] For example at a relative density of 10 %, $\tilde{E}$ of the stretch-dominated structure is one order of magnitude higher than $\tilde{E}$ of bending-dominated structures. As shown in Figure 2-4, the stretch-dominated structures are superior to bending-dominated structures in terms of stiffness and strength per unit weight. The details of analytic equations for both bending-dominated and stretch-dominated structures are given in Appendix 7.1. The relative density $\tilde{\rho}$ of the structures we have made in this thesis ranges from 0.3 to 0.75: $\tilde{\rho}$ = 0.3 for 3D periodic microframe, 3-$R\bar{3}m$ (in chapter 4), approximately $\tilde{\rho}$ = 0.55 for octagonal quasicrystalline structure (in chapter 5) and $\tilde{\rho}$ = 0.75 for 2d hexagonal lattice (in chapter 3). In the following chapters we will analyze the mechanical behavior of various structures having different relative density and symmetries.

Contrary to their substantial stiffness and strength, stretch-dominated structures undergo a dramatic softening after yield, which makes them less attractive for energy absorption properties in compression (Fig. 2-5). Depending on the application, the bending-dominated structures are interesting with their low modulus and stiffness but large strain at fracture advantageous for applications such as cushioning or packaging,

on the other hand, the stretch-dominated structures are best for applications requiring high stiffness and high strength at low weight.[2, 4]

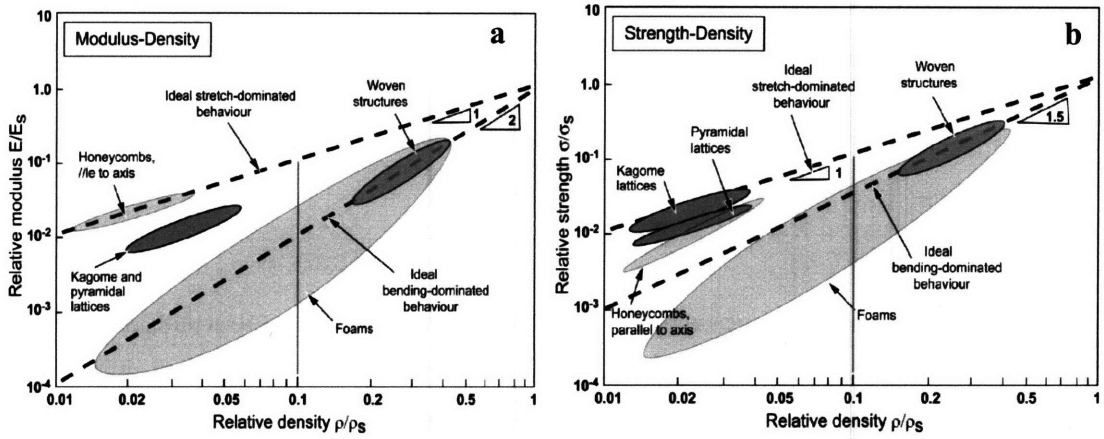

Figure 2-4. (a) Plot of relative modulus against relative density for cellular structures with different topologies on logarithmic scales. The bending dominated behavior has a slope of 2 and the stretch-dominated a slope of 1.[6] (b) Plot of relative initial collapse strength against relative density for cellular structure with different topologies on logarithmic scales. The bending dominated behavior has a slope of 1.5 and the stretch-dominated a slope of 1.[6] The orange line in (a) shows that at a relative density of 10 %, $\widetilde{E}$ of the stretch-dominated structure is 10 times larger than $\widetilde{E}$ of the bending-dominated. The orange line in (b) shows that at a relative density of 10 %, $\widetilde{\sigma}$ of the stretch-dominated is more than 5 times larger than $\widetilde{\sigma}$ of the bending-dominated.

Having known the mechanical behavior of macroscopic truss structures typically made of metal alloys,[1, 8-11] for metal structures on a millimeter length scale, the stress/strain behavior of bulk metals from the constitutive equations of macromechanics is perfectly adequate to capture the actual deformation behavior of the geometry of structures. However, for polymer structures on a submicron scale we need to discover the stress/strain behavior which is not always same with that of bulk polymers.

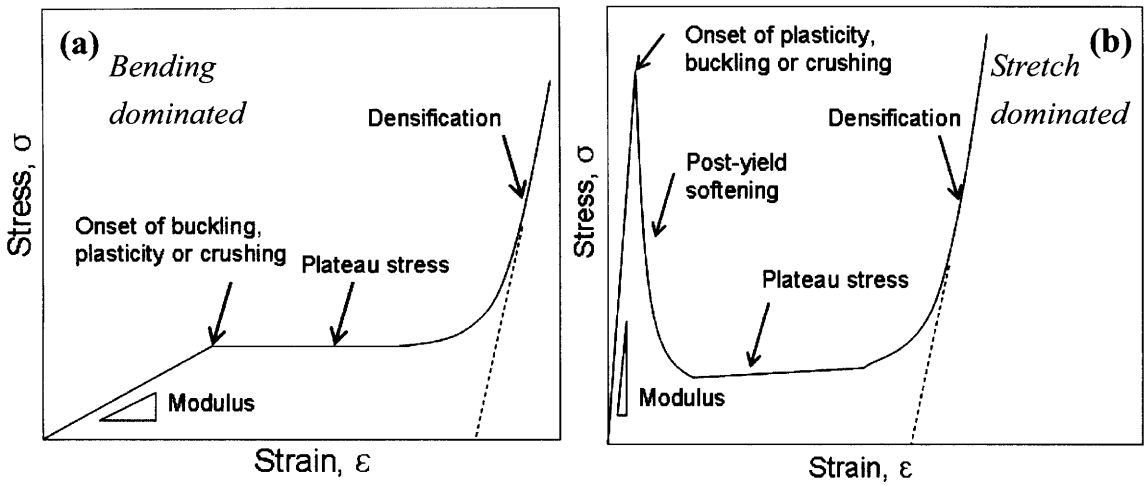

Figure 2-5. (a) Schematic compressive stress-strain curve showing important parameters for a bending-dominated structure.[6] (b) Schematic compressive stress-strain curve of a stretch-dominated structure, showing important parameters,[6] assuming the relative density of both structures is 0.3.

One example of designed-in failure is the crumple zone of the automobile as in Figure 2-6. A crumple zone built into the front and rear of the vehicle is designed to absorb the impact of a collision and to protect passengers inside the vehicle by undergoing extensive plastic deformation. Crumple zones are designed into the actual frame of the automobile, creating a point for the frame to *buckle* when subjected to extreme stress. These crumple zones yield during impact, redirecting the energy of the collision and often reducing the chance of injury to the driver.[12] There are also other parts for auto safety; the survival cell that maintains its original shape despite impact, and the side impact bar that prevents passengers from being ejected from the car.

The idea of fabricating a purposeful 'crumple zone' for redirecting the energy and reducing the chances of fracture inside the polymeric microstructure would be of

interest but it is hard to make a designed defect as crumple zone in the periodic or quasiperiodic structured currently fabricated by interference lithography and phase mask lithography. By using two-photon lithography or a second exposure through a mask a designed defect in the structure could be introduced.

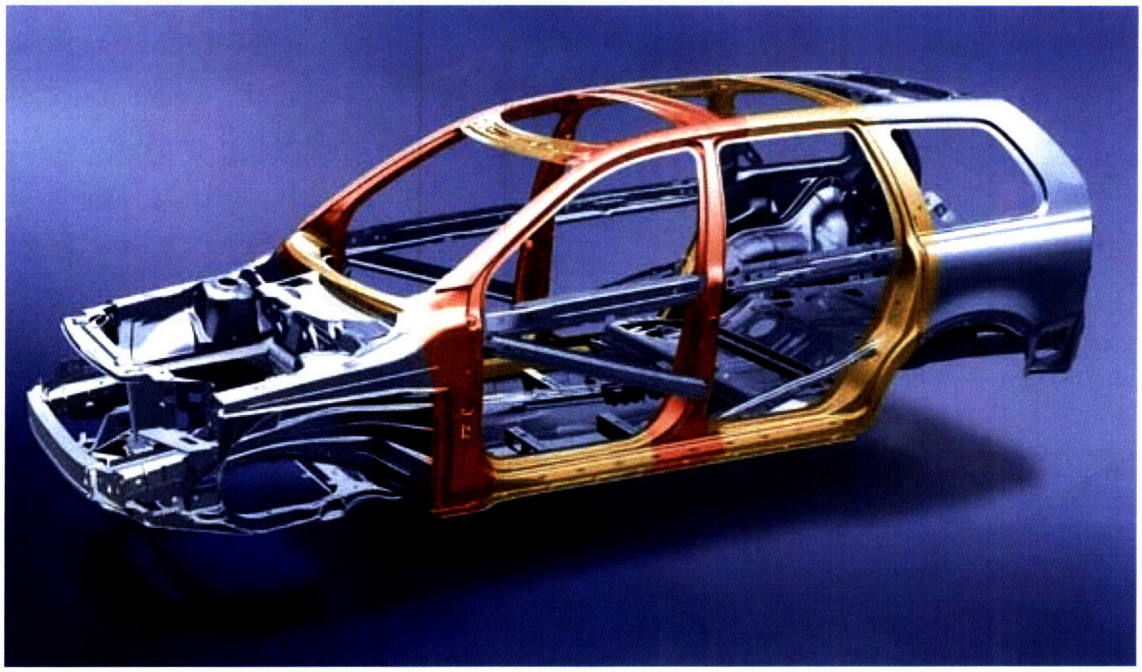

Figure 2-6. The frame of the automobile: the parts (red and yellow) for maintaining and protecting inner space are designed to be stiff and hard, and the other parts (grey, the crumple zones) for absorbing the impact energy are designed to be heavily deformed in appropriate ways.[12]

2.2 Fabrication of Microstructures via Interference Lithography

Interference lithography (IL) is one of the least expensive and the least complicated methods to create 1D, 2D and 3D periodic[13-15] or quasi-periodic[16-19]patterns. The interference of two or three beams of coherent light makes 1D periodic gratings and 2D patterns, respectively. The interference of four or more beams allows fabrication

of 3D periodic structures. The spatial variation of the intensity that determines a periodic structure is given by Eq. (2-1)[20, 21],

$$I(r) = \vec{E}^2 = \vec{E} \cdot \vec{E}^* = \sum_{l=1}^{n} \sum_{m=1}^{n} \varepsilon_l \cdot \varepsilon_m^* \exp[i\{(k_l - k_m) \cdot r + (\phi_l - \phi_m)\}] \propto \sum_{l=1}^{n} \sum_{m=1}^{n} a_{lm} \exp[iG_{lm} \cdot r] \quad (2\text{-}1)$$

where ε_i is the amplitude and polarization of the ith beam, k_i is the wave vector, r is the position vector, a_{lm} is the Fourier coefficient and G_{lm} is the Fourier expansion vector for a periodic structure in reciprocal space. Equation (2-1) demonstrates the similarity between the intensity equation of interference lithography and the Fourier series expansion of a periodic structure. The difference between the wave vectors (k_l-k_m) of the interfering beams determines the translational periodicity of the resultant structure in real space, while the polarizations (ε_i) determine the motif placed within the unit cell. The difference in phases ($\phi_l - \phi_m$) shifts the origin of the structure, which can be ignored for a periodic structure. The combination of the motif and the translational periodicity determine the set of symmetries and the space group of the structure. For four non-coplanar interfering beams, the magnitude (ε_i) of the relative phase amplitudes fix the position of the origin.[21] The experimental set-up in Figure 2-7 shows where the beam goes through beam splitters, wave plates and mirrors to a sample stage for fabricating 3D periodic structures as employed in this thesis.

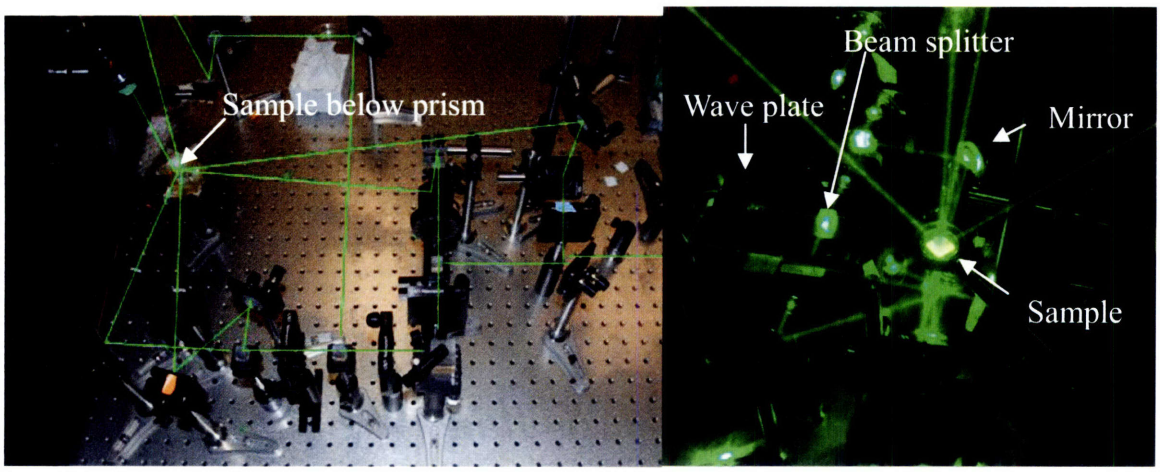

Figure 2-7. (a) Experimental set-up for 3D P structure showing optical components and schematic beam paths for interference lithography. (b) Beam set-up for 3D structure showing beam paths passing through optical components and sample stage.

The well known structure factor, $F_{(h,k,l)}$, of crystallography[20] is,

$$F_{(h,k,l)} = \sum_j f_j \sum_n \exp(2\pi i(hx_n + ky_n + lz_n)), \tag{2-2}$$

where f_j is a factor corresponding to the strength of scattering of the *j*th type of atom and (x_n, y_n, z_n) is the *n*th equivalent position of the *j*th type of atom in the unit cell.[20] In order to correlate the beam parameters and the symmetry elements in the resultant structures, the level set technique[20, 21] is used. Level set surfaces are defined by the functions of the form $F:\mathbf{R}^3 \rightarrow \mathbf{R}$ of points $\{x, y, z\} \in \mathbf{R}^3$, $F(x, y, z)= t$, where t is a constant. To find suitable candidate functions, which are invariant under the space group symmetry operations, the level set equation can be utilized and it is compared with the intensity equation. The level set equation technique uses the structure factor to generate the functions that possess the requisite symmetries and the structure factor describes the amplitudes and phases of the 3D diffraction pattern that are due to the

scattering of incident radiation off of planes (*hkl*) of atoms in the crystalline structure.[20] From Eq. (2-1) and Eq. (2-2), we can calculate out the necessary wave vectors (k_i), amplitudes of the electric field (ε_i), polarizations and the phases of the four or more beams required to create 3D periodic various structures with desired symmetries.[20]

The interference of multiple laser beams was used in the 1990's to theoretically produce both periodic and quasiperiodic optical lattices[22, 23] and became popular in the context of photonic band gap materials after Campbell et al.[24] succeeded in 2000 to fabricate high-quality bicontinuous 3D photonic crystals (PCs) via four-beam IL. The work of Campbell et al. drew a lot of interest and brought attention on IL for fabrication of 3D structures. Subsequently, Yang et al.[25] demonstrated a modified SU8 platform with a base as a contrast enhancer for IL with visible wavelengths. The SU8 based chemically amplified acid catalyzed photoresist system is illustrated in Figure 2-8.

The epoxy-based negative photoresist from the Novolak-resin family is shown in Figure 2-8(c). SU8 is typically used for the fabrication of complex microelectromechanical structures (MEMS) due to its mechanical durability, thermal stability, and dielectric properties combined with easy processability.[26-28] SU8 is easily solution-spun to form a uniform glassy and transparent film on various substrates. The eight epoxy-cycle structure (Fig. 2-8(c)) allows fast thermal and light-initiated

crosslinking resulting in a rigid network polymer with excellent chemical stability. One of the mechanisms of crosslinking is "chemically amplified" cationic polymerization (because a single acid molecule typically induces multiple cleavage reactions in which cleavage reaction is catalytic with respect to acid) with *photosensitizer* (Fig. 2-8(a)) which is active for a certain incident photon wavelength and amplifies the photons activated, and *photoacid generator* (Fig 2-8(b)).[25]

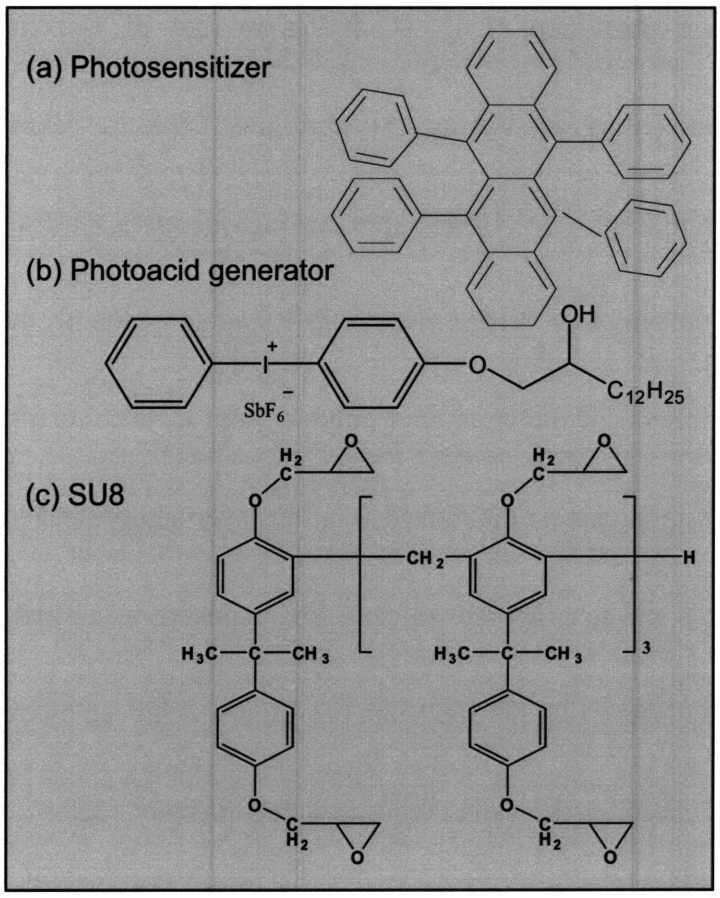

Figure 2-8. Molecular structures of (a) Photosensitizer (rubrene), active for incident wavelengths of 300nm-550nm and amplifying activated photons, (b) Photoacid generator (OPPI), generating acids and catalytically deprotecting epoxy groups on the photoresist in the light exposed regions and (c) Photoresist, SU8 prepolymer, the main platform for structures.[25]

In the case of 355nm and 363.8 nm incident wavelength, a commercially available SU8 solution from Microchem (Newton, MA) was used. For a wavelength of 532 nm, SU8 from Shell Chemicals (Houston, TX) was mixed in cyclopentanone with rubrene as a sensitizer from Sigma Aldrich (St. Louis, MO), and phenyl – p – octyloxy phenyliodonium hexafluoroantimonate (OPPI) as a photoacid generator from Spectra Group Ltd (Millbury, OH).

The basic procedure of IL is similar to that of conventional photomask lithography: spin-coating, pre-baking, exposure, post-exposure baking, developing and drying as shown in Figure 2-9. Before spin-coating, the glass substrate was coated with a thin (700~1000 nm) SU8 buffer layer which was subsequently hard-crosslinked to provide firm adhesion of the structured polymer film to the substrate. Then, the SU8 solution is again spun-cast on the thin SU8 buffer layer and pre-baked at 65℃ for 1min and at 95℃ for 1 min to evaporate solvent. The exposure was conducted using 355 or 532 nm Nd:YAG laser and a flat-top beam profile was achieved by expanding the beam and selectively choosing the central flat constant intensity region of the beam. After exposure, the film was heated to 65 ℃ for several minutes (depending on the structures) for post-exposure bake and then developed with propylene glycol monomethyl ether acetate (PGMEA) for 1 minute at room temperature and rinsed with isopropanol. To

avoid collapse of the 3D microstructure, supercritical CO_2 drying is applied after developing the uncured region to yield the final 3D porous microframe structure over areas as large as 5 mm in diameter.

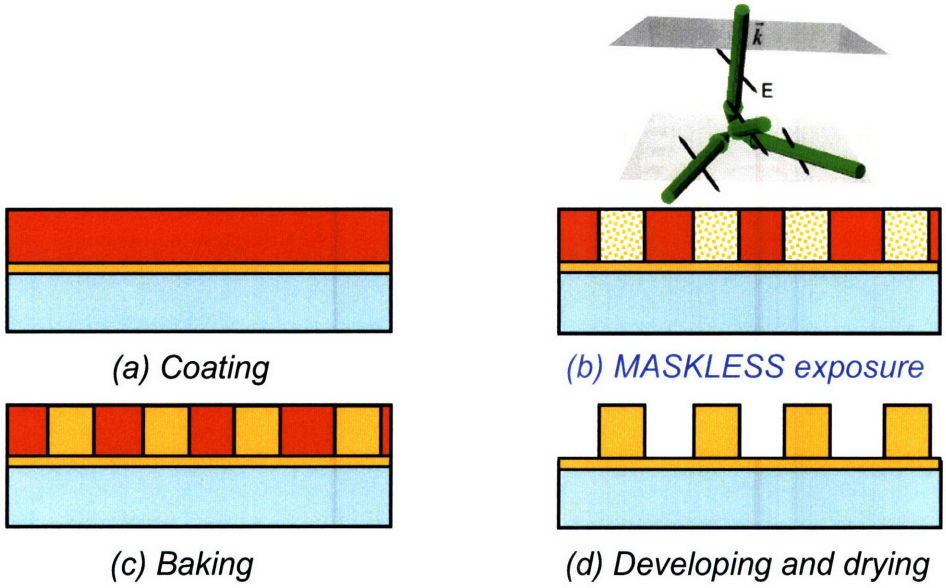

Figure 2-9. The procedure of IL: (a) Thin film cast by spin-coating (blue: glass substrate, orange: SU8 monomer layer, yellow: SU8 thin buffer layer) (b) Maskless exposure using multiple interfering beams: here shows four-beam interference with green laser beams. (black arrows: polarization) (c) Post-exposure baking to promote cationic polymerization of crosslinked network, (d) Developing and drying (supercritical CO_2 drying in some cases). After the procedure, hardbaking is done for certain investigations.

Using IL, we have been able to make different structures in 2D and 3D and some examples are shown in Figure 2-10.[29-31] These fabricated structures are promising for photonic crystals (PCs) and some of them resemble biological microlens arrays.[29]

The three-term diamond-like structure was fabricated by the four-beam interference (Fig 2-10(a) and (b)). As the inset shows in Figure 2-10(a), a prism is utilized for eliminating

refraction of the incident beams to the sample surface. We will further characterize fabricated 3-$R\bar{3}m$ structure morphologically and mechanically in chapter 4. Another 3D periodic structure, P structure, was created by also using the prism and six-beam interference in Figure 2-10(c). Some hexagonal air cylinder arrays in SU8 resemble the biomimetic microlens in brittle stars.

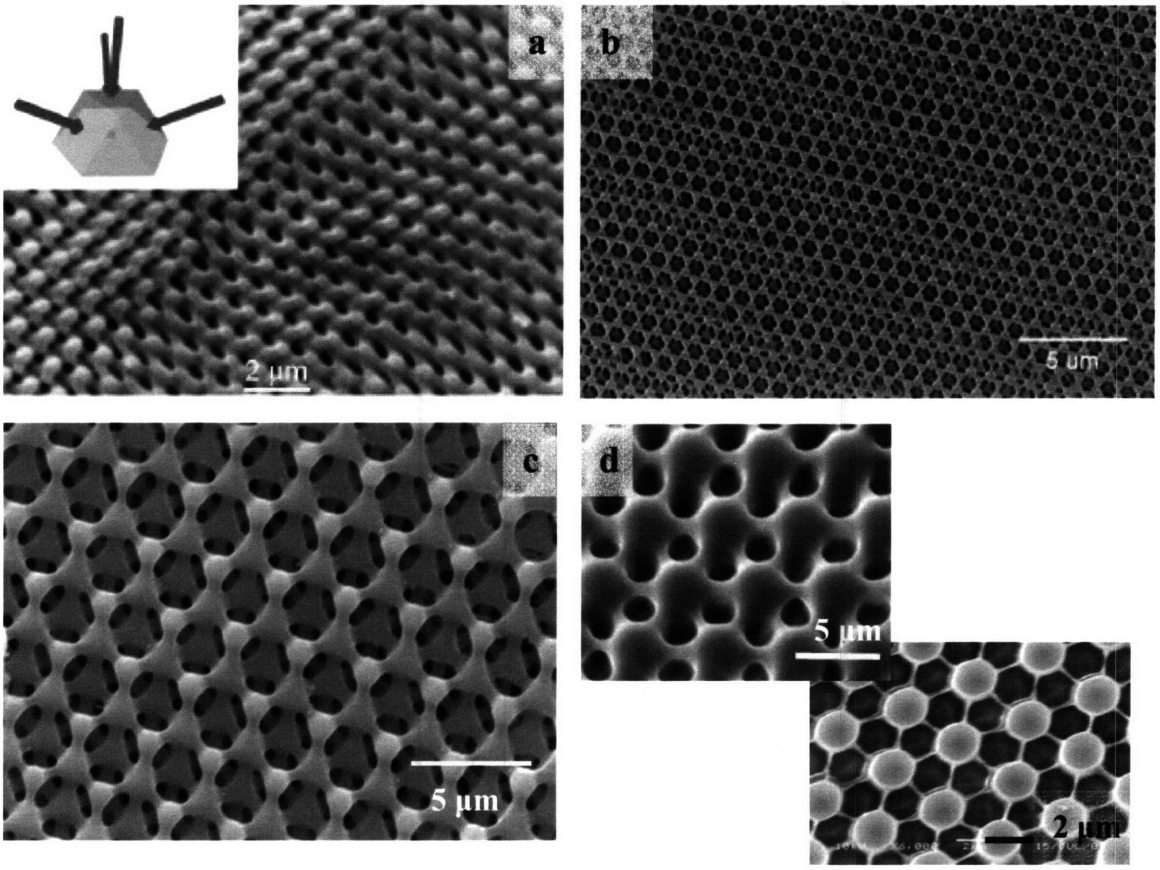

Figure 2-10. A few SU8 microstructures fabricated at MIT via IL. (a) The three-term level set diamond-like structure, 3-$R\bar{3}m$ [30] made by the exposure of the four beam interference pattern in SU8. View: off the threefold axis. Refraction of the incident beams is compensated for by using the index-matched prism configuration shown in the inset; (b) The same 3-$R\bar{3}m$ structure from plan view (see details in chapter 4[29]); (c) P structure from the view of [111] axis and (d) 2D periodic biomimetic microlens arrays with hexagonal air cylinders.[31]

2.3 Fabrication of Microstructures via Phase Mask Lithography

Phase mask lithography (PML) is another method to fabricate 3D crystalline[32] and quasicrystalline (QC) structures.[33] While PML offers less control over the final 3D structure than is possible via direct writing techniques[34, 35], or via multiple-beam IL[19], it has significant practical advantages. Perhaps the most significant one is related to a high throughput and much larger sample sizes, with ~2 cm^2 reported[33] (but full wafer size being practically achievable without an increase in sample preparation time), compared to previously reported 0.1-1 mm^2 size 3D photonic crystals made by multibeam IL[19, 34]. PML also offers flexibility for selecting the symmetry of the final 3D structure, by selecting appropriate 2D phase masks. Furthermore, the feature size of the resulting 3D structures can be adjusted from the sub-micron to a few microns length scale by choosing the wavelength of the laser used in the PML step in conjunction with the average primary feature spacing of the 2D phase mask.

A π phase shift makes abrupt changes of electric field in sign, which determines the intensity patterns and the shape of the structure.[36, 37] This phenomenon is the basis for generating contrast with masks that manipulate only the phase of the light.[37] The phase shift $\Delta\phi$ arising from the shape of the phase mask is given by $\Delta\phi = \frac{2\pi}{\lambda}\Delta n \Delta u$, where λ is the wavelength of the incident light, Δu is the difference in height of the

mask structure and Δn is the difference in refractive indices between the mask and surrounding. In the fabrication of 2D QC phase mask in this thesis, λ= 364 nm, Δu= 500 nm, Δn= 0.45 (n_{PDMS}= 1.45) and the resulting phase shift is 1.24π. For details of analytic theory of π shift phase mask, see Appendix 7.2.

Fabrication of 2D QC phase masks and consequently 3D QC microstructures have not been previously demonstrated. In a first step, 2D QC conformable phase masks were fabricated from 2D templates produced via multiple-exposure IL (ME-IL). These masks were then used to create 3D structured QC photoresist (PR) scaffolds by recording in a thick PR the near field intensity pattern produced by a laser beam incident on the phase mask.

In order to fabricate 2D QC phase masks, we used ME-IL where multiple 1D gratings were recorded in a thin PR layer with in-plane substrate rotations between exposures. Gauthier and Ivanov[16] used a similar dual-beam multiple exposure technique to fabricate 2D QC with 8-, 10-, and 12-fold rotational symmetries, and micron-scale features sizes. In our implementation, a highly stable Lloyd's mirror IL setup[38] with a single *325nm* HeCd laser beam was used to fabricate 2D octagonal QC with feature sizes as small as *~100nm* by serial exposures of 1D gratings followed by three successive 45^{o} rotations of the PR-coated wafer. The high sample quality and small

feature size were enabled by the intrinsic stability of the Lloyd's mirror interferometer, and by using a technique that mitigates the issue of reduced contrast associated with increased number of exposures in IL by maximizing the contrast of each individual exposure (>99%).

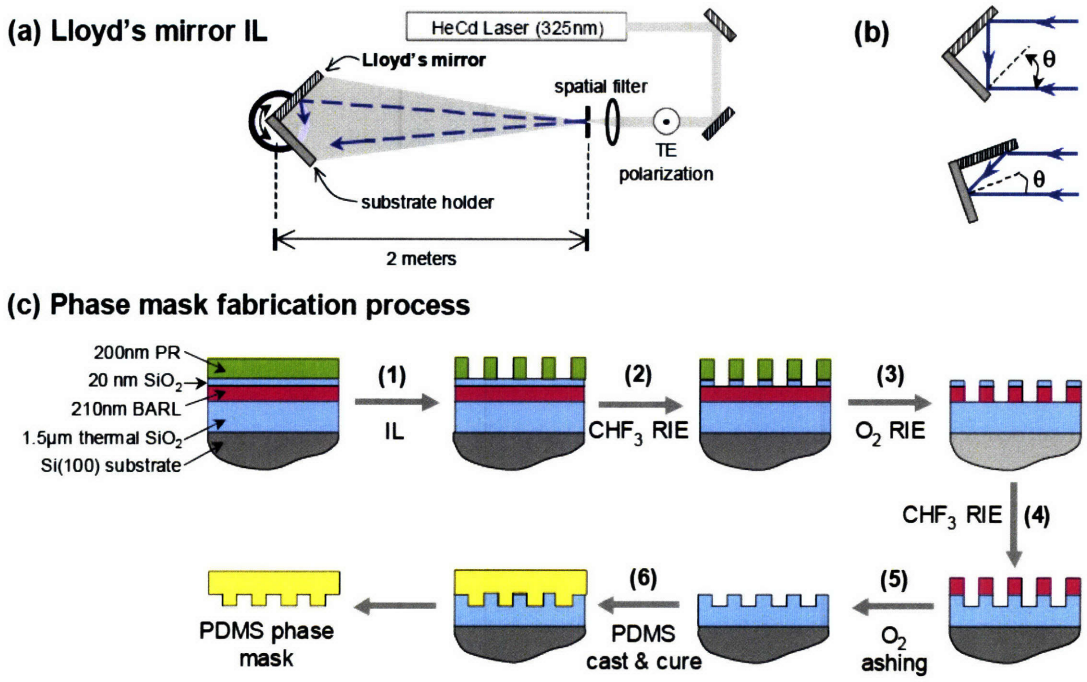

Figure 2-11. (a) Lloyd's mirror interference lithography setup and (b) Controlling the period of the recorded fringes by rotating the sample holder with regard to the incoming beam direction. (c) Fabrication process for 2D QC PDMS phase masks. PR = photoresist, BARL = bottom antireflection layer.[39] These setup and experiments were done in Nano Structure Laboratory of professor H.I. Smith in the Department of Electrical Engineering and Computer Science, MIT.

A diagram of the Lloyd's mirror interferometer used is shown in Figure 2-11(a). The single laser beam of this interferometer is spatially filtered, expanded and projected for a path length of *2m*, and then reaches the sample holder assembly as essentially planar wave fronts due to the large radius of curvature of the actual spherical wave

fronts.[38] The Lloyd's mirror assembly consists of a *10 cm* square optically flat mirror with *λ/4* flatness, arranged perpendicular to the substrate holder so that interference is obtained between the reflected portion of the expanded beam and a portion of the beam that is incident directly on the substrate. Since interference takes place between two parts of the same laser beam, the resulting fringes are virtually immune to any optical path length disturbances away from the sample region. The spatial period of the recorded 1D gratings can be readily varied by rotating the sample holder assembly to change the incidence angle of the incoming laser beam onto the substrate as shown in Figure 2-11(b), with periods greater than 162.5nm being available from our system.[38]

The light intensity distribution recorded in the PR layer after *N=4* equal-dose exposures of TE-polarized beams, with *0°*, *45°*, *90°* and *135°* rotation angles of the recording substrate around the surface normal can be described by:

$$I(x,y) = 2I_0 \sum_{j=1}^{N} \left(1 + \cos\left(2x\, k_{1D} \cos((j-1)\pi/N) + 2y\, k_{1D} \sin((j-1)\pi/N) + \Delta\phi_j\right)\right) \tag{2-3}$$

where I_0 = intensity of the laser beam, $k_{1D} = 2\pi/P_{1D}$, with P_{1D} being the period of the 1D gratings recorded in each exposure, controlled by the angle θ shown in Figure 2-11(b).[33] The $\Delta\phi_j$ terms represent the phase difference between the two interfering beams in each exposure, and are included here for generality. It can be shown that the resulting 2D octagonal quasiperiodic pattern is insensitive to the $\Delta\phi_j$ terms, henceforth

these phase terms will be assumed zero. The predicted 2D octagonal QC structures are obtained by binarizing a section through the *I(x,y)* 3D profile at a particular threshold, which is similar to the binary result of developing the exposed PR layer, and etching into the underlayer. In regions where the exposure dose exceeds a certain threshold, the positive PR becomes soluble, and the remaining PR pattern is then transferred by CHF_3 reactive ion etching (RIE) into the *20nm* SiO_2 interlayer as shown in Figure 2-11(c). The details of processing conditions and concerns in 2D QC patterns and phase masks are further discussed in Ion Bita's Ph.D. thesis.[39]

Having successfully developed a process for making high quality 2D QC templates with desired symmetries, periodicities, fill fractions, and surface relief heights, we next fabricated poly(dimethyl siloxane) (PDMS) phase masks, and used these for producing corresponding 3D QC structures via quasiperiodic phase mask lithography (QCPML). The process we followed is similar to previous reports, which employed phase masks with crystalline symmetries.[40, 41] Making a conformable contact between a mask and a spun-cast PR film in order not to have air gaps, we then shine a laser beam passing though the mask and PR layer. The diffracted beams at the interface interfere with one another and pattern a structure inside the SU8 PR film (Fig. 2-12). After

exposure, the PR film is heated normally at 65°C for 7 minutes, developed in PGMEA for a minute and rinsed with isopropyl alcohol.

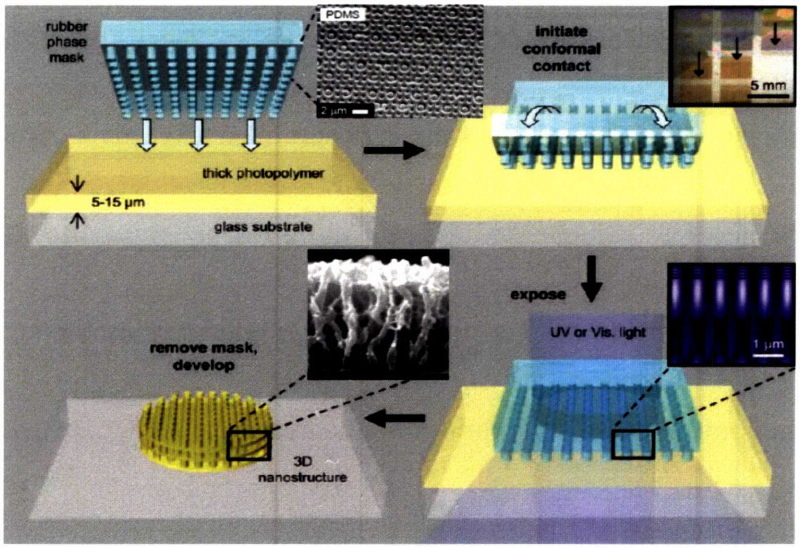

Figure 2-12. Schematic illustration of procedures for using a conformable and elastomeric phase mask to produce 3D quasicrystalline nanostructures: 2D octagonal QC phase mask (SEM) and cross-section SEM of resultant 3D QC nanostructures. Adapted from Jeon et al.[40]

One of the challenges associated with QCPML is related to the higher number of beams in each diffracted order (*N* beams from a 2D QC with *Nmm* point group symmetry, where $N = 8, 10, 12$, etc.), and also to the denser diffraction spectrum of QC compared to crystals.[15] The more beams per diffracted order, the smaller the contrast of the resulting 3D near field intensity pattern, and the smaller the chances of obtaining a self-supported, bicontinuous 3D structure in the recording PR. This is one of the reasons for which we focused on the *8mm* (octagonal) 2D QC symmetry for this study, and not on higher rotational symmetry QC such as *10mm* (decagonal) or *12mm* (dodecagonal).

2.4 Mechanical Characterization by AFM Nanoindentation

Over the last two decades, nanomechanical testing has been increasingly used to measure the local properties of hard thin films because nanomechanical testing achieves controlled measurements of solids with ultra-high resolution[42-48]. Nanoindentation testing is performed with the force normal to the surface on the scale of nanometer resolution employing Atomic Force Microscopes (AFM) (e.g. Digital Instruments Multimode and Dimension 3100) and instrumented nanoindentation (e.g. Hysitron triboindenter). In this dissertation, AFM nanoindentation was conducted on unstructured and 2D structured SU8 polymer films, further discussed in chapter 3.

For the AFM nanoindentation, experimental data are collected in the form of the force-displacement curve (FDC).[47] The FDC is a recording of a cantilever deflection versus a piezo-displacement during the approaching and retracting vertical motion. A typical FDC shown in Figure 2-13 displays several important regions: (a) the probe approaches the surface, (zero cantilever deflection); (b) the probe undergoes "jump-into contact" due to attractive forces between the probe and the surface; (c) the upward deflection of the cantilever in response to the probe interaction with the surface; (d) unloading process; (e) the "jump-off contact" as the tip abruptly moves away from the surface when the cantilever spring force exceeds the adhesion forces; (f) the probe and the surface are separated again (zero cantilever deflection).[47] Segments **abc** describe

the approach part of the cycle and segments **def** describe the retracting part of the cycle. The approach cycle is used to analyze the mechanical properties of the sample. The nanomechanical properties of a surface layer are analyzed within the segment **c** of the approaching cycle of the FDC. The retracting cycle is used for adhesion analysis.

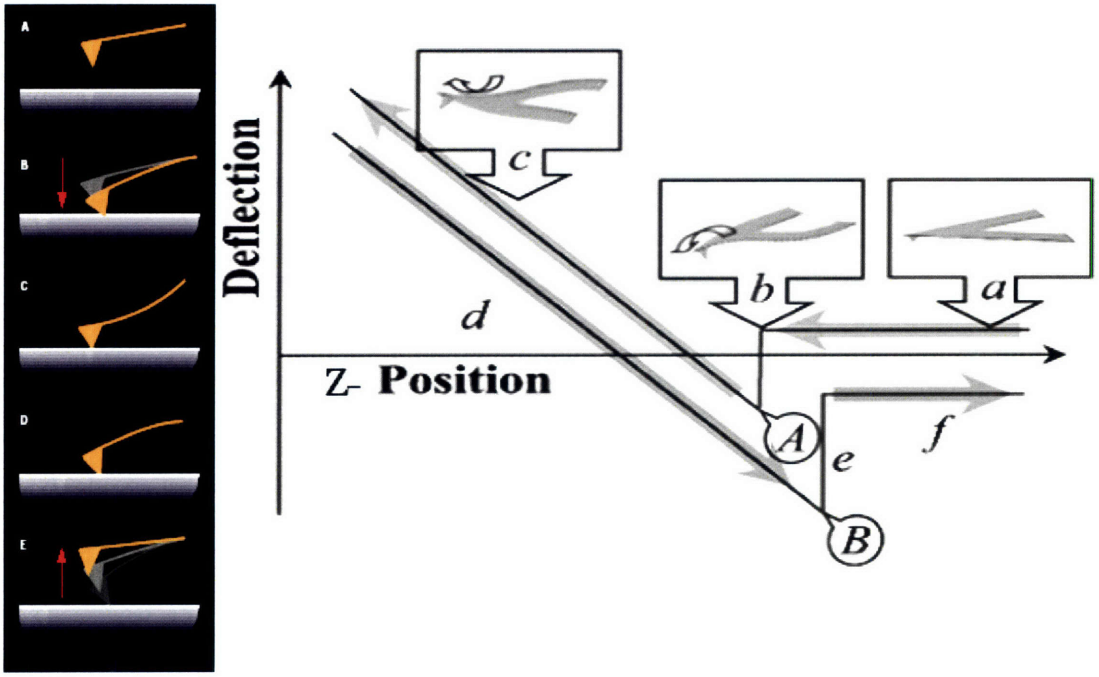

Figure 2-13. Schematic force-distance curve in the approaching-retracting mode with the cantilever shapes: (a) Approach, (b) Jump into contact with jump-in point (A), (c) Load with deflection, (d) Unload and (e) Jump-off contact with pull-off point (B).[47]

There are two basic principles to analyze nanomechanical data in the Scanning Probe Microscopes (SPM) based on *elastic contact*: the Hertzian approximation and Sneddon's equation.[48] For estimating the elastic modulus for small indentation depth, the Hertzian model is applied; for larger indentations, the Sneddon model should be used. In the analytic theories, indentation depth (h) is a function of the applied force

(normal load, P), tip geometry (radius of curvature, *R*), as well as the mechanical and the adhesion properties of the contacting sample and tip.

When a solid sphere with a radius of curvature, R, and the planar surface are in contact under a compressive load, the normal displacements (indentation depth) is related to the pressure, which is the total applied load (P) divided by the area of contact (A). The area of contact is defined as $A = \pi \cdot r^2$, where r is the contact radius in Figure 2-14. Calibrating the radius of curvature of the tip is outlined in Appendix 7.3.

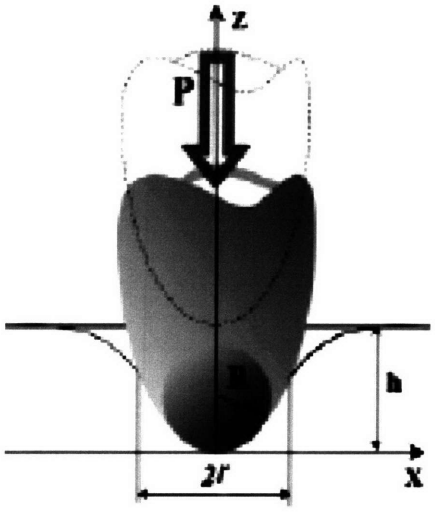

Figure 2-14. The tip-surface interaction with a sphere approximation of the tip end: P = load, R = the radius of curvature, r = the contact radius and h = the penetration depth.[47]

The magnitude of strain, defined by penetration depth/contact radius ($\frac{h}{r}$), is proportional to the compressive pressure divided by the elastic modulus. From the depth-geometry relationship and the strain-pressure relationship, the applied loading

force (P) and the penetration depth (h) can be related via Hertzian approximation is determined[47] as,

$$P = \frac{4}{3} \cdot R^{\frac{1}{2}} \cdot h^{\frac{3}{2}} \cdot E_r, \tag{2-4}$$

$$\frac{1}{E_r} = \frac{1-\nu_i^2}{E_i} + \frac{1-\nu_s^2}{E_s}, \tag{2-5}$$

where E_r is the reduced modulus, which is a summation of the contributions of the indenting tip and the sample, ν_i and ν_s are the Poisson's ratios of the indenting tip and the sample film, and E_i and E_s are the elastic modulus of the indenting tip and the sample, respectively. The Hertzian approximation is valid for elastic, low adhesive and flat surfaces and homogeneous isotropic mechanical properties with a small deformations, when $h < R$, shown in Figure 2-15.

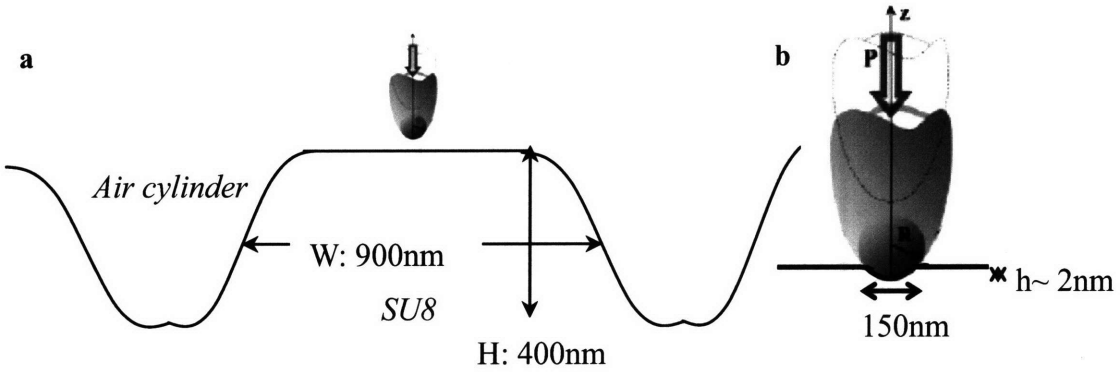

Figure 2-15. (a) Schematic of the geometry of the indenting tip and the sample surface showing the relative size difference (size adapted from conditions in chapter 3) which is valid for Hertzian approximation. The width and height of SU8 region are 900nm and 400nm, respectively. (b) Blow-up image of the tip showing the dimensions of radius of curvature and the indenting depth.

For silicon and silicon nitride probes, because the elastic modulus of the tip is much larger than that of the polymeric sample, we can assume

$$E_s \approx \frac{E_r}{1-\nu_s^2}. \tag{2-6}$$

As a result, the elastic modulus of a polymer sample as a function of indentation depth can be found from the simplified equation:

$$\boxed{E_s = \frac{3}{4} \cdot \frac{1-\nu_s^2}{R^{\frac{1}{2}}} \frac{dP}{d(h^{\frac{3}{2}})}}, \tag{2-7}$$

where the slope of the plot $P \sim h^{3/2}$ is used to calculate E_s.

Sneddon's model can also be applied to describe the tip-plane surface mechanical contact with larger indentation assuming a homogeneous isotropic film.[44] (However, we will not always have the situation of homogeneous isotropic films due to the crosslinked structures and that is interesting to study.) Figure 2-16 shows the load-displacement curve during indentation. From the unloading slope at the maximum load, the sample stiffness is defined as Eq. (2-8),[49]

$$S = \left|\frac{dP}{dh}\right|_{max} = \frac{2\sqrt{A}}{\sqrt{\pi}} E_r. \tag{2-8}$$

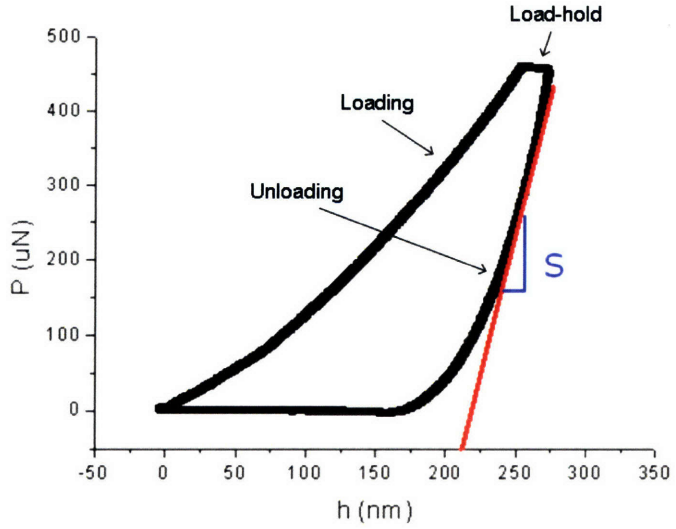

Figure 2-16. A representative experimental load (P)-displacement (h) curve showing stiffness (S) from the slope of the unloading curve at the maximum load.

The contact area of indentation (A) is calculated by the tip area function in terms of the displacement (h) and the geometry of the indenting tip. Figure 2-14 illustrates the cross section image when the indenting tip and the film surface come into contact. By substituting the value of S from the P-h curve and the value of A calculated with h into Eq. (2-8), E_r is calculated. From Eq. (2-6), we can extract E_s since we know all the other material constants.

Klapperich et al.[50, 51] measured E and hardness (H) for various polymers at room temperature, such as poly(methyl methacrylate) (PMMA), polycarbonate (PC) and different kinds of polyethylene (PE) using the static mode of nanoindentation. Recently the dynamic mode of nanoindentation[52-54] considering time-dependent properties has been widely utilized on polymer films. However, the nanoindentaion

still has not been yet applied to explore how local structural differences (crosslink density) of polymer films, as 2D or 3D microframes and trusses, influence local sample modulus. The next chapter of this thesis discusses AFM nanoindentation of 2D hexagonal-arranged air cylinder and polymer film and how the symmetry effect is observed in the force measurements.

Neumann's principle[55] says that the symmetry elements of any physical property of a crystal must exhibit at least the symmetry elements of the point group of the crystal. One axis of 3-fold symmetry in 2D and six axes of 5-fold symmetry in 3D assure an isotropic elastic modulus.[56] We measured the in-plane elastic moduli along all different directions for 2D symmetries of *p6mm* and for 3D octagonal QC symmetry, and validated Neumann's principle in SU8 structured films in chapter 3 and chapter 5.

2.5 Mechanical Characterization by Microtensile Testing

By utilizing a nanoindentation method, the local mechanical properties such as position-dependent elastic moduli within an area of several nm^2 can be investigated. However, indentation does not shed much light on an overall structure effect such as toughness and energy absorption. We need another characterization tool for the structure effect on the large strain mechanical properties of polymer films on the whole.

Due to a several micron thickness with the area of several centimeters and unique geometries of samples, the characterization of thin films poses many unique challenges. A few specific challenges in this arena of nanomechanical testing are an accurate determination of the ratio of stress to strain and the evaluation of viscoelastic and dynamic properties as well as practical issues such as how to grip.[57]

The microtensile tester, NanoUTM from MTS Systems Corporation, (500mN load cell) was utilized for testing thin films of various structures in this thesis in the quasi-static mode. The NanoUTM basically works on the same principle applied for the Instron-type tensile tester with its 10N load cell; each end of the sample is gripped and stretched in tension, the machine measures the load (stress) and the corresponding elongation (strain). The main difference is the sample dimensions; the smallest dimension in the cross section is on the order of micrometer. The typical specimen size for the testing in the thesis is (length, width, thickness) = (5mm, 1mm, 5~7 μm). In case of thin films or fibers, there is no need to make dog-bone shape to test them since the force (load) is very small. Figure 2-17 shows how a fiber sample is mounted for microtensile testing.

One of the representative resulting graphs of a tensile test is shown in Figure 2-18. This particular graph is a characteristic of a brittle polymer; the film does not

exhibit yielding and plastic behavior. The slope near the origin defines the elastic modulus, $d(stress)/d(strain)$ and the area under the curve is toughness, which represents energy absorption during the deformation.

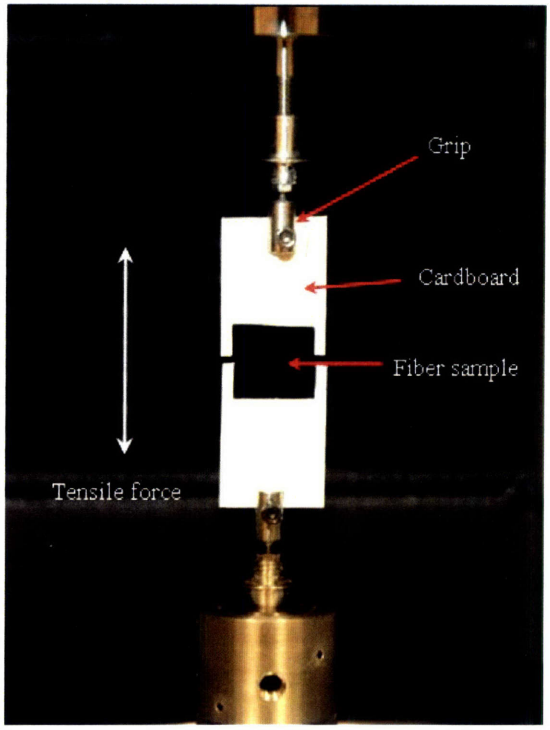

Figure 2-17. A sample mounting (fiber in this case) for uniaxial microtensile testing: the fiber sample is glued on the cardboard which has a rectangular cutout. After gripping both ends, the sides of the cardboard are cut for a tensile measurement of the fiber.

Another type of polymers with extensive plastic behavior is used for calibrating the instrument. A polypropylene (PP) fiber is used as the calibration sample for uniaxial tensile testing in MTS nanoUTM and the resulting stress-strain curve is shown in Figure 2-19. From this stress-strain curve, the elastic modulus is around 1.4 GPa and strain at fracture reaches up to 330%, of which values are similar as known in the Polymer Handbook.[58]

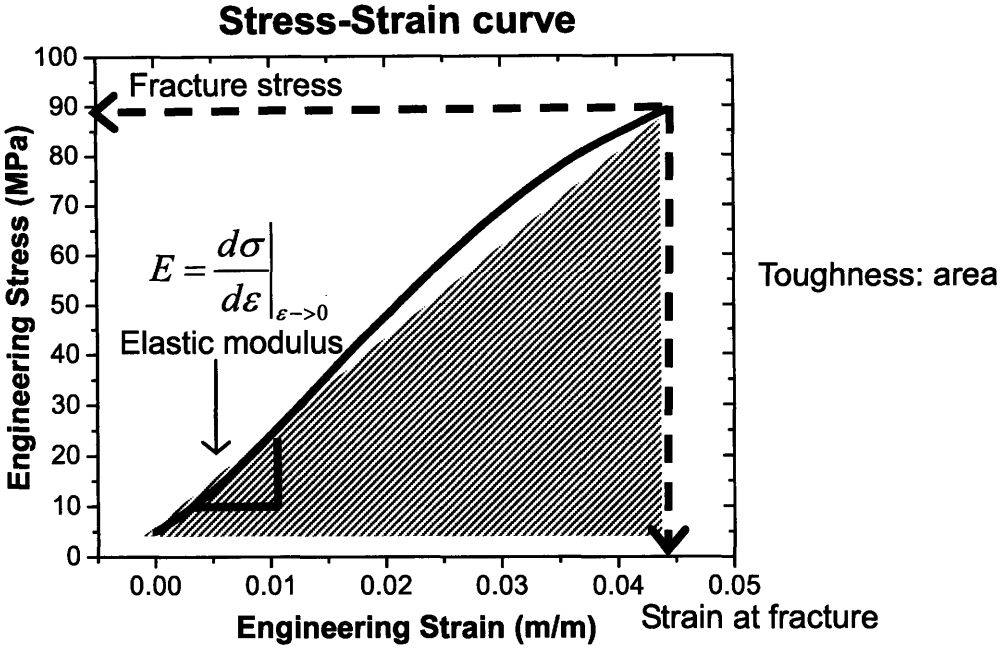

Figure 2-18. A representative stress-strain curve from micro-tensile testing of brittle polymer thin films. Important mechanical parameters are described in the curve.

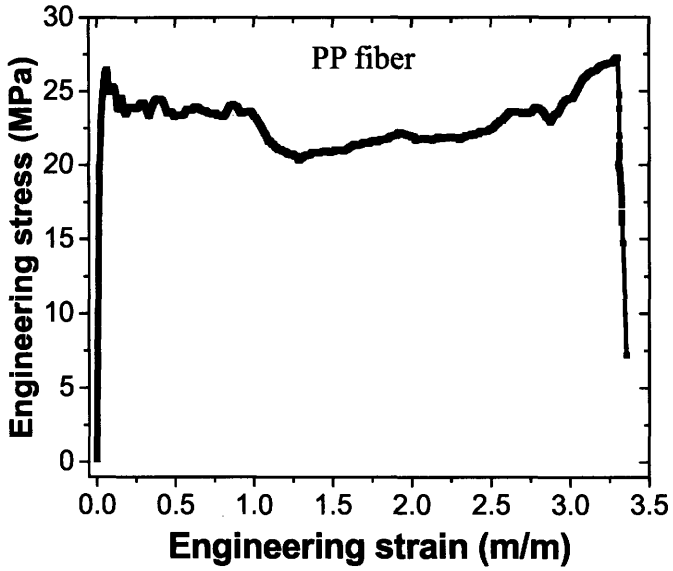

Figure 2-19. A stress-strain curve from the uniaxial tensile testing of polypropylene (PP) fiber, which has a 100 μm diameter and 3 cm gauge length. It exhibits a 1.4 GPa elastic modulus and 330 % strain at fracture with yielding and work hardening. This agrees well with the data in the manual for calibration.

2.6 Mechanical Characterization by Brillouin Light Scattering

Brillouin light scattering (BLS) is ideally suited for investigations of hypersonic crystals (which usually work at frequencies higher than 100 MHz or so) because it allows direct measurement of their complete phonon dispersion relation $\omega = \omega(\vec{k})$. A BLS apparatus has been designed and built by Taras Gorishnyy in our group at MIT.

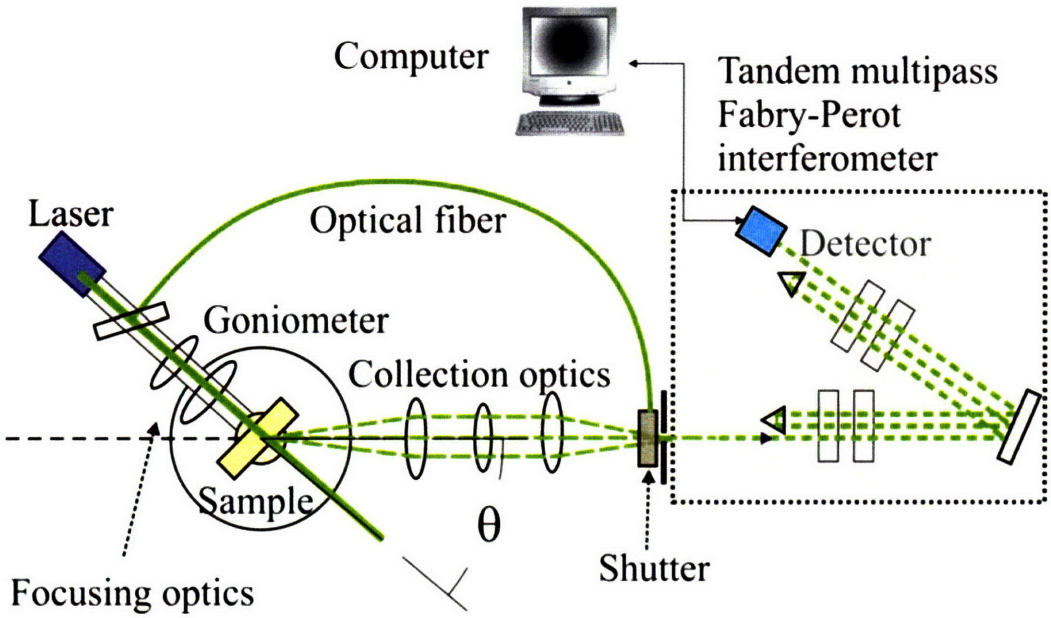

Figure 2-20. Schematic of BLS apparatus: Green lines represent the laser beam path guided by goniometer and optics. Scattering angle of measurements, θ, is variable from nearly 0 to 180 degrees. Courtesy of Taras Gorishnyy (MIT).

A schematic of the BLS apparatus is shown in Figure 2-20. The main components are a light source, focusing and collection optics, mounting mechanics and a tandem Fabry-Perot interferometer used for the spectral analysis of the scattered light. The light source is a continuous wave (cw) green (532 nm) laser mounted on an arm of a goniometer. Usually several hundred mW of cw power is sufficient for most BLS

experiments. More powerful lasers heat samples too much, which may cause material degradation. The laser frequency cannot be chosen arbitrarily; it must match the target operation frequency of the Fabry-Perot interferometer. Another important consideration for the laser selection is its spectral width. Since in Brillouin spectroscopy very small shifts in the light frequency (on the order of several GHz) are measured, it is critical to use lasers with very narrow spectral lines (preferably with full-width-half-maximum (FWHM) <10 MHz).

We use an angle-resolved Brillouin setup with a sample mounted in the center of the goniometer. In this setup measurements at any scattering angle from nearly 0 to 180 degrees are possible both in transmission and reflection, see Figure 2-21. As a result, a wide range of phonon wave vectors (roughly 1 – 35 μm^{-1}) can be accessed. The sample holder uses a separate rotation stage to adjust the orientation of the sample in a plane is normal to the scattering plane. For single crystalline samples this adjustment allows measurement of the phonon dispersion along any desired direction in the Brillouin zone. Finally, most experiments described in this thesis are done in transmission geometry, where the angle ϕ between the incident light and the normal to the sample surface is equal to the half of the scattering angle θ, see Figure 2-21. The unique experimental advantage of this geometry is that the phonon wave vector does not depend on the

refractive index of the sample due to mutual cancellation of the refraction effects at the front and back faces of the sample. It can be shown that the phonon wave vector in this case is given by a simple formula

$$k = \frac{4\pi}{\lambda_0} \sin\left(\frac{\theta}{2}\right), \tag{2-9}$$

where $\theta = 2\phi$ is the scattering angle and λ_0 is the wavelength of light in air.

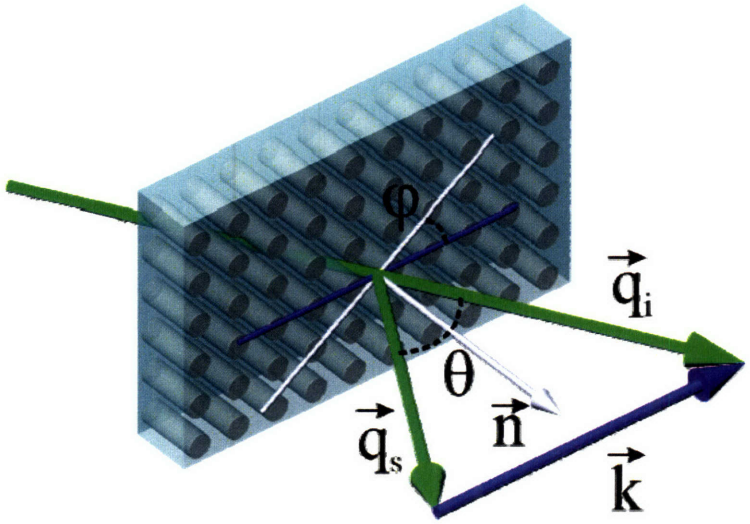

Figure 2-21. Symmetric scattering geometry in transmission BLS experiments. The angle between the incident light and the normal to the sample plane is equal to the angle between the scattered light and the normal to sample plane. In this geometry the phonon wave vector does not depend on the refractive index of the sample.

From BLS spectroscopy, we measure the wave vectors at different angles of the structured films we fabricate and obtain the sound velocity along the different directions inside the structure. Due to the relationship between the longitudinal speed of sound and the bulk modulus, $c = \sqrt{\frac{K}{\rho}}$, we can analyze the mechanical properties of various structures: c is the speed of sound, K is bulk modulus and ρ is density of the

structure. Bulk modulus is related to Young's modulus, which represents the elastic properties, so we can extract out the elastic modulus from BLS measurements, if we know Poisson's ratio of the structured polymer: $K = \frac{E}{3 \cdot (1 - 2\nu)}$.

2.7 References

1. Evans, A. G., "Lightweight materials and structures". *MRS Bull.* **26**, 790-797 (2001).
2. Deshpande, V. S., Ashby, M. F. and Fleck, N. A., "Foam topology bending versus stretching dominated architectures". *Acta Mater.* **49**, 1035-1040 (2001).
3. Smith, J., Hodgins, J., Oppenheim, I. and Witkin, A., "Creating Models of Truss Structures with Optimization". *ACM Trans. Graph.* **21**, 295-301 (2002).
4. Ashby, M. F., "The properties of foams and lattices". *Philos. Trans. R. Soc. A-Math. Phys. Eng. Sci.* **364**, 15-30 (2006).
5. Deshpande, V. S., Fleck, N. A. and Ashby, M. F., "Effective properties of the octet-truss lattice material". *J. Mech. Phys. Solids* **49**, 1747-1769 (2001).
6. Ashby, M. F., *Cellular Ceramics* (eds. Scheffler, M. andColombo, I. P.) (Wiley-VCH, 2005).
7. Gibson, L. J. and Ashby, M. F., *Cellular Solids: Structure and Properties* (Cambridge University Press, Cambridge, 1997).
8. Evans, A. G., Hutchinson, J. W., Fleck, N. A., Ashby, M. F. and Wadley, H. N. G., "The topological design of multifunctional cellular metals". *Prog. Mater. Sci.* **46**, 309-327 (2001).
9. Sypeck, D. J. and Wadley, H. N. G., "Multifunctional microtruss laminates: Textile synthesis and properties". *J. Mater. Res.* **16**, 890-897 (2001).
10. Sypeck, D. J. and Wadley, H. N. G., "Cellular metal truss core sandwich structures". *Adv. Eng. Mater.* **4**, 759-764 (2002).
11. Wallach, J. C. and Gibson, L. J., "Mechanical behavior of a three-dimensional truss material". *Int. J. Solids Struct.* **38**, 7181-7196 (2001).
12. Erickson, C., Crumple Zones in Automobiles, http://members.aol.com/cErick5563/physics/crumple.html (2005).
13. Berger, V., GauthierLafaye, O. and Costard, E., "Photonic band gaps and holography". *J. Appl. Phys.* **82**, 60-64 (1997).

14. Joannopoulos, J. D., Villeneuve, P. R. and Fan, S. H., "Photonic crystals: Putting a new twist on light". *Nature* **386**, 143-149 (1997).
15. Yablonovitch, E., "Inhibited Spontaneous Emission in Solid-State Physics and Electronics". *Phys. Rev. Lett.* **58**, 2059-2062 (1987).
16. Gauthier, R. C. and Ivanov, A., "Production of quasi-crystal template patterns using a dual beam multiple exposure technique". *Opt. Express* **12**, 990-1003 (2004).
17. Notomi, M., Suzuki, H., Tamamura, T. and Edagawa, K., "Lasing action due to the two-dimensional quasiperiodicity of photonic quasicrystals with a Penrose lattice". *Phys. Rev. Lett.* **92** (2004).
18. Wang, X., Ng, C. Y., Tam, W. Y., Chan, C. T. and Sheng, P., "Large-area two-dimensional mesoscale quasi-crystals". *Adv. Mater.* **15**, 1526-+ (2003).
19. Wang, X., Xu, J., Lee, J. C. W., Pang, Y. K., Tam, W. Y., Chan, C. T. and Sheng, P., "Realization of optical periodic quasicrystals using holographic lithography". *Appl. Phys. Lett.* **88**, 051901 (2006).
20. Wohlgemuth, M., Yufa, N., Hoffman, J. and Thomas, L. E., "Triply periodic bicontinuous cubic microdomain morphologies by symmetries". *Macromolecules* **34**, 6083-6089 (2001).
21. Ullal, C. K., Maldovan, M., Wohlgemuth, M. and Thomas, E. L., "Triply periodic bicontinuous structures through interference lithography: a level-set approach". *J. Opt. Soc. Am. A-Opt. Image Sci. Vis.* **20**, 948-954 (2003).
22. Mei, D. B., Cheng, B. Y., Hu, W., Li, Z. L. and Zhan, D. H., "3-Dimensional Ordered Patterns by Light Interference". *Opt. Lett.* **20**, 429-431 (1995).
23. Burns, M. M., Fournier, J. M. and Golovchenko, J. A., "Optical Matter - Crystallization and Binding in Intense Optical-Fields". *Science* **249**, 749-754 (1990).
24. Campbell, M., Sharp, D. N., Harrison, M. T., Denning, R. G. and Turberfield, A. J., "Fabrication of photonic crystals for the visible spectrum by holographic lithography". *Nature* **404**, 53-56 (2000).
25. Yang, S., Megens, M., Aizenberg, J., Wiltzius, P., Chaikin, P. M. and Russel, W. B., "Creating periodic three-dimensional structures by multibeam interference of visible laser". *Chem. Mat.* **14**, 2831-+ (2002).
26. Hong, G., Holmes, A. S. and Heaton, M. E., "SU8 resist plasma etching and its optimisation". *Microsyst. Technol.* **10**, 357-359 (2004).

27. Staedler, T. and Schiffmann, K., "Correlation of nanomechanical and nanotribological behavior of thin DLC coatings on different substrates". *Surf. Sci.* **482**, 1125-1129 (2001).
28. Lee, K. Y., Hu, C. K., Shaw, T. and Kuan, T. S., "Fabrication of microstructures for studies of electromigration in sub-0.25 mu m metal interconnections". *J. Vac. Sci. Technol. B* **13**, 2869-2874 (1995).
29. Jang, J. H., Ullal, C. K., Choi, T. Y., Lemieux, M. C., Tsukruk, V. V. and Thomas, E. L., "3D polymer microframes that exploit length-scale-dependent mechanical behavior". *Adv. Mater.* **18**, 2123-+ (2006).
30. Ullal, C. K., Maldovan, M., Thomas, E. L., Chen, G., Han, Y. J. and Yang, S., "Photonic crystals through holographic lithography: Simple cubic, diamond-like, and gyroid-like structures". *Appl. Phys. Lett.* **84**, 5434-5436 (2004).
31. Yang, S., Chen, G., Megens, M., Ullal, C. K., Han, Y. J., Rapaport, R., Thomas, E. L. and Aizenberg, J., "Functional biomimetic microlens arrays with integrated pores". *Adv. Mater.* **17**, 435-+ (2005).
32. Jeon, S., Menard, E., Park, J. U., Maria, J., Meitl, M., Zaumseil, J. and Rogers, J. A., "Three-dimensional nanofabrication with rubber stamps and conformable photomasks". *Adv. Mater.* **16**, 1369-1373 (2004).
33. Bita, I., Choi, T., Walsh, M. E., Smith, H. I. and Thomas, E. L., "Large Area 3D nanostructures with Octagonal Quaasicrystalline Symmetry via Phase Mask Lithography". *Adv. Mater.* (2007).
34. Ledermann, A., Cademartiri, L., Hermatschweiler, M., Toninelli, C., Ozin, G. A., Wiersma, D. S., Wegener, M. and Von Freymann, G., "Three-dimensional silicon inverse photonic quasicrystals for infrared wavelengths". *Nat. Mater.* **5**, 942-945 (2006).
35. Man, W. N., Megens, M., Steinhardt, P. J. and Chaikin, P. M., "Experimental measurement of the photonic properties of icosahedral quasicrystals". *Nature* **436**, 993-996 (2005).
36. Aizenberg, J., Rogers, J. A., Paul, K. E. and Whitesides, G. M., "Imaging the irradiance distribution in the optical near field". *Appl. Phys. Lett.* **71**, 3773-3775 (1997).
37. Rogers, J. A., Paul, K. E., Jackman, R. J. and Whitesides, G. M., "Generating similar to 90 nanometer features using near-field contact-mode photolithography with an elastomeric phase mask". *J. Vac. Sci. Technol. B* **16**, 59-68 (1998).

38. Walsh, M. E., *On the design of lithographic interferometers and their application.* Ph. D. thesis, Dept. of Electrical Engineering and Computer Science, Massachusetts Institute of Technology, (Cambridge, 2004).

39. Bita, I., *Breaking symmetries in ordered materials : spin polarized light transport in magnetized noncentrosymmetric 1D photonic crystals, and photonic gaps and fabrication of quasiperiodic structured materials from interference lithography.* Ph. D. thesis, Dept. of Materials Science and Engineering., Massachusetts Institute of Technology., (Cambridge, 2006).

40. Jeon, S., Park, J. U., Cirelli, R., Yang, S., Heitzman, C. E., Braun, P. V., Kenis, P. J. A. and Rogers, J. A., "Fabricating complex three-dimensional nanostructures with high-resolution conformable phase masks". *Proc. Natl. Acad. Sci. U. S. A.* **101**, 12428-12433 (2004).

41. Maria, J., Jeon, S. and Rogers, J. A., "Nanopatterning with conformable phase masks". *J. Photochem. Photobiol. A-Chem.* **166**, 149-154 (2004).

42. Pethica, J. B. and Oliver, W. C., "Tip Surface Interactions in STM and AFM". *Phys. Scr.* **T19A**, 61-66 (1987).

43. Doerner, M. F. and Nix, W. D., "Stresses and Deformation Processes in Thin-Films on Substrates". *CRC Critical Reviews in Solid State and Materials Sciences* **14**, 225-268 (1988).

44. Oliver, W. C. and Pharr, G. M., "An Improved Technique for Determining Hardness and Elastic-Modulus Using Load and Displacement Sensing Indentation Experiments". *J. Mater. Res.* **7**, 1564-1583 (1992).

45. Briscoe, B. J., Fiori, L. and Pelillo, E., "Nano-indentation of polymeric surfaces". *J. Phys. D-Appl. Phys.* **31**, 2395-2405 (1998).

46. Oyen, M. L., Cook, R. F., Emerson, J. A. and Moody, N. R., "Indentation responses of time-dependent films on stiff substrates (vol 19, pg 2487, 2004)". *J. Mater. Res.* **19**, 3120-3121 (2004).

47. Shulha, H., Kovalev, A., Myshkin, N. and Tsukruk, V. V., "Some aspects of AFM nanomechanical probing of surface polymer films". *Eur. Polym. J.* **40**, 949-956 (2004).

48. Johnson, K. L., *Contact Mechanics* (Cambridge University Press, New York, 1985).

49. VanLandingham, M. R., Villarrubia, J. S., Guthrie, W. F. and Meyers, G. F., "Nanoindentation of polymers: An overview". *Macromol. Symp.* **167**, 15-43 (2001).

50. Klapperich, C., Komvopoulos, K. and Pruitt, L., "Nanomechanical properties of polymers determined from nanoindentation experiments". *J. Tribol.-Trans. ASME* **123**, 624-631 (2001).
51. Klapperich, C., Pruitt, L. and Komvopoulos, K., "Nanomechanical properties of energetically treated polyethylene surfaces". *J. Mater. Res.* **17**, 423-430 (2002).
52. Asif, S. A. S., Wahl, K. J. and Colton, R. J., "Nanoindentation and contact stiffness measurement using force modulation with a capacitive load-displacement transducer". *Rev. Sci. Instrum.* **70**, 2408-2413 (1999).
53. Du, B. Y., Tsui, O. K. C., Zhang, Q. L. and He, T. B., "Study of elastic modulus and yield strength of polymer thin films using atomic force microscopy". *Langmuir* **17**, 3286-3291 (2001).
54. Ngan, A. H. W. and Tang, B., "Viscoelastic effects during unloading in depth-sensing indentation". *J. Mater. Res.* **17**, 2604-2610 (2002).
55. Nye, J. F., *The physical properties of crystals* (Oxford University Press, Oxford, 1985).
56. Christensen, R. M., "Sufficient Symmetry Conditions for Isotropy of the Elastic-Moduli Tensor". *J. Appl. Mech.-Trans. ASME* **54**, 772-777 (1987).
57. Corporation, M. S., MTS Nano Instruments, Products, Nano UTM, http://www.mtsnano.com/products/utm/ (2007).
58. eFunda, eFunda: Engineering Materials, www.efunda.com/materials (2007).

Chapter 3. Elastic Properties of 2D Hexagonal Structures*

In the previous chapter in section 2.2, we discussed a technique, interference lithography (IL), which allowed us to fabricate various periodic and quasiperiodic structures. In section 2.4, we described AFM nanoindentation as a characterization tool to probe local mechanical properties. In this chapter we present the results of an experimental investigation of the elastic properties of a 2D hexagonal air-cylinder and the corresponding solid polymer film via AFM force measurements. The elastic modulus is found to systematically vary as a function of location in the hexagonal air-cylinder-epoxy film reflecting the local crosslink density of the polymer film.

3.1 Introduction to SU8 properties

To date only a few studies address the mechanical properties of SU8 under microfabrication conditions. Feng and Farris[1] investigated the dependence of the mechanical properties of 130 micron-thick SU8 films at different relatively simple processing conditions such as post-exposure bake (PEB) temperature, time and hardbake (HB) time (Fig. 3-1). The reported elastic moduli range from 0.7 GPa for the as-cast glassy monomer to 2.7 GPa with PEB and HB for a UV-cured material (see

* This chapter is based on a paper published in *Adv. Func. Mater.* **16**, 1324-1330 (2006).

Figure 3-1). Reducing the post-exposure bake time results in decreasing crosslinking density, thus, a lower elastic modulus with an increase in elongation to break.[1, 2] The glass transition temperature of SU8 is 55°C in the uncured state and increases to 230°C for fully cured material with a linear relationship found between glass transition temperature and crosslinking density and the degree of conversion of the epoxy groups reaching 90% for e-beam curing.[1, 3]

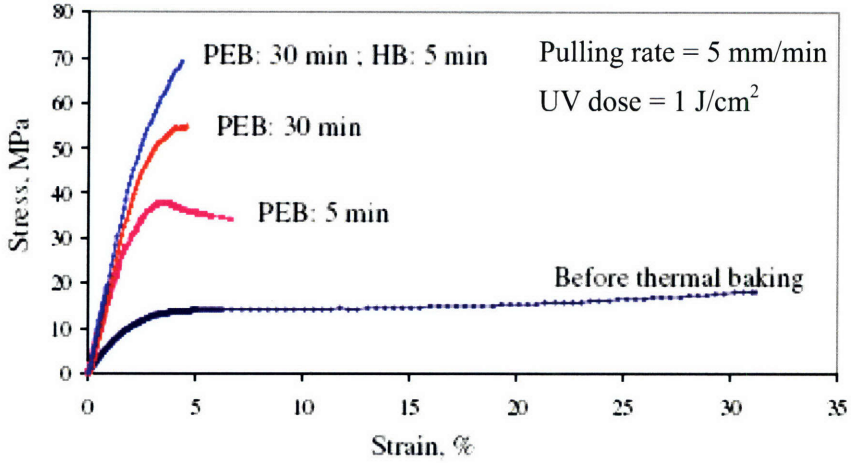

Figure 3-1. Stress-strain curves for SU8 film at different stages of processing.[1] The free standing samples peeled off from the substrate were tested under a tensile force. Without the post-exposure bake, SU8 glassy monomer film exhibits a fairly large strain at fracture (~30%). With post-exposure bake and hardbake, the film becomes stiffer and more brittle.

The recent application of advanced optical microfabrication methods such as holographic interference lithography (IL) for creating complex 2D and 3D microstructures poses the question of the actual distribution of crosslink density and, thus, the corresponding spatial distribution of mechanical and thermal properties within these structures.[4, 5] In accordance with usual consideration of MEMS structures,

current approaches simply treat these complex porous microstructures as a two-phase (polymer-air) composite with properties of the epoxy material assumed identical to that of the corresponding bulk state.

In order to investigate the actual material properties of the complex photopatterned materials fabricated by IL, we focus on the elucidation of the spatial distribution of elastic and plastic properties of a relatively simple 2D microstructure. Using atomic force microscopy (AFM), we conduct high-resolution nanomechanical studies of the thin SU8 film having a hexagonal pattern of cylindrical air holes fabricated via three-beam laser IL. A spatial distribution of the local elastic modulus, which can be directly related to the symmetry of light intensity distribution within the original interference pattern in the photoresist, is found with higher elastic modulus observed for the node regions in accordance with the highest light intensity locations (see Fig. 3-2, detailed measurements are in section 3.3.2).

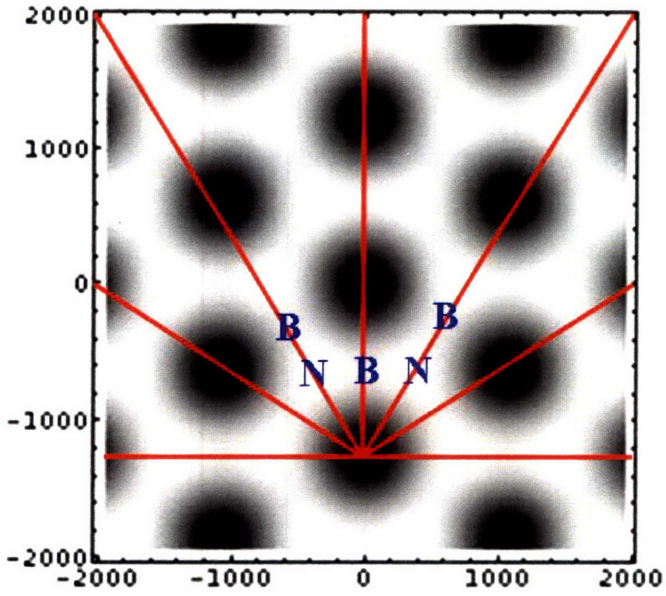

Figure 3-2. 2D light intensity distribution for three-beam interference used for the fabrication of the patterned specimen along with primary lattice vectors for corresponding 2D lattice; **N** stands for the regions of nodes having highest intensity and **B** stands for the regions of beams having slightly lower intensity than nodes (see Figure 3-5).

Theoretically the difference in the light intensity between nodes (N) and beams (B) is small as shown the brightness difference in Figure 3-2 and Figure 3-5 (c) and (d), so that the expected corresponding difference in the elastic modulus should not be very big. Moreover, since we test the samples at $T_{testing} < T_g$ (the testing temperature is room temperature and the glass transition temperature of the crosslinked SU8 is around 100 °C from a differential scanning calorimetry (DSC) experiment), differences in crosslink density will not be as easily detected as for $T_{testing} > T_g$.[6]

3.2 AFM Nanoindentation of Uncured and Cured SU8 films

Uncured and cured uniform 5 μm-thick SU8 films on glass substrates were first tested by AFM nanoindentation for comparative purposes. Uncured film was prepared with spin-coating of the SU8-cyclopentanone solution on a glass substrate and followed by pre-baking at 65°C for 1 minute and 95 °C for 2 minutes for solvent evaporation. For cured film the following procedure was conducted as explained in section 2.2: spin-coating of SU8 solution, pre-baking, exposure with continous-wave (cw) 532 nm Nd:YAG laser with a dose of 3 J/cm^{2,}, post-exposure baking at 65 °C for 5 minutes, developing in propylene glycol monomethyl ether acetate (PGMEA) and drying with nitrogen gas. The films showed a very smooth surface topography with the RMS microroughness of 0.3 nm for uncured films and the 0.9 nm for cured films (measured within 3x3 μm^2 areas) indicating a little surface alteration after the laser beam exposure and curing procedure used in this study (Fig. 3-3(a) and 3-4(a)). No significant wrinkling of the polymer film observed indicates small or uniform shrinkage (~8%) and insignificant residual stresses developing in the bulk crosslinked SU8 material as was reported in previous studies.[7-9]

	Uncured film	Cured film	2D hexagonal film
Prebake	65 °C for 1 min and 95 °C for 2 min	65 °C for 1 min and 95 °C for 2 min	65 °C for 1 min and 95 °C for 2 min
Exposure	None	I_0* = 3 J/ cm^2	I_0* = 5.7 J/cm^2, total intensity of 3 beams. Interference pattern: I_{min} = 1.2 J/cm^2 and I_{max} = 8 J/cm^2
PEB	N/A	65 °C, 5 min	65 °C, 5 min
Develop	N/A	In PGMEA, 1 min	In PGMEA, 2 min

*Exposure with 532nm, uniform intensity cw Nd:YAG laser.

Table 3-1. Processing conditions for uncured, cured uniform film and 2D hexagonally structured SU8 films. Since they have same spin-coating rate, the film thicknesses of three films should be similar with ~ 8% shrinkage of SU8.[8, 9] The exposure energies are calculated with the measured power, exposure time and from the theoretical light intensity distribution.

The surface distribution of the out-of plane elastic modulus data of the uncured SU8 film obtained with static AFM force-volume micromapping with spatial resolution of below 0.2 μm shows a relatively uniform modulus distribution and indentation depth not exceeding 3 nm (Fig. 3-3(b)).[10] The histogram of the surface distribution of the elastic modulus confirms the expected uniform spatial distribution with virtually all

values obtained in the range from 500 to 1500 MPa and the average elastic modulus measured of about 1 GPa (Fig. 3-3(c)). This value is close to that reported for bulk uncured SU8 films (0.7 GPa) from tensile experiments for bulk specimens[1] and confirms virtually identical microscopic elastic response of thin films studied here to macroscopic elasticity of the bulk material.

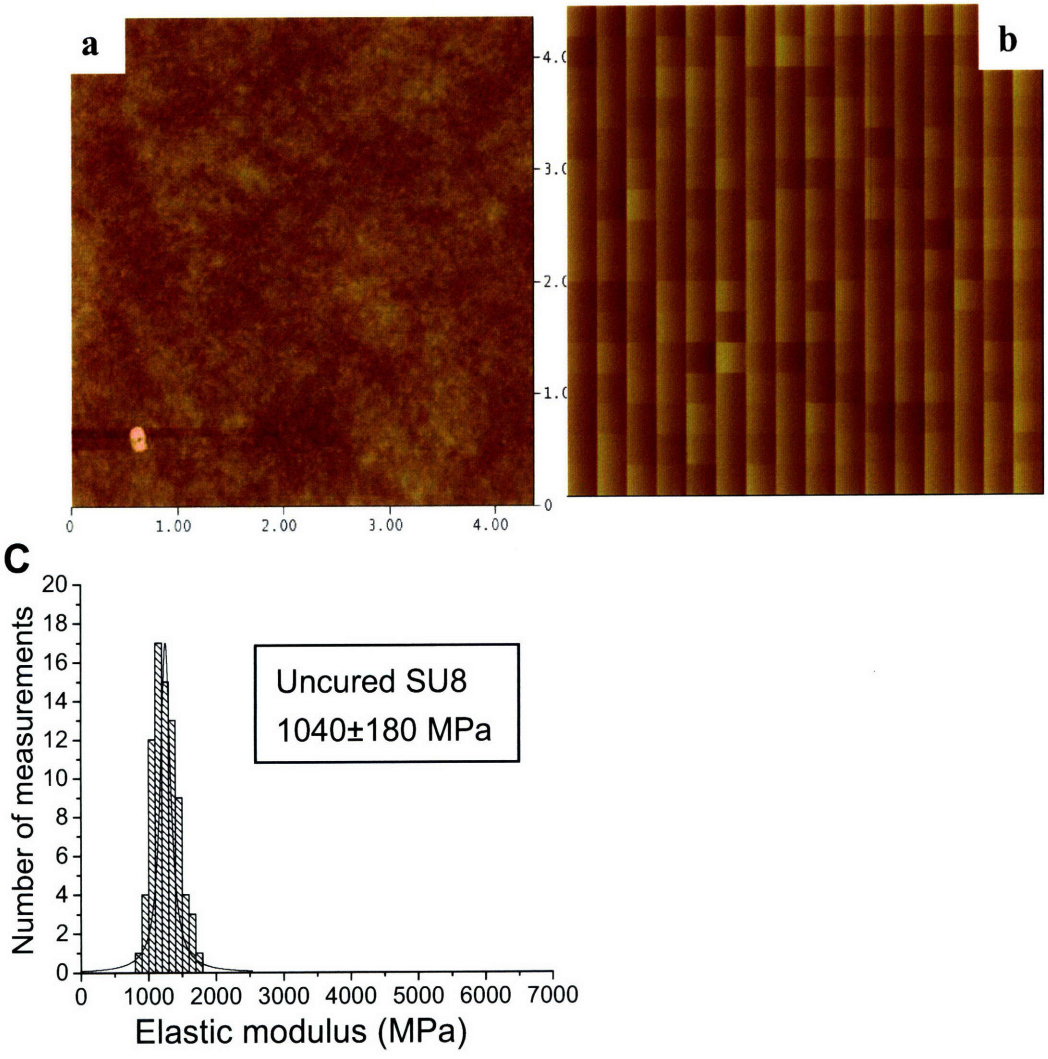

Figure 3-3. AFM data for uncured SU8 film: (a) AFM topography image with 0.3 nm RMS roughness. A white spot in the lower left is a dirt particle. (b) The surface distribution of the elastic modulus from 16x16 force measurements ($3x3\mu m^2$). (c) The histogram of the elastic modulus distribution.

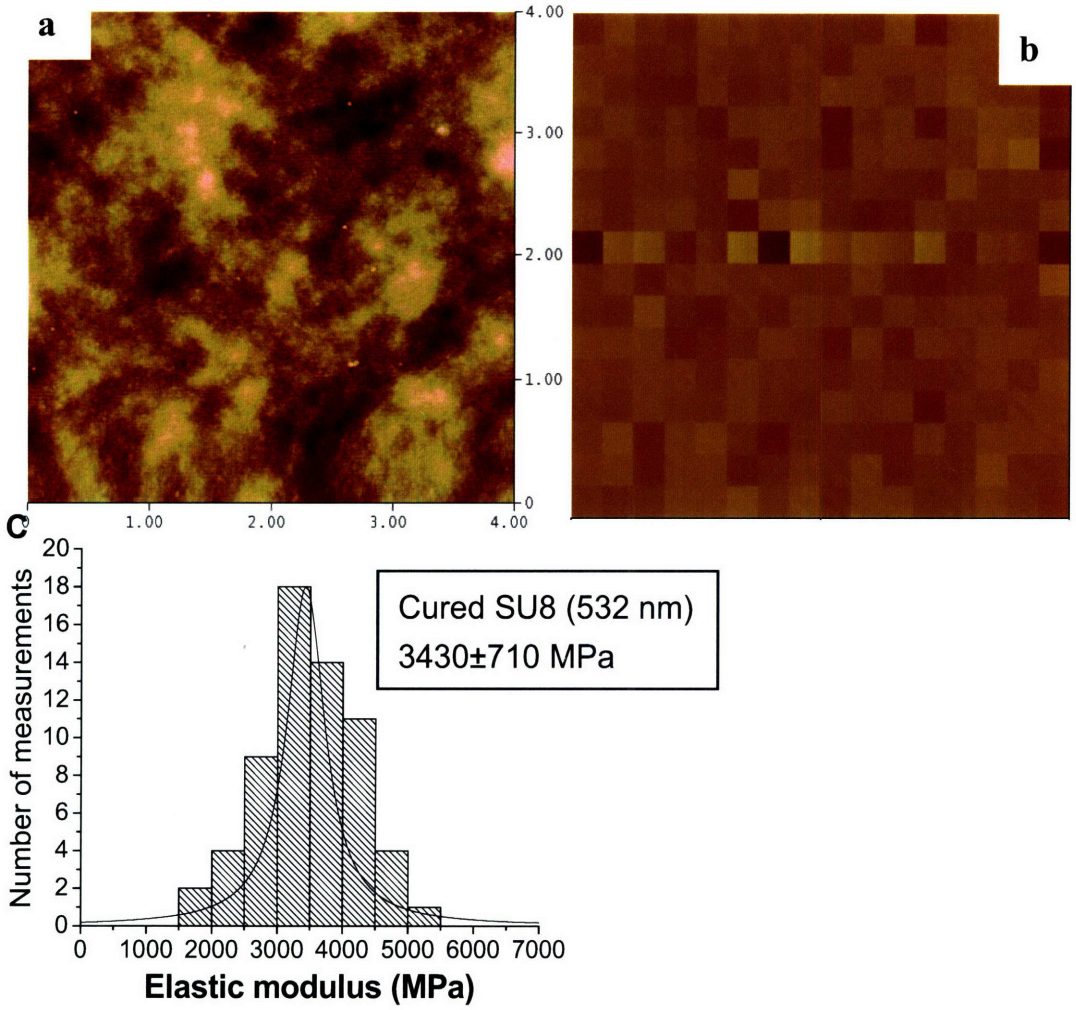

Figure 3-4. AFM data for cured SU8 film: (a) AFM topography image with 0.9nm RMS roughness. (b) The surface distribution of the elastic modulus from 16x16 force measurements (2x2 μm^2). (c) The histogram of the elastic modulus distribution.

The surface distribution of the elastic moduli obtained with spatial resolution (below 0.1 μm) for cured SU8 films was uniform as well (Fig. 3-4(b)). The standard deviation for different surface areas was 20% indicating little spatial and chemical inhomogeneities at a microscale which can be generated by uniform light-initiated crosslinking and chemical developing (Fig. 3-4(c)). The average elastic modulus after curing increased significantly as compared with the uncured film and reached 3-4 GPa

(Fig. 3-4(c)). This value is fairly close to that obtained from macroscopic tensile experiments (~4 GPa) for the bulk SU8 material.[1, 11, 12]

3.3 AFM Nanoindentation of 2D Hexagonal lattice SU8 film

3.3.1 Fabrication of 2D Hexagonal Lattice via IL

2D patterns were fabricated using three-beam holographic IL that allows generation of periodic structures over large areas with high resolution.[13, 14] The fabrication procedure involved the interference of three equal intensity laser beams and the transfer of the resultant intensity pattern into an SU8 photoresist platform via laser-initiated cationic polymerization as described in section 2.2.[15]

To increase the adhesion between the glass substrate and SU8 layer, a 1 μm thick buffer layer of SU8 was spin-coated (2,000 rpm, 1 min) and pre-baked (5 min at 95 °C). It was then flood-exposed under the UV lamp and hard-baked at 180°C for 10 min. This layer effectively improved adhesion of the patterned SU8 layer to the substrate and prevented delamination during the developing process. Next, the SU8-cyclopentanone solution was spun-coated on top of this existing SU8 film at a spin speed of 1000 rpm. The coated photoresist was then pre-baked at 65°C for 1 min and 95°C for 2 min. The exposure was done using a 532 nm Nd:YAG laser with an input intensity of 5.7 J/cm^2

(I_0) to give the range of an exposure dose of 1.2 ~ 8.0 J/cm^2 over areas with diameter larger than 5 mm. The directions and polarization of the three beams are given by

$$\vec{k}_1 = [0.0164, 0.0073, 0.0073], \quad \vec{E}_1 = [0, -2.45, 2.45],$$

$$\vec{k}_2 = [0.0073, 0.0164, 0.0073], \quad \vec{E}_2 = [0, -2.45, 2.45],$$

$$\vec{k}_3 = [0.0073, 0.0073, 0.0164], \quad \vec{E}_3 = [-0.97, -2.97, 1.75],$$

where each beam has same intensity of $I_0/3$ = 1.9 J/cm^2. After baking the 6㎛-thick film at 65 ℃ for 5 min, the resultant cationic photopolymerization only takes place in regions that were exposed to high intensities of light. The uncured regions were developed away in PGMEA and the film was finally rinsed with isopropyl alcohol to yield the 2D porous photopatterned structure.

3.3.2 AFM Nanoindentation Measurements

The interference pattern was designed to create a 2D lattice with hexagonal symmetry and pre-defined spacing (1.22 μm) and porosity level (40%). The 2D distribution of light intensity created by three-beam IL is presented in Figure 3-5(a), along with a sketch of a unit cell and primary lattice vectors for the 2D air-cylinder lattice. The brighter spots represent the nodes (**N**) with the highest intensity and the somewhat less intense regions are called beams (**B**) as marked in Figure 3-5(a). The actual surface morphology of the photopatterned film showed a well-ordered, long-

range, 2D lattice with a hexagonal array of air holes closely resembling the theoretical light "template" (black regions in Fig. 3-5(a)) as can be seen in SEM image (Fig. 3-5(b)).

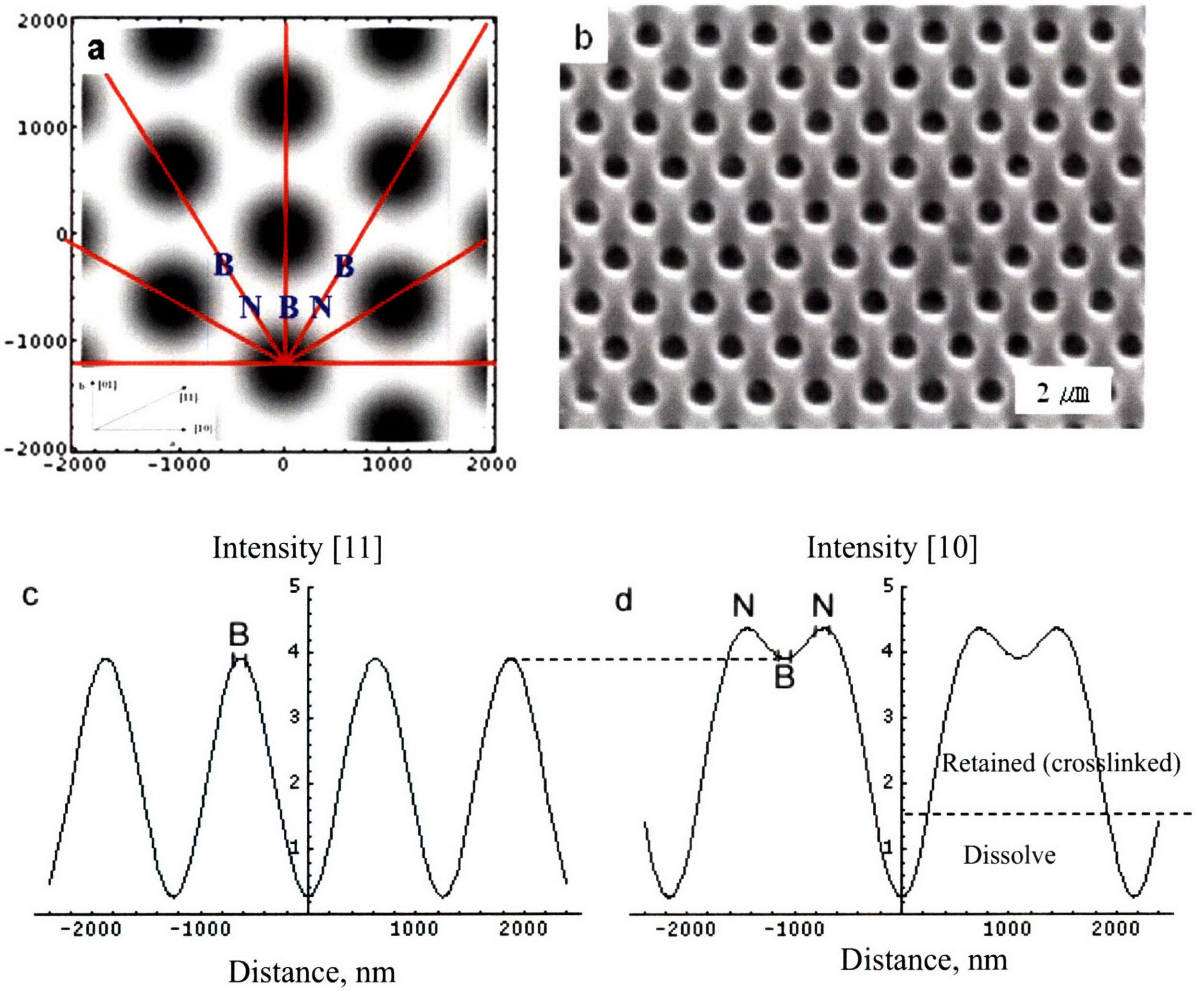

Figure 3-5. (a) 2D light intensity distribution for three-beam IL used for the fabrication of the patterned specimen along with (inset) primary lattice vectors for corresponding 2D lattice; **B** and **N** stand for regions of beams and nodes of lattice. (b) Scanning electron microscopy (SEM) image shows long-range ordered 2D hexagonal lattice; (c) One-dimensional light intensity distribution along the [11] direction (y axis in arbitrary values, DC offset is removed by amine). The intensity of each beam is assumed as 1 ($=I_0/3$ (1.9 J/cm^2)) in the graphs. (d) One-dimensional light intensity distribution along the [10] direction.

The 1D theoretical light distribution across the nodes and beams is shown in Figure 3-5(c) and (d) along the [11] direction and along the [10] direction. The intensity of light distribution along the [11] direction is a simple periodic function but a more complex periodic intensity distribution is observed along the [10] direction with intensity slightly lower for beams (marked B) between two neighboring nodes (marked N) (Fig. 3-5(c), (d)).

The surface morphology of the 2D polymer films with higher resolution was obtained using the tapping mode AFM in Figure 3-6. The AFM images revealed a well-developed topography with an array of round holes penetrating through the polymer film (Fig. 3-6(a)). A porosity level of about 40% and a spacing of 1220 nm were estimated from the cross-section analysis and 2D Fourier transforms of the AFM images, respectively. The polymer surface between the round holes was relatively smooth with the local microroughness not exceeding 1 nm within 500x500 nm^2 surface areas, which satisfies assumptions of Hertzian model for interpreting the mechanical data. The nanomechanical measurements were conducted in the elastic regime with an indentation depth of less than 2 nm allowing full elastic recovery of the tested surface areas after probing (Fig. 3-6(b)). Each pixel in Figure 3-6(b) has 80 nm x 80 nm lateral dimensions and represents the entire surface area for a single force measurement. The estimated

contact area for a single nanoprobe experiment did not exceed 1 nm^2 which is very small so that the distance between two successive indentations (80 nm) precluded interference related to stress generation. Having the Force-Volume scan mode of the

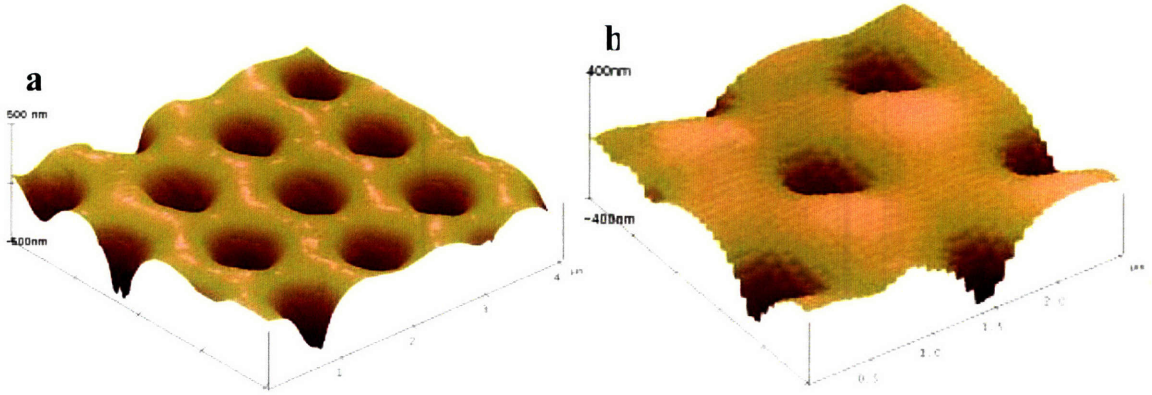

Figure 3-6. (a) 3D surface topography of the specimen with the hexagonal pattern (4x4 μm^2, the tapping mode) and (b) 3D topography of the surface areas mapped with 32x32 force spectroscopy (2.5x2.5 μm^2); each pixel in the force scan represents one force measurement. The frequency of each measurement was 1 Hz.

AFM, high-resolution topographical images were simultaneously obtained with nanomechanical property (modulus) images (shown as a 32x32 array of small square pixels) and were very similar to those images obtained with conventional tapping mode scanning (Fig. 3-7(a)). In the course of AFM micromapping, the AFM tip indented the surface in the center of this area, pulled off, and moved to a neighbor surface area for the next test. The force-distance data obtained were converted to the loading curve (load vs indentation depth) for the evaluation of the surface stiffness and calculation of the elastic modulus by applying the Hertzian model of the elastic deformation by semi-spherical indenter interacting with planar elastic solid (see details in section 2.4).

We selected two surface areas representing beams and nodes which excluded the surface areas in the vicinity to the holes (Fig. 3-7(a)) and calculated statistical distribution of the elastic moduli for these areas (Fig. 3-7(b)). The average elastic modulus obtained from the histograms for the nodes was 1480 ± 460 MPa, which was higher than that calculated for the beam areas, 1120 ± 590 MPa. This tendency of the variation in elastic moduli was always observed in testing different equivalent spots in the sample. The difference in the elastic moduli was not significant but this weak variation between nodes and beams was expected from the fundamental mechanics of crosslinked polymers since noncrystalline polymers do not have a strong dependence of elastic modulus on the crosslink density below the glass transition temperature.

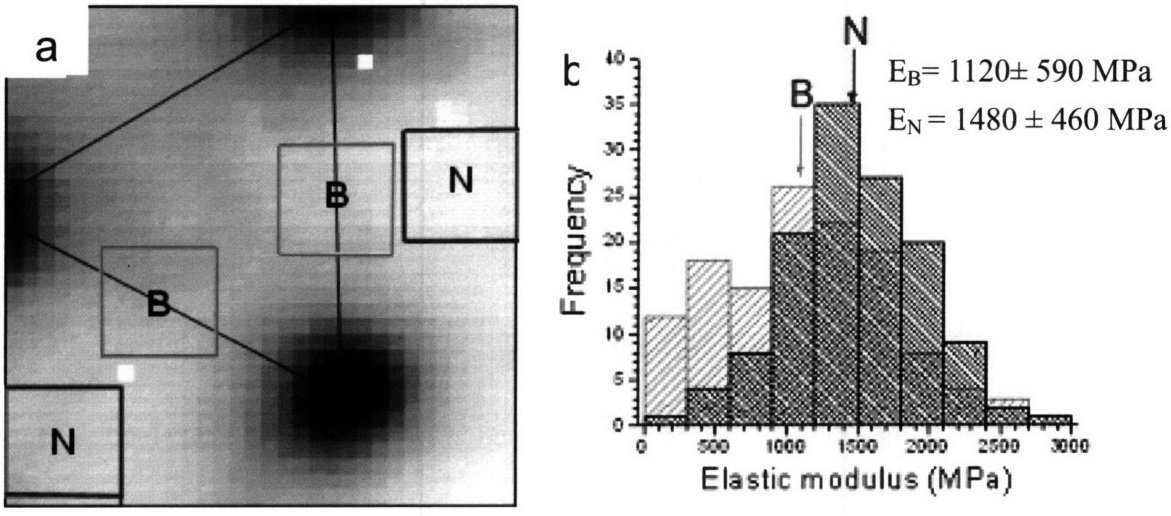

Figure 3-7. (a) 32x32 high-resolution AFM topography during force micromapping of the 2x2 μm^2 surface area. (b) Combined surface histograms collected for selected surface areas (500x500 nm^2) for nodes (black boxes) and beams (grey boxes).

We suggest that the observed location-dependent variation of the elastic moduli is caused by the spatial variation of the material properties "templated" by the light distribution within the interference pattern.[16] The variable light distribution results in variable crosslink density and hence corresponding materials properties such as elastic modulus, glass transition, or plasticity behavior.[11, 17, 18] In IL, crosslink density depends on dose, cure conditions and the distribution of the amine compensator. In fact, the close to linear relationship between the exposure dose and the crosslink density above the dissolution threshold is confirmed in this study by microprobing SU8 materials uniformly exposed to light doses (532 nm Nd:YAG laser) from 0.38 to 3.8 J/cm^2 in Figure 3-8. Four cured SU8 samples with exposure to be the green laser were prepared with different light doses (0.38, 0.76, 2.28 and 3.80 J/cm^2) and then tested by AFM nanoindentation. The average elastic modulus from each sample is plotted in Figure 3-8. Even though we do not have many dose points, the results suggest an initial linear relationship between the elastic modulus from the crosslink density and exposure dose before reaching a plateau. The plateau region showed that the crosslink density and the following elastic modulus are fully saturated above a certain amount of light energy. The value of elastic modulus also matches well with the value (3.4 GPa) of the cured uniformly exposed SU8 films in section 3.2.

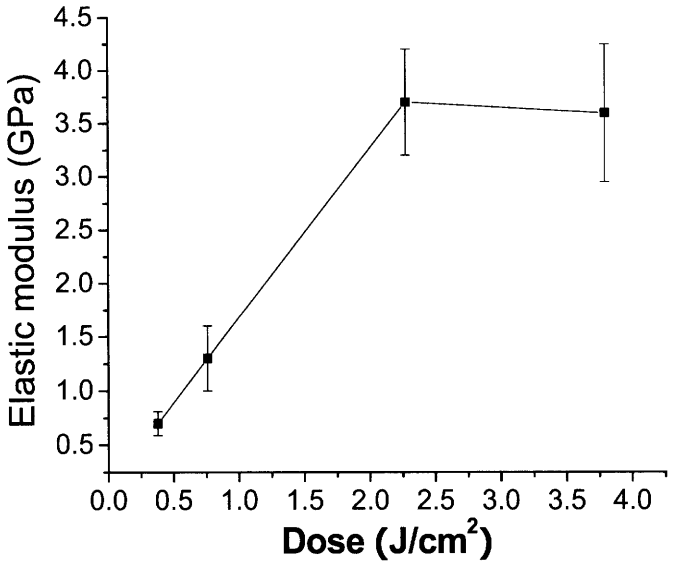

Figure 3-8. The linear relationship before obtaining a certain light energy and the plateau after saturation of crosslinking between elastic modulus and exposure dose obtained by AFM force measurement. Error bars represent less than 20% standard deviation.

3.4 Conclusion

The 2D hexagonal-photopatterned films fabricated here can be considered as composite networks with potentially unique properties associated with the non-uniform distribution of elastic properties imprinted by the interference pattern. In fact, we observed interesting plastic deformation of shear and bending in these perforated films in Figure 3-9. SU8 films are capable of high plastic behavior with significant local deformation of individual cells and large scale deformation of the whole net. Although this unusual behavior requires further investigation, we can speculate that precise control of the non-uniform internal elastic properties within IL-microfabricated polymer structures makes these structures highly deformable and opens potential paths for

photopatterned polymeric materials with efficient energy absorption on a sub-micrometer scale.

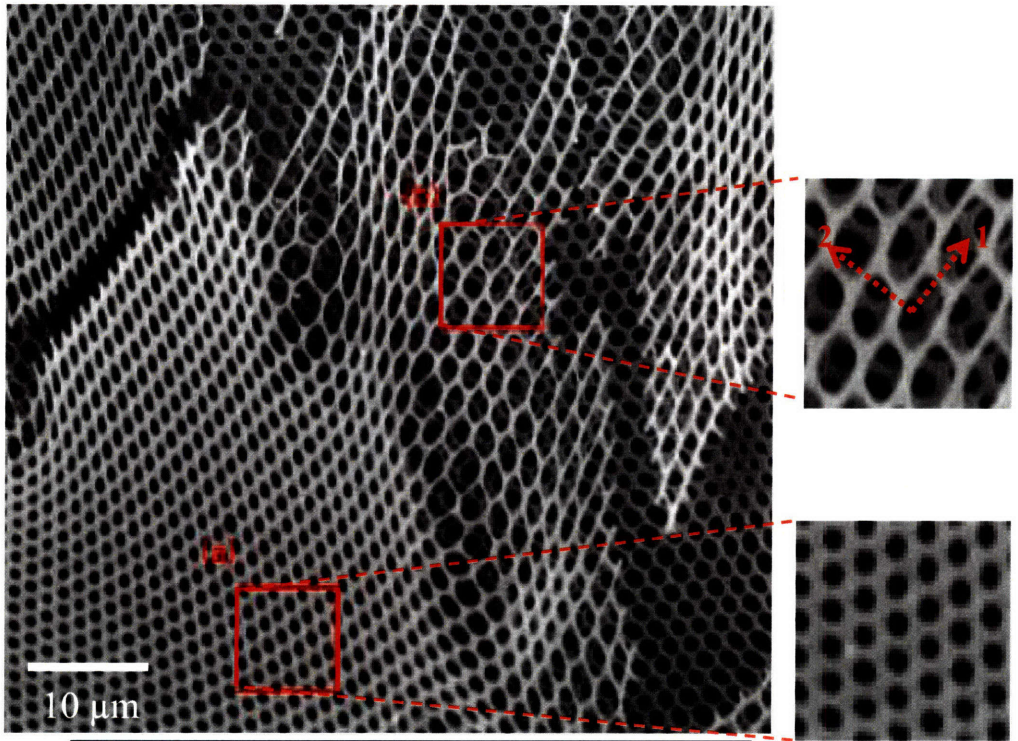

	Porosity (ρ)	Strain1, ε1	Strain2, ε2
Fig. 3-9(a)	0.26	0	0
Fig. 3-9(b)	0.52	2.26	0.84

Figure 3-9. SEM micrograph of a stretched and twisted polymer (the first layer is on top of the undeformed underlying layer) with a 2D hexagonal air-cylinder pattern, demonstrating regions with large plastic behavior. Comparing locations (a) and (b), we estimate a local strain up to 230 % in largely deformed locations as described in the table.

3.5 Future work

In this chapter, we have measured the elastic modulus of 2D air-cylinder and SU8 structure via AFM nanoindentation at $T_{testing} < T_g$. The difference in elastic modulus according to the light intensity distribution was not big. It is of interest to investigate the same structures of different materials such as elastomeric materials in order to see differences at $T_{testing} > T_g$. Elastomers are interesting with their low glass transition temperatures for AFM nanoindentation and dynamic tensile testing.

3.6 References

1. Feng, R. and Farris, R. J., "Influence of processing conditions on the thermal and mechanical properties of SU8 negative photoresist coatings". *J. Micromech. Microeng.* **13**, 80-88 (2003).
2. Yu, H., Balogun, U., Li, B., Murray, T. W. and Zhang, X., "Building embedded microchannels using a single layered SU-8, and determining Young's modulus using a laser acoustic technique". *J. Micromech. Microeng.* **14**, 1576-1584 (2004).
3. Rath, S. K., Boey, F. Y. C. and Abadie, M. J. M., "Cationic electron-beam curing of a high-functionality epoxy: effect of post-curing on glass transition and conversion". *Polym. Int.* **53**, 857-862 (2004).
4. Hong, G., Holmes, A. S. and Heaton, M. E., "SU8 resist plasma etching and its optimisation". *Microsyst. Technol.* **10**, 357-359 (2004).
5. Nguyen, N. T. and Truong, T. Q., "A fully polymeric micropump with piezoelectric actuator". *Sens. Actuator B-Chem.* **97**, 137-143 (2004).
6. Sperling, L. H., *Introduction to Physical Polymer Science* (Wiley-Interscience, 2001).
7. Seet, K. K., Mizeikis, V., Matsuo, S., Juodkazis, S. and Misawa, H., "Three-dimensional spiral-architecture photonic crystals obtained by direct laser writing". *Adv. Mater.* **17**, 541-+ (2005).
8. Plepys, A., Vratsanos, M. S. and Farris, R. J., "Determination of Residual-Stresses Using Incremental Linear Elasticity". *Compos. Struct.* **27**, 51-56 (1994).

9. Bohl, B., Steger, R., Zengerle, R. and Koltay, P., "Multi-layer SU-8 lift-off technology for microfluidic devices". *J. Micromech. Microeng.* **15**, 1125-1130 (2005).
10. Chizhik, S. A., Huang, Z., Gorbunov, V. V., Myshkin, N. K. and Tsukruk, V. V., "Micromechanical properties of elastic polymeric materials as probed by scanning force microscopy". *Langmuir* **14**, 2606-2609 (1998).
11. Feng, R. and Farris, R. J., "The characterization of thermal and elastic constants for an epoxy photoresist SU8 coating". *J. Mater. Sci.* **37**, 4795-4801 (2002).
12. Lorenz, H., Despont, M., Fahrni, N., LaBianca, N., Renaud, P. and Vettiger, P., "SU-8: a low-cost negative resist for MEMS". *J. Micromech. Microeng.* **7**, 121-124 (1997).
13. Campbell, M., Sharp, D. N., Harrison, M. T., Denning, R. G. and Turberfield, A. J., "Fabrication of photonic crystals for the visible spectrum by holographic lithography". *Nature* **404**, 53-56 (2000).
14. Ullal, C. K., Maldovan, M., Thomas, E. L., Chen, G., Han, Y. J. and Yang, S., "Photonic crystals through holographic lithography: Simple cubic, diamond-like, and gyroid-like structures". *Appl. Phys. Lett.* **84**, 5434-5436 (2004).
15. Yang, S., Megens, M., Aizenberg, J., Wiltzius, P., Chaikin, P. M. and Russel, W. B., "Creating periodic three-dimensional structures by multibeam interference of visible laser". *Chem. Mat.* **14**, 2831-+ (2002).
16. Decker, C., Viet, T. N. T., Decker, D. and Weber-Koehl, E., "UV-radiation curing of acrylate/epoxide systems". *Polymer* **42**, 5531-5541 (2001).
17. Simonin, L., Zissi, S., Gonnet, J. P., Hunsinger, J. J., Corbel, S. and Lougnot, D. J., "Characterization of heterogeneous structure in a polymer object manufactured by stereolithography with low-frequency microechography". *J. Mater. Chem.* **6**, 1595-1599 (1996).
18. Zhang, J., Chan-Park, M. B. and Conner, S. R., "Effect of exposure dose on the replication fidelity and profile of very high aspect ratio microchannels in SU-8". *Lab Chip* **4**, 646-653 (2004).

Chapter 4. Length Scale Dependence of 3D Polymeric Microframe Deformation*

In the previous chapter, we observed the microscopic spatial distribution of out-of-plane elastic modulus in a 2D hexagonal air-cylinder and polymer film. In addition to the local elastic properties of the 2D periodic structure, in this chapter we extend our investigation to the plastic behavior of 3D submicron-scale periodic microframe fabricated in the epoxy SU8 via four-beam interference lithography (IL). We fabricated a three-dimensionally designed and structured air-polymer composite, characterized the mechanical behavior of the structure and observed symmetry-guided fracture and plastic deformation. An unusual plastic behavior was observed for the 3D microframe. The structure exhibits a length scale dependence of the deformations unlike the brittle behavior of bulk SU8.

The large area (5 mm diameter), periodic and porous polymer/air structures are fabricated from negative Novolak-resin photoresist and due to their length scale dependent mechanical behavior, exhibit interesting deformational characteristics (e.g. necking of crosslinked struts and their evolution into long fibrils) with ultimate strains reaching ~ 300 %, much higher than the strains attainable in bulk films of either the fully

* This chapter is based on a paper published in *Adv. Mater.* **18**, 2123-2136 (2006).

crosslinked solid polymeric material or the glassy monomer precursor. The unique deformation and fracture behavior of the polymer networks reported here demonstrates the promise of rational design and fabrication of lightweight bicontinuous network nanocomposite materials via IL.

4.1 3D Microframe: Design, Fabrication and Mechanical Applications

Materials science, especially metallurgy has long exploited the relationship between submicron length scale arising from various processing routes and resultant properties with increasing emphasis on the benefits of ultra-fine scale structures. Critical elements for the design of lightweight materials for mechanical applications include means for stiffening, strengthening as well as providing energy absorption and controlled crack propagation.[1-4] Combinations of hard and soft components, control over component size, shape, and arrangement, and attention to interfacial strength are widely used to design composite materials with superior properties.

Man-made ordered composites are typically assembled via machine or hand lay-up and generally rely on macroscopic components. On the other hand, load bearing structures in nature are much more complex, often using a combination of hard (e.g. calcite) and soft (e.g. proteins) components and importantly, feature elegant self organized hierarchical designs extending from the nanometer to the mm scale.[5]

Moreover, nature has evolved certain structures into nearly optimized mechanical designs.[6] Most of the current man-made submicron scale composites provide little control over the detailed microstructure of the respective components.[7] For example, recent efforts on polymer-carbon nanotube composites currently lack the processing ability to pattern the components at various length scales to create optimally designed materials. Patterning by self assembly is one means to mimic nature but at present most ordered structures occur more by happenchance than by purposeful design and the pattern is achieved normally only at one length scale. Taking advantage of length scale dependent mechanical properties is another strategy used by nature to tailor mechanical behavior.[5] Polymeric materials in particular are also sensitive to the influence of sample dimensions on properties, for example, below a critical film thickness, brittle polymers can exhibit increased strain to break and improved toughness.[8, 9]

Lightweight microframe structural materials possessing load bearing capabilities approaching those theoretical limits have recently been constructed from millimeter size metallic assemblies.[10] Their open architecture provides for a density well below 10 % of that for the corresponding bulk materials.[11] Several structures have been fabricated, tested, and theoretically analyzed. However, for feature sizes at the millimeter scale, the material's mechanical properties are not size dependent, indeed, theoretical models that

rely only on inputting a constitutive equation based on bulk material behavior along with the particular truss geometry do a very good job of capturing the experimentally observed behavior. Designs that provide conditions such that beams are under compression or tension while avoiding bending, which are defined as microtrusses in section 2.1 are desired for stiffness and strength. In particular pyramidal and octahedral frame structures provide maximum stiffness and strength at a given density.[12] In addition to outstanding specific mechanical properties, the open structure and high surface area [m^2/g] of microframes add additional functionality such as the ability to cool by flowing a continuous fluidic phase through the structure.[13]

Recent developments in laser IL demonstrate the ability for fast fabrication of complex polymeric structures with long-range periodic order.[14] IL can create connected submicron sized elements in complex 2D and 3D networks (all possible crystal lattice symmetries)[15] with micron to submicron spacings. Such periodic structures created with IL are being pursued for photonic[14-16] and phononic[17] applications. Periodic high porosity polymeric structures are also attractive candidates for mechanical applications. The polymeric material used for the "skeleton" network of members exhibits appropriate mechanical properties, and the chosen geometry of the 3D structure provides proper mechanical load distribution.

4.2 Fabrication of 3D Polymer Microframes via IL

We use holographic IL to fabricate a 3D polymer microframe having a four-functional network geometry with submicron periodicity, low density (~ 0.3 g cm^{-3}) and 200 nm feature size. As a first attempt to fabricate and mechanically test a 3D polymer microframe, we used multiple IL to pattern Novolak-resin (SU8). SU8 is widely used as a robust negative photoresist for microelectromechanical devices.[18] The details about the material, SU8, and IL procedure are described in section 2.2. The glass support was treated with a thin (700 nm) buffer layer of pre-crosslinked SU8 material to assure firm attachment of the structured polymer film to the substrate via chemical grafting to enable subsequent mechanical peeling experiments. The exposure was done using a 532 nm Nd:YAG laser and the Gaussian output was converted into a flat top function using a refractive beam shaper. By post-exposure baking of the 8.5 μm-thick film (thickness measured with profilometer, P10 Tencor Surface Profiler) the resultant cationic photopolymerization takes place in regions that were exposed to high intensities of light. To avoid collapse of the 3D microframe structure, CO_2 supercritical drying is applied after developing the uncured regions to yield the final 3D porous microframe structure over areas as large as 5 mm in diameter.

Our 3D microstructure is an elongated IL variant of the classic Yablonovite

photonic structure[19] with a symmetry close to that of the space group #166, $R\bar{3}m$. The final directions and polarizations of the beams inside the photoresist are given by:

$$\vec{k}_0 = [0.0112, 0.0112, 0.0112], \quad \vec{E}_1 = [0, -5.74, 5.74],$$

$$\vec{k}_2 = [0.0073, 0.0164, 0.0073], \quad \vec{E}_2 = [0, -2.45, 2.45],$$

$$\vec{k}_3 = [0.0073, 0.0073, 0.0164], \quad \vec{E}_3 = [-0.97, -2.97, 1.75],$$

$$\vec{k}_3 = [0.0073, 0.0073, 0.0164], \quad \vec{E}_3 = [-0.97, -2.97, 1.75],$$

The structure is a four-functional network and can be envisioned as a type of continuously joined set of polymer nodes and members, having a basic unit comprised of a thick vertical post (L/D ~ 2.3) supporting three thinner struts (L/D ~ 3.2) where L is the length and D is the diameter (see Fig. 4-1).[20] The structure is defined by the distribution of crosslinks in the photoresist arising from the light intensity distribution determined by the laser beam parameters (directions, polarizations, amplitudes and phases). For the present IL defined network members having aspect ratios of only 2-3, transverse loads create shear stresses across the members in addition to bending.

To gain a better understanding of our structure, the theoretical light distribution at different sections of the unit cell as well as the corresponding schematic views of different orientations of the theoretical 3D structure are presented in Figure 4-1(a) and (b). The high intensity regions of the interference pattern result in regions of high

crosslink density, while dark regions correspond to low crosslink density, as we studied in chapter 3. During the development process, the weakly crosslinked material is removed, leaving a connected pore space between the crosslinked epoxy regions.[21] The unit cell is comprised of three layers illustrated by the different colors in Figure 4-1(c). The section at height $\frac{2}{3}c$ shows the successive lateral shift of the basic motif. The view along [0 0 0 1] shows a 3-fold pattern of members and nodes with the color indicating the height in the unit cell (see Fig. 4-1(b)). SEM images of planes perpendicular to [1 1 $\bar{2}$ 0] and [0 0 0 1] show good correspondence between the SU8 structure and the theoretical model (compare Figs. 4-1(b), 4-1(c) with the insets in 4-1(e)). The overall 8.5 μm-thick microframe polymer film includes 2 unit cells with six sub layers composed of staggered vertical posts with average height of 1400 nm, diameter of 500 nm and spacing of 980 nm as evaluated from the side view (Fig. 4-1(e)). We estimate sample porosity at about 70 % by comparison of SEM images with various level set representations of the structure and from assigning sizes to the struts and computing the volume fraction occupied by the epoxy network in the unit cell.

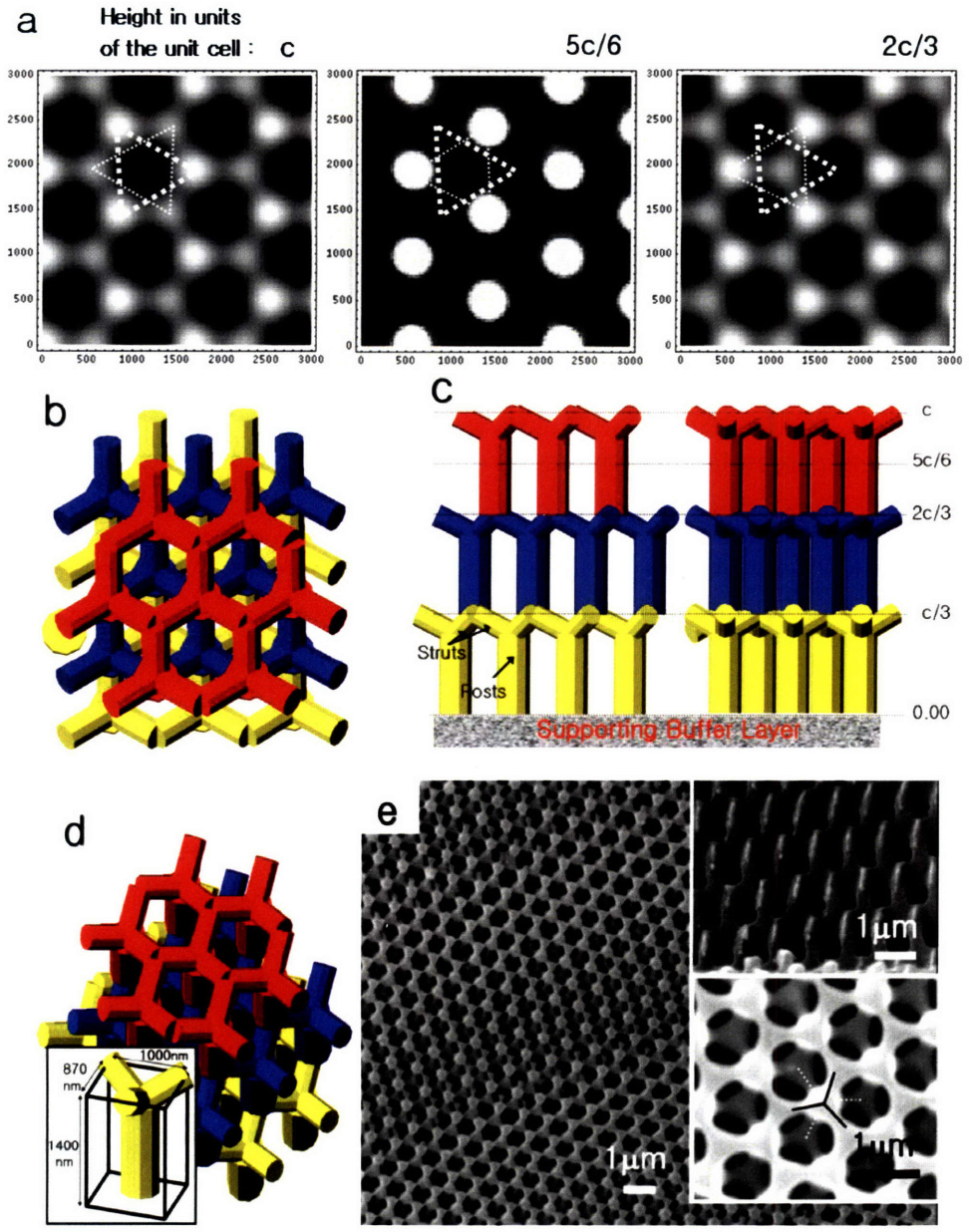

Figure 4-1. Microframe polymer structures fabricated by 3D interference lithography. (a) Theoretical 2D light intensity distributions at various heights within the unit cell (the middle image is binarized to correspond to the final developed structure). The triangles are for locating the same region in each image (b) View normal to the (0001) plane of the microframe structure. The colors correspond to struts at c/3, 2c/3 and c. (c) Views normal to the (1 1 $\bar{2}$ 0) and (1 0 $\bar{1}$ 0) planes of the microframe structure. (d) Perspective view of the structure with the basic four-functional element as the inset. The sub cell dimensions are ~ 1400 nm x 1000 nm x 870 nm. The three thinner struts have a diameter about 200 nm and length of 640 nm and the thicker vertical post has a diameter of 500 nm and length of 1100 nm. (e) SEM image of the 3D-microframe fabricated in SU8. The insets show magnified views of the top (lower right) and cross sectional (upper right) surfaces corresponding to the schematic views in b and c.

4.3 Length Scale Dependence on the Mechanical Behavior of the Microframe

In order to make a preliminary assessment of the deformation behavior of the microframe film, we employed a simple peeling process that involves applying adhesive tape to the structure and peeling off a portion of the film. The remaining film is then transferred onto carbon tape and mounted in an SEM holder. Peeling involves a complex interplay of forces and allows us to observe the mechanical response of the microframe structure in a wide variety of deformational modes. We thus see the effect of tension, bending, compression, and shearing on our sample. Inspection of the film (see Fig. 4-2, 4-3) reveals a host of interesting morphologies related to fracture and various types of deformation.

Features associated with failure include long, straight, micron-wide cracks following easy fracture directions (Fig. 4-2(a) and (b)) and penny shaped cracks extending inwards from the surface towards the substrate (Fig. 4-2(c)). The planes of easy fracture are parallel to the thick post and always involved the failure of the thinner transversely oriented struts in accordance with the 3-fold symmetry in the [0 0 0 1] planes.

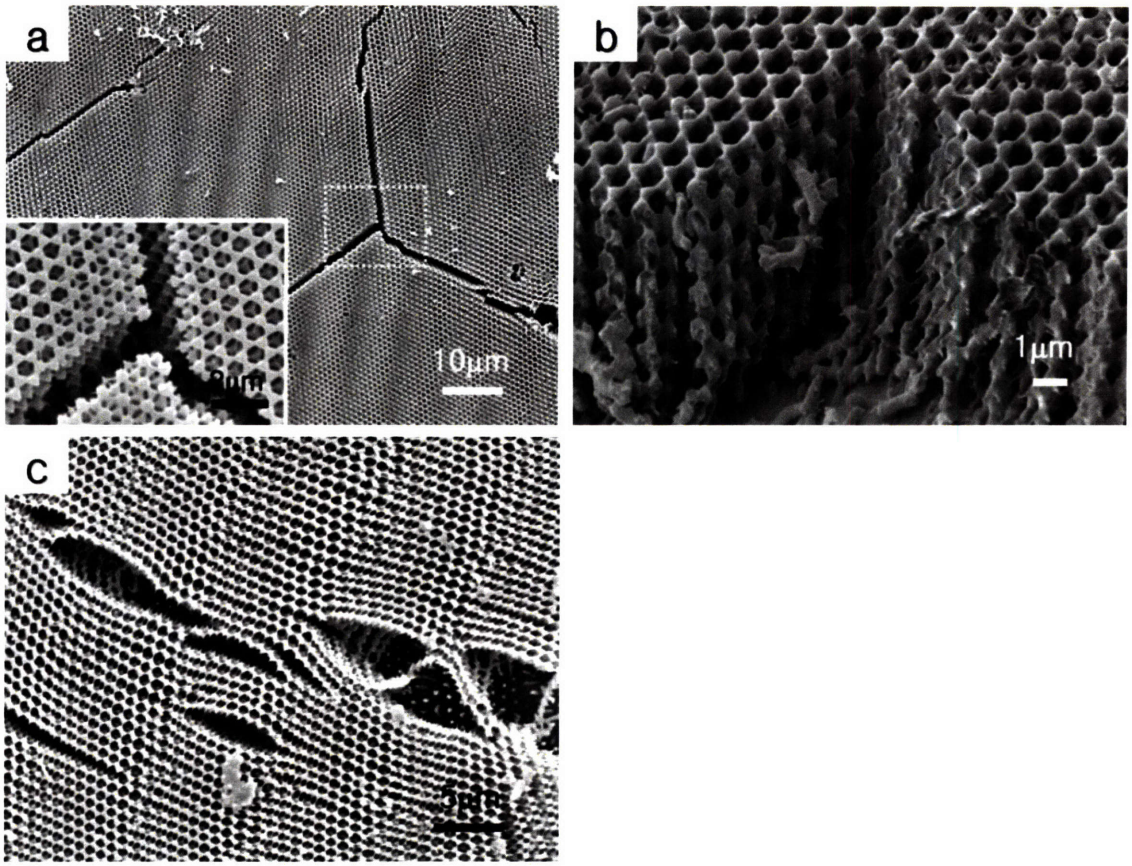

Figure 4-2. SEM images of fracture within the polymer microframe. (a) Region where cracks are guided by planes of easy fracture with 3-fold symmetry. (b) View showing a region with intersecting $\{1\ 1\ \bar{2}\ 0\}$ facets with an apex angle of 60 degrees. (c) Region where surface-initiated cracks penetrate towards the substrate.

Unusual behavior is observed while examining the modes of failure of the thinner members. Here we observe portions of microframe bridging across wide cracks (Fig. 4-3(a)), highly stretched members in front of arrested cracks (Fig. 4-3(b)), and crushed and densified areas in regions of compression (Fig. 4-3(c)). The diameter of the most highly stretched members decreases to approximately 70 nm from the original 200nm. By comparison of the strut length in unperturbed unit cells with those in deformed regions, member strain can be estimated and is upwards of 300 % (see elongated members in Fig.

4-3(b)). The strain to failure of the 100 nm features is about an order of magnitude higher than that observed for uncured ($\varepsilon_f \sim 30$ %) and for fully crosslinked Novolak resins ($\varepsilon_f \sim$ 8-10 %).[22] The plasticity of the fine scale structure is further evidenced in the formation of fibrils in regions of high extension, due to pull out and alignment of posts and struts (Fig. 4-3(d) and (e)).

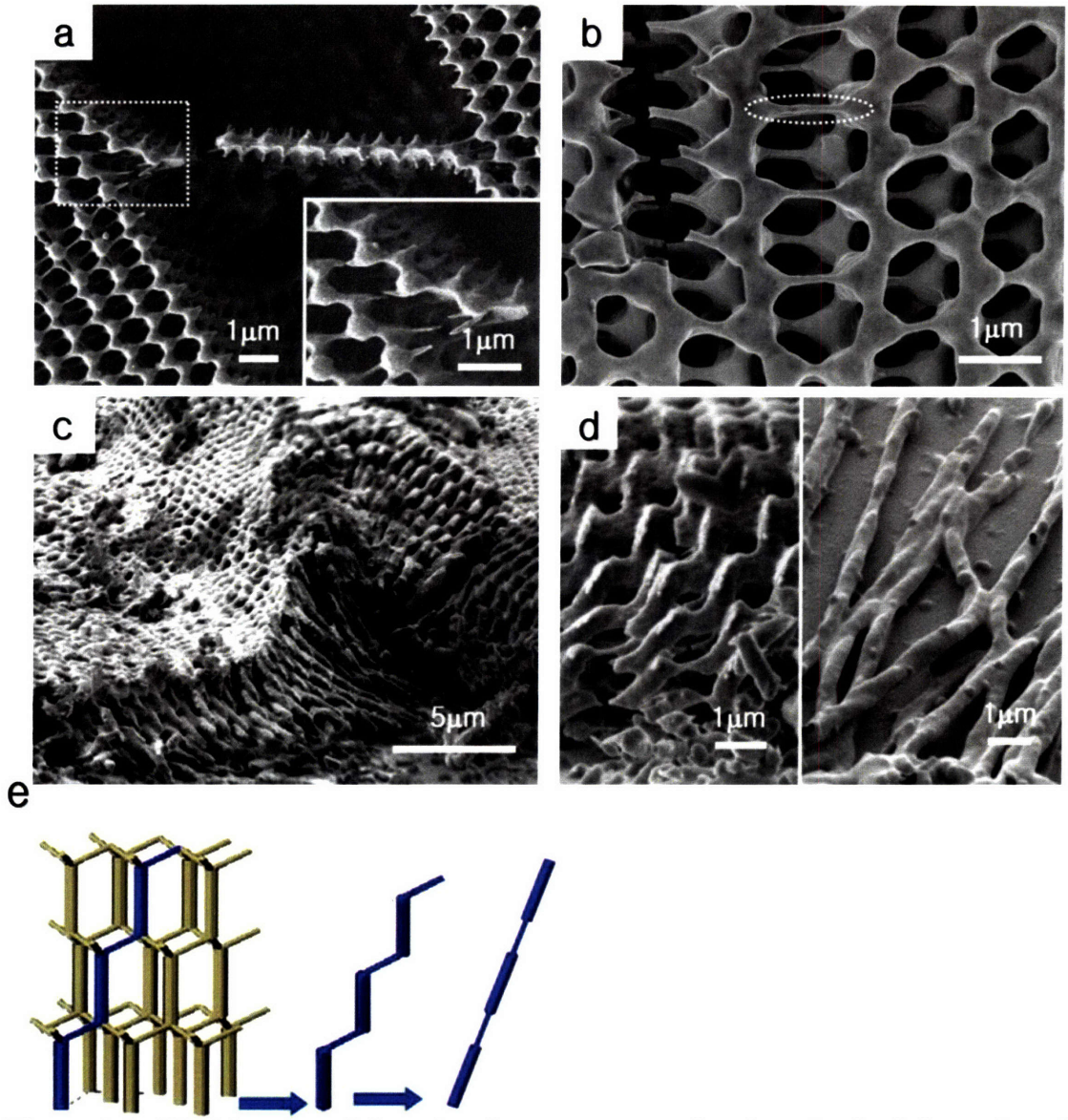

Figure 4-3. SEM images of the microframe structure showing plastic deformation. (a) Area with a microframe bridge extending from one side of a crack to the other. The inset shows extensive shear, bending and microplastic deformation of the structure near the left terminus of the bridge. (b) Evidence of tensile deformation and fracture of transverse struts with up to several hundred % strain (e.g. circled strut) in the vicinity of a crack. The local strain can be estimated based on the departure of the strut and node pattern from the initial undeformed unit cell structure (right side of image). (c) Portion of film that was compressed, showing the collapsed microframe region at left. (d) (left) Cross section of a region of the film where the structure has been plastically deformed. (right) Fibrils formed due to peeling of microframe from substrate. (e) Schematic depicting how long fibrils form via stretch-alignment of vertical and transverse struts.

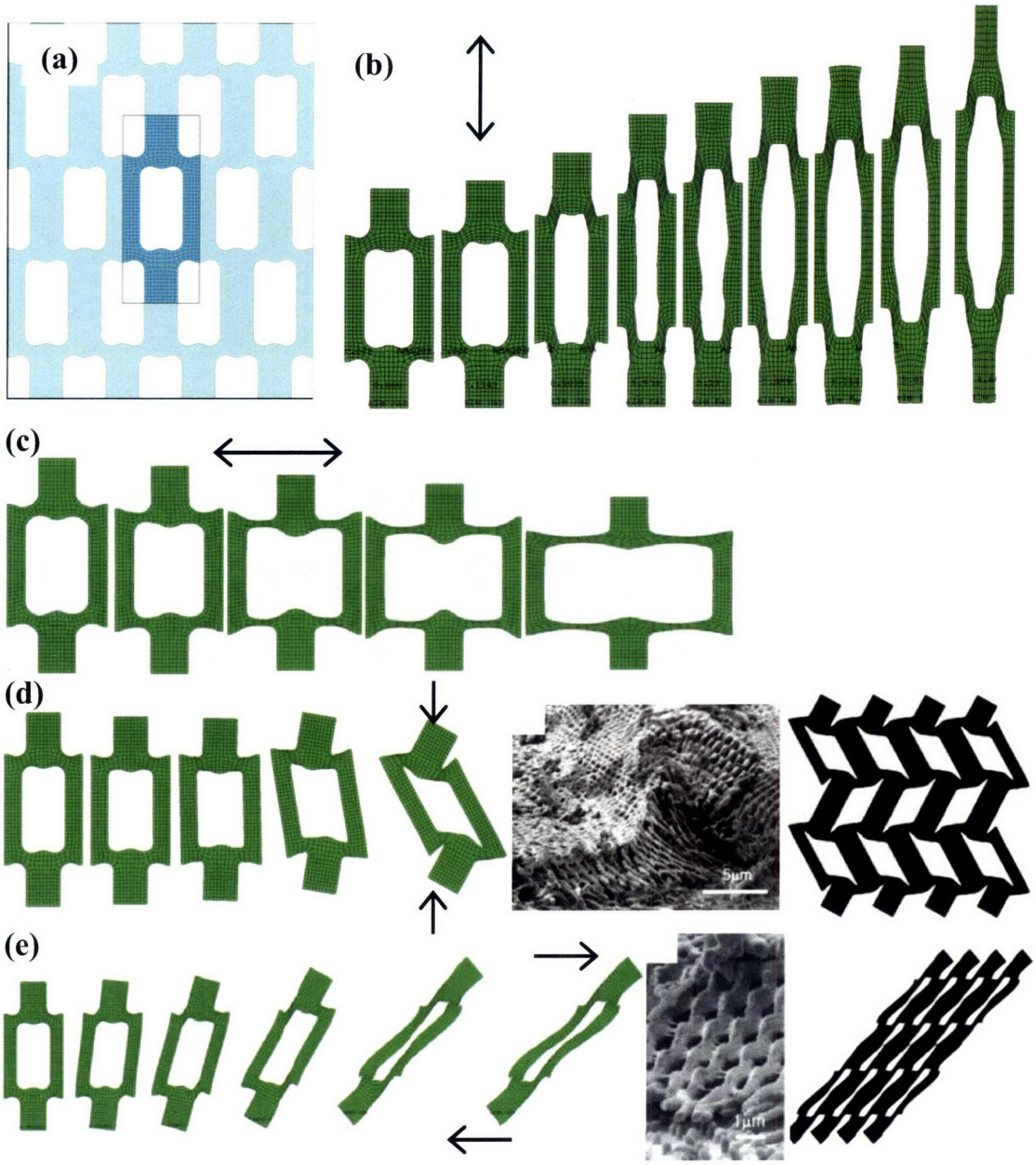

Figure 4-4. (a) A Representative Volume Element (in the center box) of the 3D microframe by applying a 2D micromechanical model with periodic boundary conditions under multiaxial loading. (b) The predicted deformation under a tension along the thick post direction (0°). (c) The predicted deformation under a tension along the perpendicular to the thick post (90°). (d) The predicted deformation under a compression explains the observed SEM micrograph with the deformed RVEs. (e) Applying shear to the RVE represents the deformation of elongated fibrils on the substrate. Arrows in each figure show the loading direction. Modeling conducted by Dr. Lifeng Wang in professor Mary C. Boyce in mechanical engineering at MIT.

To understand and predict the multiaxial large deformation behavior, we developed a 2D micromechanical model for our microframe structural polymer. Having a basic unit of a four-functional element as shown in Figure 4-1 (d), we defined a representative volume element (RVE) in 2D finite element modeling in Figure 4-4 (a). Each RVE is spatially periodic and there is no separation or overlap between the neighboring RVEs. When such an RVE is subjected to macroscopic loading of deformation history, periodic boundary conditions must be applied to the surface of RVE. The large-strain elastic-viscoplastic behavior of glass polymer[23, 24] was applied for matrix constitutive behavior. With inputs of geometry, constitutive behavior and materials constants of SU8, we investigated the response and underlying local deformation under various loading conditions. Figure 4-4 (b-e) shows the predicted deformations in time under tension with two different directions (0° and 90°), compression and shear. Under a tension (Fig. 4-4(b)), the thin beams firstly start to deform and undergo neck-formation and then, the thick posts deform afterwards. At several necking points, we observed sudden stress drops in stress-strain curves (not shown). The deformations by the modeling of compression and shear in Figure 4-4(d) and (e) elucidate well SEM micrographs we observed under the complicated applying force.

In Figure 4-5 two SEM micrographs recapitulated the interesting deformation

behavior of SU8 3D microframe within several hundred μm^2. Shown in Figure 4-5(a), by tension forces struts were elongated, broken, contracted and bent after breaking, and the penny-shape crack formation from the surface were observed within the area of 100 μm^2. In Figure 4-5(b), the half of the region where the structure remained exhibits compression and shear as the 2D micromechanical modeling demonstrated. In the other half where some parts of 3D microframe were removed, we observed that the residual SU8 on the substrate preserves the symmetry and some of the struts were drawn and made as self-supporting pillars. With these evidences, we are able to say that the periodic microframe undergoes substantial energy absorption through various deformation modes.

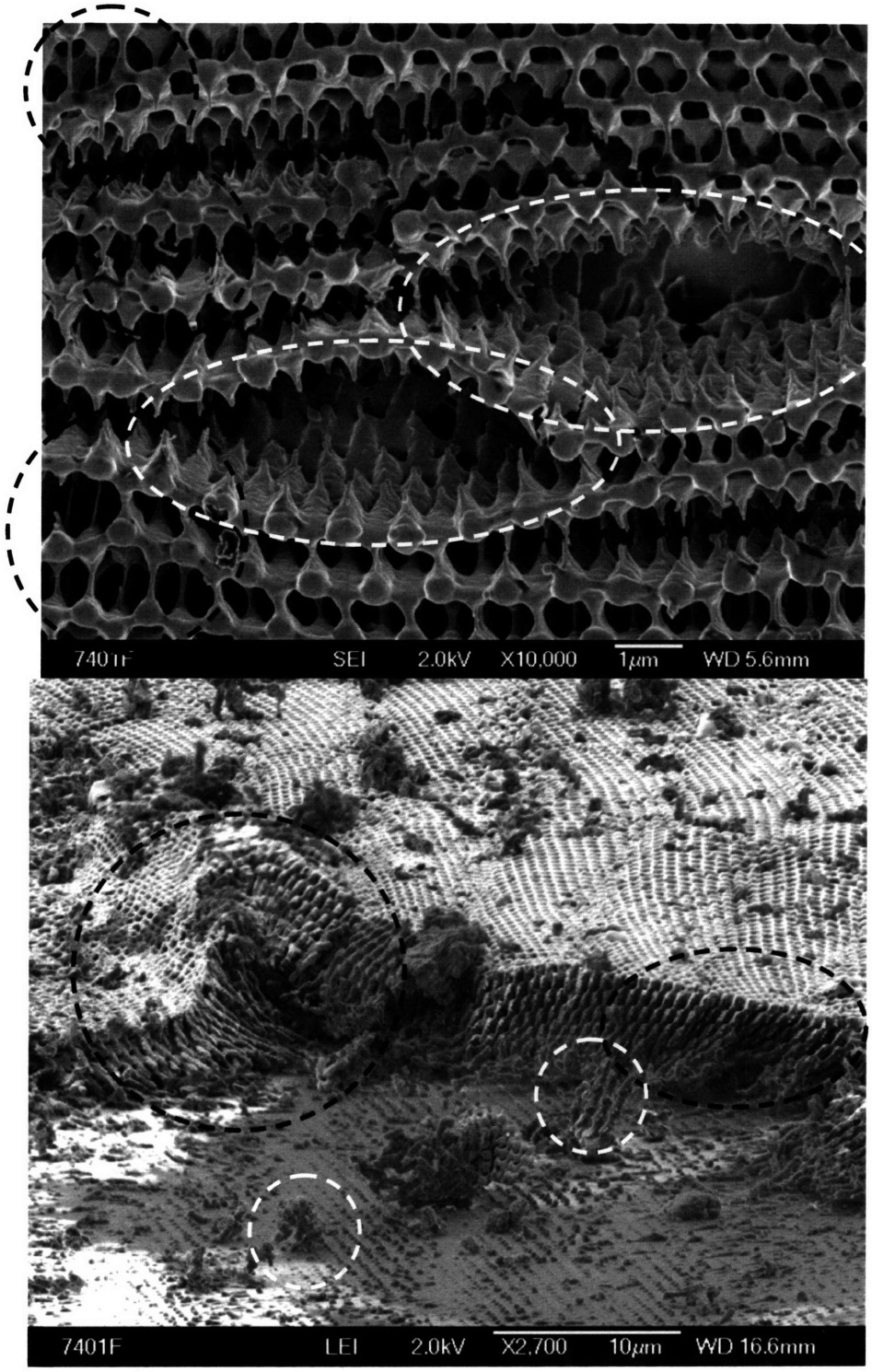

Figure 4-5. SEM micrographs of multiaxial loading on the 3D periodic microframe; most of predicted deformations from 2D micromechanical modeling were observed in a single SEM image. (a) In this SEM image SU8 microframe exhibits strut-stretching and contraction after break (black circles), penny-shape crack formation (white ellipses) where has extended, broken, bent and contracted struts, neck-forming (white circles and ellipses) by overall tension. (b) Compression, shear (black circles) and residual pillars adhered to the substrate were shown in the SEM micrograph.

We can explain the highly ductile failures of the normally brittle SU8 epoxy primarily as a result of two effects: *the creation of the very small diameter epoxy members* and *attainment of an intermediate crosslink density*. Kramer's group has shown for glassy amorphous polymers that below a critical film thickness (~100 nm-1000 nm), the strain to break can approach the maximum expected draw ratio of the entanglement network[8] or crosslinked network.[25] Van der Sanden and Meijer[26] investigated a thermosetting polymer and found a similar critical ligament thickness, below which the strain to failure greatly increased. For highly crosslinked SU8 material, the glass transition temperature is 230 °C[27], compared to 55 °C for the uncured monomer.[22] The glass transition temperature determined by DSC of our structured polymer film was approximately 100 °C consistent with partially crosslinked material. Thermal properties and extent of crosslinking were evaluated by a TA instruments Differential Scanning Calorimeter (Q 1000) by scanning from 30 °C to 250 °C with a heating rate of 20 °C min^{-1} under a nitrogen purge. Samples for DSC were collected by scraping the crosslinked film from the substrate. In order to eliminate the possibility of the behavior being due to the presence of solvent, we conducted spectroscopic studies (Total Reflectance Fourier Transform Infrared Spectra (ATR FT-IR mode) using NEXUS 870 FT-IR (Thermo Nicolet)), which revealed no detectable residual solvent after developing and drying

(supercritical CO_2).

4.4 Conclusion

Periodic microframe structures can direct crack propagation along *certain crystallographic directions* and also exhibit *enhanced plastic response.* The remarkable large plastic deformation exhibited in the microframe structure derives from the hundred nm length scale of the individual members, facilitated by crosslink density gradients in the epoxy, with the more highly crosslinked nodes being less deformable than the less densely crosslinked struts.[28] Deformation mechanisms characteristic to a nanoscale structure combined with a purposeful mechanical design suggest a pathway for creating new ultra light, mechanically dissipative structures.

4.5 References and Notes

1. Ashby, M. F., *Materials Selection in Mechanical Design* (Butterworth-Heinemann, 1999).
2. Creton, C., Kramer, E. J., Brown, H. R. and Hui, C. Y."Adhesion and fracture of interfaces between immiscible polymers: From the molecular to the continuum scale", in "Molecular Simulation Fracture Gel Theory", *Advances in Polymer Science*, 53-136 (2002).
3. Gibson, L. J. and Ashby, M. F., *Cellular Solids: Structure and Properties* (Cambridge University Press, Cambridge, UK, 1999).
4. Young, R. J., *Crack Propagation in Thermosetting Polymers: Developments in Reinforced Polymers* (Applied Science, 1980).
5. Aizenberg, J., Weaver, J. C., Thanawala, M. S., Sundar, V. C., Morse, D. E. and Fratzl, P., "Skeleton of Euplectella sp.: Structural hierarchy from the nanoscale to the macroscale". *Science* **309**, 275-278 (2005).

6. Deshpande, V. S., Ashby, M. F. and Fleck, N. A., "Foam topology bending versus stretching dominated architectures". *Acta Mater.* **49**, 1035-1040 (2001).
7. Kim, J. K. and Mai, Y. W., "High-Strength, High Fracture-Toughness Fiber Composites with Interface Control - a Review". *Compos. Sci. Technol.* **41**, 333-378 (1991).
8. Berger, L. L., "On the Mechanism of Craze Fibril Breakdown in Glassy-Polymers". *Macromolecules* **23**, 2926-2934 (1990).
9. Van der Sanden, M. C. M., Meijer, H. E. H. and Lemstra, P. J., "Deformation and Toughness of Polymeric Systems: 1. The Concept of a Critical Thickness". *Polymer* **34**, 2148-2154 (1993).
10. Wadley, H. N. G., Fleck, N. A. and Evans, A. G., "Fabrication and structural performance of periodic cellular metal sandwich structures". *Compos. Sci. Technol.* **63**, 2331-2343 (2003).
11. Tian, J., Kim, T., Lu, T. J., Hodson, H. P., Queheillalt, D. T., Sypeck, D. J. and Wadley, H. N. G., "The effects of topology upon fluid-flow and heat-transfer within cellular copper structures". *Int. J. Heat Mass Transf.* **47**, 3171-3186 (2004).
12. Hyun, S., Karlsson, A. M., Torquato, S. and Evans, A. G., "Simulated properties of Kagome and tetragonal truss core panels". *Int. J. Solids Struct.* **40**, 6989-6998 (2003).
13. Sypeck, D. J. and Wadley, H. N. G., "Multifunctional microtruss laminates: Textile synthesis and properties". *J. Mater. Res.* **16**, 890-897 (2001).
14. Campbell, M., Sharp, D. N., Harrison, M. T., Denning, R. G. and Turberfield, A. J., "Fabrication of photonic crystals for the visible spectrum by holographic lithography". *Nature* **404**, 53-56 (2000).
15. Ullal, C. K., Maldovan, M., Wohlgemuth, M. and Thomas, E. L., "Triply periodic bicontinuous structures through interference lithography: a level-set approach". *J. Opt. Soc. Am. A-Opt. Image Sci. Vis.* **20**, 948-954 (2003).
16. Meisel, D. C., Wegener, M. and Busch, K., "Three-dimensional photonic crystals by holographic lithography using the umbrella configuration: Symmetries and complete photonic band gaps". *Phys. Rev. B* **70** (2004).
17. Gorishnyy, T., Ullal, C. K., Maldovan, M., Fytas, G. and Thomas, E. L., "Hypersonic phononic crystals". *Phys. Rev. Lett.* **94** (2005).
18. Lorenz, H., Despont, M., Fahrni, N., LaBianca, N., Renaud, P. and Vettiger, P., "SU-8: a low-cost negative resist for MEMS". *J. Micromech. Microeng.* **7**, 121-124 (1997).
19. Yablonovitch, E., Gmitter, T. J., Meade, R. D., Rappe, A. M., Brommer, K. D. and

Joannopoulos, J. D., "Donor and Acceptor Modes in Photonic Band-Structure". *Phys. Rev. Lett.* **67**, 3380-3383 (1991).

20. Ullal, C. K., Ph. D. thesis, Dept. of Materials Science and Engineering, Massachusetts Institute of Technology, (Cambridge, 2005).
21. Yang, S., Megens, M., Aizenberg, J., Wiltzius, P., Chaikin, P. M. and Russel, W. B., "Creating periodic three-dimensional structures by multibeam interference of visible laser". *Chem. Mat.* **14**, 2831-+ (2002).
22. Feng, R. and Farris, R. J., "Influence of processing conditions on the thermal and mechanical properties of SU8 negative photoresist coatings". *J. Micromech. Microeng.* **13**, 80-88 (2003).
23. Arruda, E. M., Boyce, M. C. and Quintusbosz, H., "Effects of Initial Anisotropy on the Finite Strain Deformation-Behavior of Glassy-Polymers". *Int. J. Plast.* **9**, 783-811 (1993).
24. Boyce, M. C., Parks, D. M. and Argon, A. S., "Large Inelastic Deformation of Glassy-Polymers .1. Rate Dependent Constitutive Model". *Mech. Mater.* **7**, 15-33 (1988).
25. Berger, L. L. and Kramer, E. J., "The Effect of Temperature on the Transition from Crazing to Shear Deformation in Crosslinked Polystyrene". *J. Mater. Sci.* **23**, 3536-3543 (1988).
26. Van der Sanden, M. C. M. and Meijer, H. E. H., "Deformation and Toughness of Polymeric Systems: 3. Influence of Crosslink Density". *Polymer* **34**, 5063-5072 (1993).
27. Feng, R. and Farris, R. J., "The characterization of thermal and elastic constants for an epoxy photoresist SU8 coating". *J. Mater. Sci.* **37**, 4795-4801 (2002).
28. Choi, T., Jang, J. H., Ullal, C. K., LeMieux, M. C., Tsukruk, V. V. and Thomas, E. L., "The elastic properties and plastic behavior of two-dimensional polymer structures fabricated by laser interference lithography". *Adv. Funct. Mater.* **16**, 1324-1330 (2006).

Chapter 5. Mechanical Properties of 3D Quasiperiodic Nanostructures*

In the previous chapters we investigated the elastic and plastic properties of 2D and 3D periodic structures in epoxy photoresist films and observed the spatial variation of elastic moduli corresponding with light intensity distribution in the 2D hexagonal air-cylinder and polymer structure, and extensive plastic deformation (~300% elongation) for submicron feature sizes in the 3D periodic microframe. Our interests now move to *quasiperiodic* structures of the same SU8 material and same feature size. Using an octagonal-patterned phase mask described in section 2.3, 3D nanostructured quasicrystals (QC) with an octagonal axial symmetry were fabricated in SU8 films. After peeling off from the substrate, the freestanding QC SU8 films with the thin SU8 buffer layer were tested in the microtensile tester to characterize their large strain mechanical properties via stress-strain curves. Additional small strain mechanical characterization was made via Brillouin Light Scattering (BLS) conducted on the QC SU8 films on a thin SU8 buffer layer on a glass substrate by varying the incident angles and orientations. BLS measurements allowed us to verify the isotropic in-plane elastic modulus (E) in the octagonal symmetry and to explore the effect of hardbaking on the modulus.

---

* This chapter is based in part on a paper published in *Adv. Mater.* **19**, 1403-1407 (2007).

5.1 Quasicrystals and Their Properties for Last Two Decades

Discovered in 1984[1, 2], the first quasicrystals were metallic alloys of specific compositions having non-crystallographic multifold rotational symmetries without overall translational symmetry.[3] There are three classes of quasicrystals: 1D quasicrystals (e.g. Fibonacci series), axial (polygonal) quasicrystals being quasiperiodic in 2D and with one periodic direction perpendicular to the quasiperiodic layers, and 3D quasicrystals (icosahedral symmetry).

Metallic alloy quasicrystals have shown interesting physical and mechanical properties associated with their unique structure; they are known for extraordinary hardness and wear resistance, low coefficients of friction and low heat conductivity under certain test conditions.[4-7] Investigations of their mechanical properties have shown that dislocation-controlled mechanisms are responsible for deformation in QC metal films.[7, 8] Due to their extreme hardness and brittleness, without any atomic displacements at ambient temperature, most of these mechanical studies have been performed at high temperatures when quasicrystals become deformable (e.g. T > 500 ℃).[7-9]

QC polymeric materials patterned on submicron scales have been fabricated[10-14] [15-17], and have been shown to exhibit similar structural characteristics as metallic QC.

Polymeric 2D quasicrystals have been made on the micron scale in photoresist polymers by multibeam and multiexposure interference lithotgraphy.[10-14] 3D quasicrystals with structural features from hundred-micron to millimeter length scales have been made by direct writing techniques[15-17]. Artificially patterned QC structures have attracted significant attention due to their promising applications as photonic and phononic crystals.[11, 13, 15-17] While studies of the photonic properties of the 2D and 3D quasicrystals have been reported recently[11, 16, 17] but the mechanical properties of IL fabricated 3D polymeric quasicrystals are not widely explored yet, unlike for QC metallic alloys

A challenge is to create 3D QC patterns on a 100nm scale. Using QC phase mask lithography[18, 19] (QCPML) we successfully fabricated 3D quasicrystals having eight-fold rotation axes on a submicron length scale in photoresist films and further characterized their mechanical behavior in the following sections.

5.2 Effect of Disorder on the Mechanical Properties of Composites

Fava and coworkers[20] studied the mechanical properties of a composite comprised of an elastomeric matrix with dispersed hard particles made of rigid core and soft shell. They demonstrated that the films with a random distribution of hard particles exhibit 25~30 % higher indenting stress than those with the particles in an

ordered distribution at a given particle volume fraction (30 %). The explanation for this behavior was that in face-centered cubic (fcc) ordered films, the deformation takes place by shear aligning the hard particles in zigzag patterns on the octahedral (111) planes, while the random distribution of the particles in disordered films blocks shear at low stress levels. Particle distribution in the matrix became an important factor for the resistance to deformation, energy absorption and the propagation of energy.

In the present investigation, the structural order of our polymer QC composites (polymer - air) is intermediate between crystalline (translationally periodic) and fully random structures. Furthermore, our QC samples consist of self-sustaining, polymer-air bicontinuous interpenetrating networks where each phase is continuously connected and intertwined with the other phase. This leads us to study 3D polymer-air quasicrystals as well as 3D polymer-air crystals[21] in terms of mechanical properties.

5.3 Fabrication of Octagonal Quasicrystals

The 3D octagonal QC SU8 films were fabricated by quasicrystalline phase mask lithography (QCPML) using 2D quasiperiodic poly(dimethylsiloxane) (PDMS) phase masks. To create the 2D QC phase masks, we molded transparent PDMS onto 2D octagonal QC (QC) silica templates following typical procedures.[22] The fabrication of the 2D octagonal QC silica templates via Lloyd's mirror IL is described in detail in

section 2.3.[18, 23] An SEM picture of a 2D QC PDMS mask is presented in Figure 5-1(a), where a 60% fill fraction mask was replicated from a 40% fill fraction 2D octagonal QC template with a relief height of 500nm. The multiple grating-patterns in positive photoresist (PR) layer were fabricated by 4 exposures of 800nm period 1D gratings with subsequent 45° rotations. In regions where the exposure dose exceeds a certain threshold, the positive PR becomes soluble, and the remaining PR pattern is then transferred by CHF_3 reactive ion etching (RIE) into the *20nm* SiO_2 interlayer.

Figure 5-1(b) is a digital photograph of the corresponding diffraction pattern obtained from a 355nm laser beam at normal incidence onto the PDMS phase mask shown in Figure 5-1(a). This diffraction pattern shows the octagonal, *8mm* point group symmetry, and qualitatively resembles the diffraction patterns of octagonal metallic alloy quasicrystals.[24]

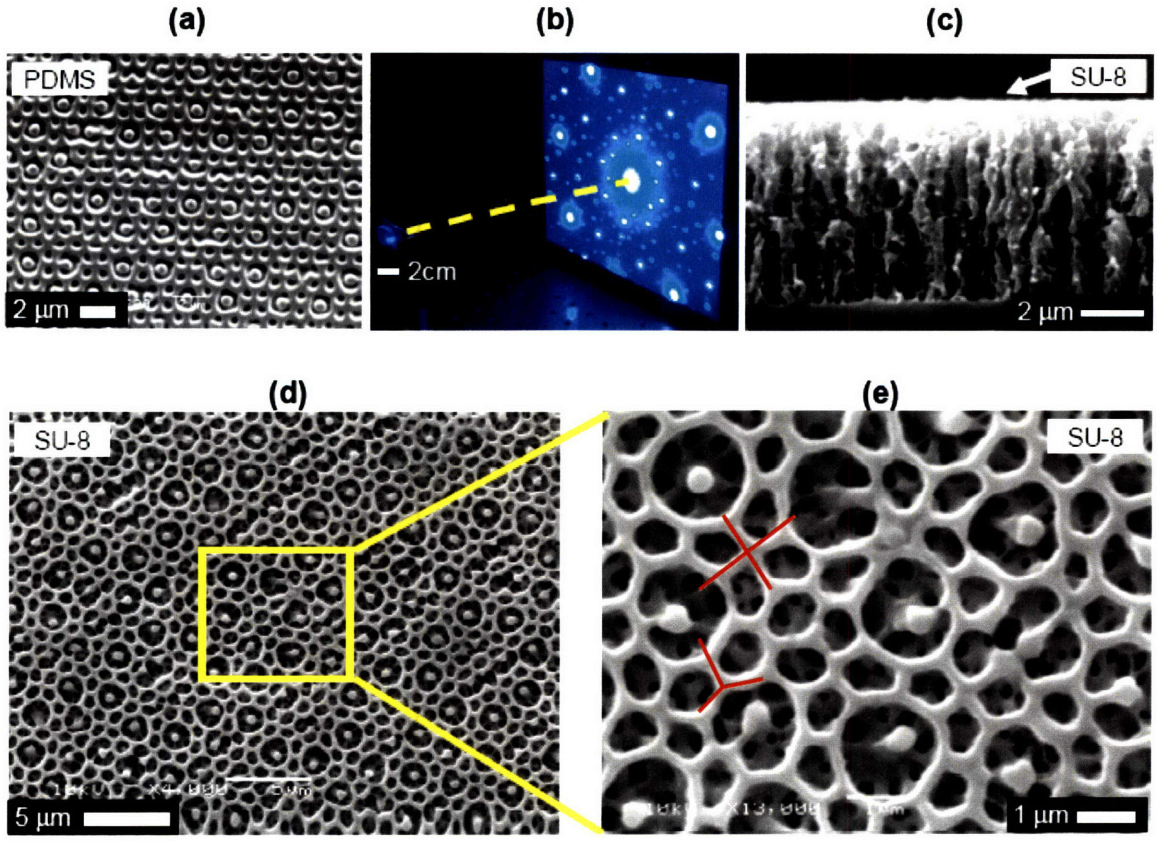

Figure 5-1. (a) SEM image of a 2D octagonal quasiperiodic PDMS phase mask, and (b) corresponding diffraction pattern produced by a laser beam (355nm) at normal incidence. (c) Cross-sectional SEM image of the 3D nanostructured quasiperiodic scaffold recorded in SU-8 by an expanded, flat-top 364nm laser beam passing through the phase mask in (a), and (d) corresponding plane-view SEM of its surface. Yellow box in (d) shows the diffraction pattern of the *~1x2cm* size 3D QC. (e) Magnified area from (d), showing sub-surface structured details. The red lines in the structure represent 3-connected or 4-connected at nodes in plane.

Using the PDMS phase mask, we fabricate 3D QC structures via QCPML. The glass substrate was coated with a 1.5 μm-thick buffer layer of hard-crosslinked SU8 material for the firm adhesion of the structured scaffold to the substrate. The subsequently coated SU8 films were exposed using a 355nm Nd:YAG laser with the dose of 0.18 J/cm^2 for creating QC patterns (shown in Fig. 5-1(c-e)). The following procedures were carried out as discussed in section 2.3.

Figures 5-1(c-e) show plan-view and side-view SEM images of a bicontinuous 3D QC structure with octagonal symmetry produced via QCPML. The sample morphology was analyzed by SEM (JEOL 6060) after cross sectional polishing (JEOL). These structures were recorded in a 6 μm thick layer of SU8 photoresist by a flat-top 364nm laser beam passing through the 2D octagonal QC PDMS phase mask shown in Figure 5-1(a) placed in conformal contact with the SU8 layer. The magnified image in Figure 5-1(e) details the sub-surface structure of the fabricated 3D QC SU8 scaffold.

In order to investigate the 3D nature of the fabricated QC, confocal microscopy was conducted on the sample shown in Figure 5-1(d). The porous SU8 scaffold was filled with rhodamine 6G glycerol solution, and the confocal images captured in fluorescent mode using a 488nm Ar-ion laser. Images at various depths from the surface ($0 > z > -5.0$ μm) are shown in Figure 5-2(b). Note that the brighter regions containing the dye correspond to air channels in the original SU8 structure. This series of z-depth dependent images demonstrates that the octagonal quasiperiodicity is preserved throughout the entire thickness of the SU8 film. For example, note the approximate structural inversion at $z = -0.5$ μm and -4.0 μm, where the solid SU8 regions (darker pixels) reverse into void space (brighter pixels), and vice-versa.

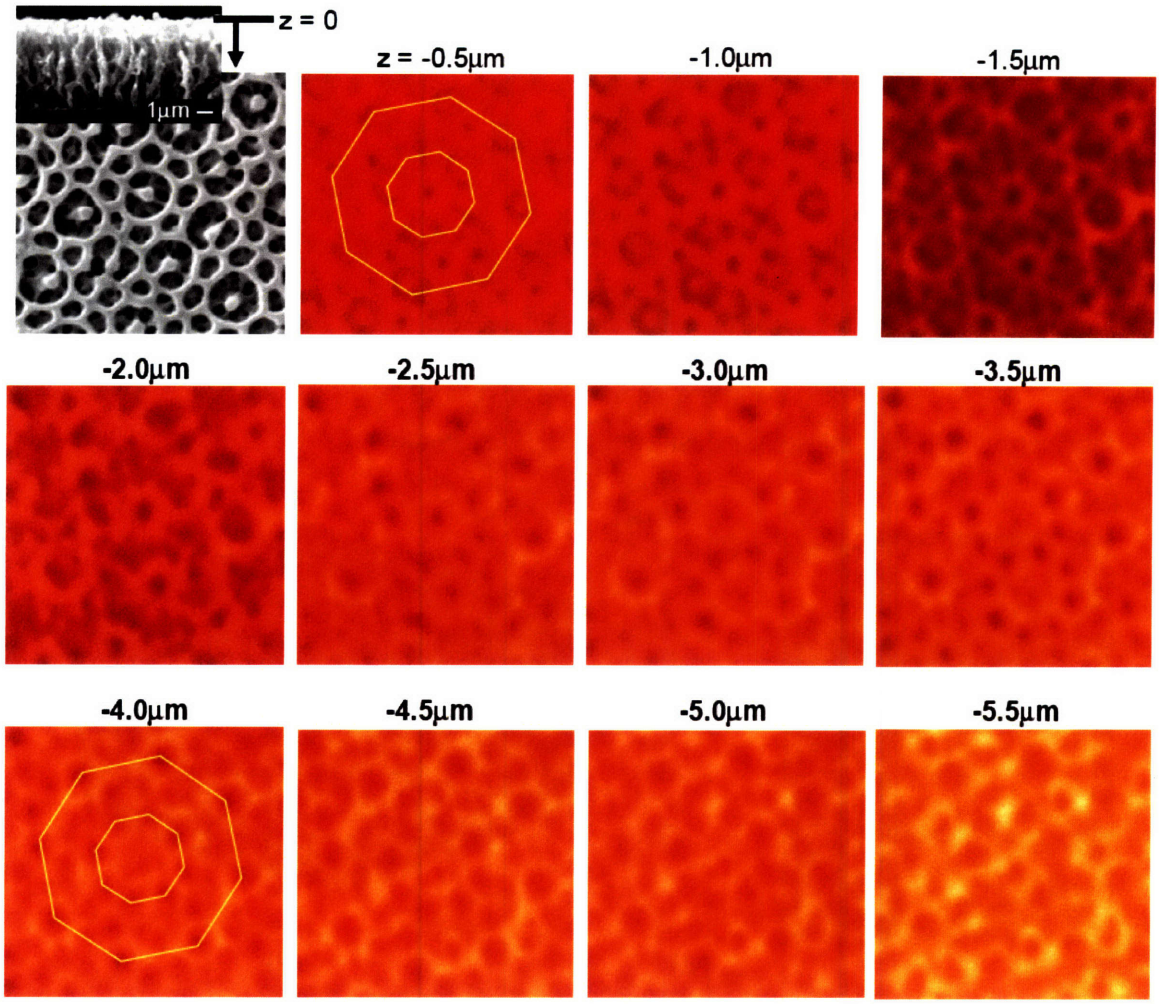

Figure 5-2. Confocal microscopy images of the 3D quasiperiodic SU8 scaffold shown in Figure 5-1(d) taken in fluorescent mode using a 488nm Ar-ion laser. Brighter regions correspond to air channels in the original SU-8 structure. The octagonal quasicrystalline symmetry is preserved throughout the thickness of the structured film. The plan-view SEM picture of the SU8 scaffold surface is given as a reference for the $z = 0$ location.

In collaboration with CheongYang Koh (DMSE, MIT), we calculated the 3D octagonal QC structure using the octagonal phase mask via a generalized form of the Fourier Modal Method,[25] typically used in computing diffraction efficiencies in 2D gratings. The calculated model using the conditions of phase mask is shown in Figure 5-3(b) agrees very well with the fabricated SU8 QC structure from the phase mask. For example, in the thickness range from z = -0.5 μm and z = -4.5 μm in Figure 5-3, the blue

top layer and the gold bottom layer in the calculation are shifted sideways as observed in confocal images in Figure 5-2. Further use of this method of structure prediction calculation based on the Fourier Modal Method[25] will be very valuable to guide the fabrication of phase masks for desired target 3D structures.

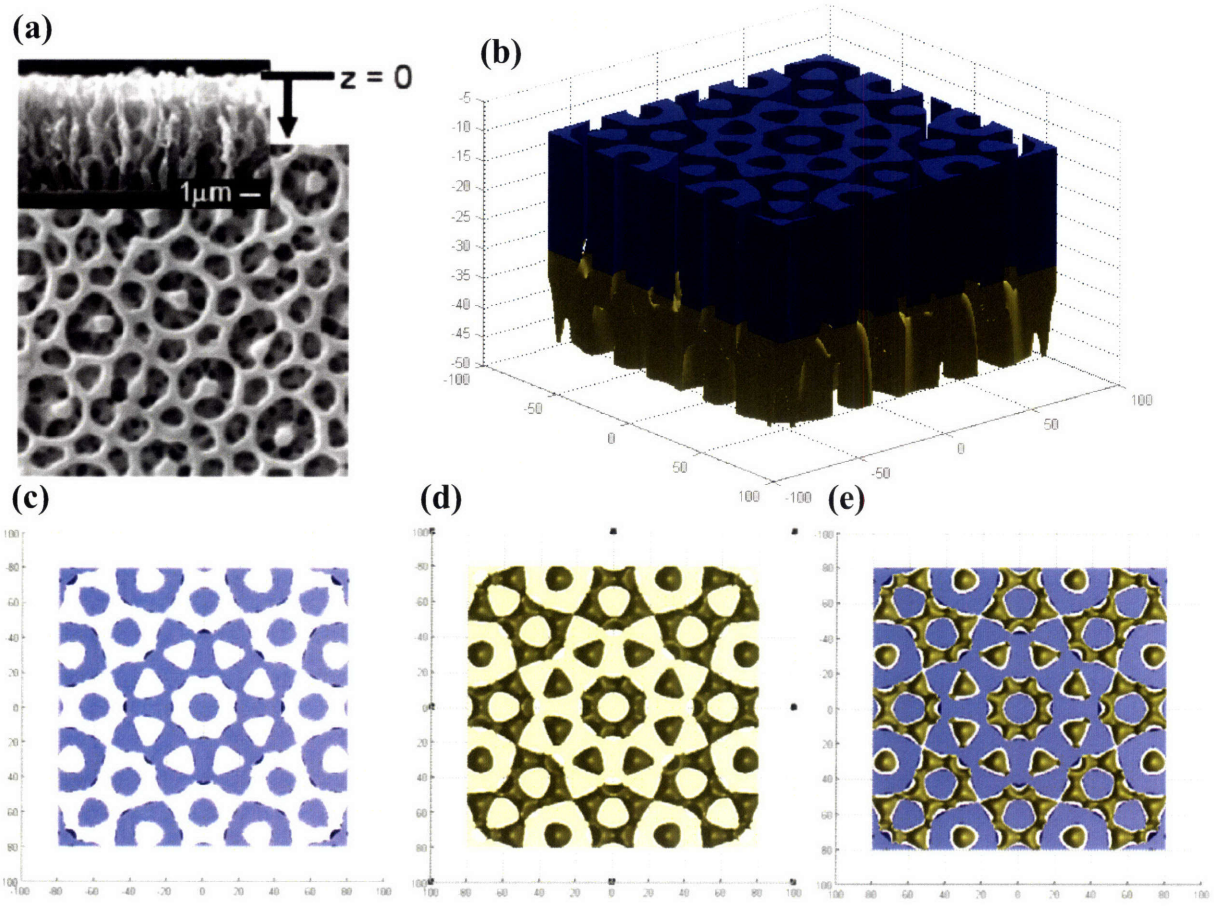

Figure 5-3. The computation of diffraction efficiencies in a set of 2D gratings for the octagonal QC structure from the 2D octagonal phase mask which has 300nm periodicity, 60% volume faction with 364 nm exposure wavelength and the refractive index of 1.62 from SU8. (a) SEM micrograph of QC structure. (b) The calculated model corresponds very well with the resultant structure in the SEM. (c) The top half of the structure in plane at -0.5 μm. (d) The bottom half of the structure which is staggered to the top layer at -4.0 μm. (e) The top layer (blue) and the bottom layer (yellow) shown at the same time of z range from -0.5 to -4 μm. Courtesy of CheongYang Koh. (DMSE, MIT).

5.4 Brillouin Light Scattering and Microtensile Testing on 3D Octagonal Quasicrystals

It is known that the elastic moduli (E) tensor is expected to be isotropic in the plane normal to the rotation axis when the structure has more than one axis of three-fold rotational symmetry in 2D and six axes of 5-fold symmetry in 3D by crystallography.[26] It is also found that the E tensor is isotropic in linear elastic properties for octagonal and dodecagonal axial quasicrystals according to Hermann's theorem for analysis of elasticity in quasicrystals.[27] In order to experimentally investigate the isotropy of elastic modulus in our SU8 axial QC films, we used Brillouin Light Scattering (BLS) to measure the velocities of sound along different directions in the plane perpendicular to the axial direction. Specifically, an azimuthal angle (φ) range of 0°, 5°, 10°, 15°, 20° and 22.5° was investigated, where 0° was chosen to correspond to a mirror axis, as shown in Figure 5-4(a). Figure 5-4(b) presents a representative BLS spectrum of the SU8 QC film obtained at a scattering angle of 24° showing phonon peaks arising from the SU8 QC structure and from the glass substrate. These measurements from 0 to 22.5 degrees provide sufficient information for all directions in the structure due to the 8-fold rotational symmetry.

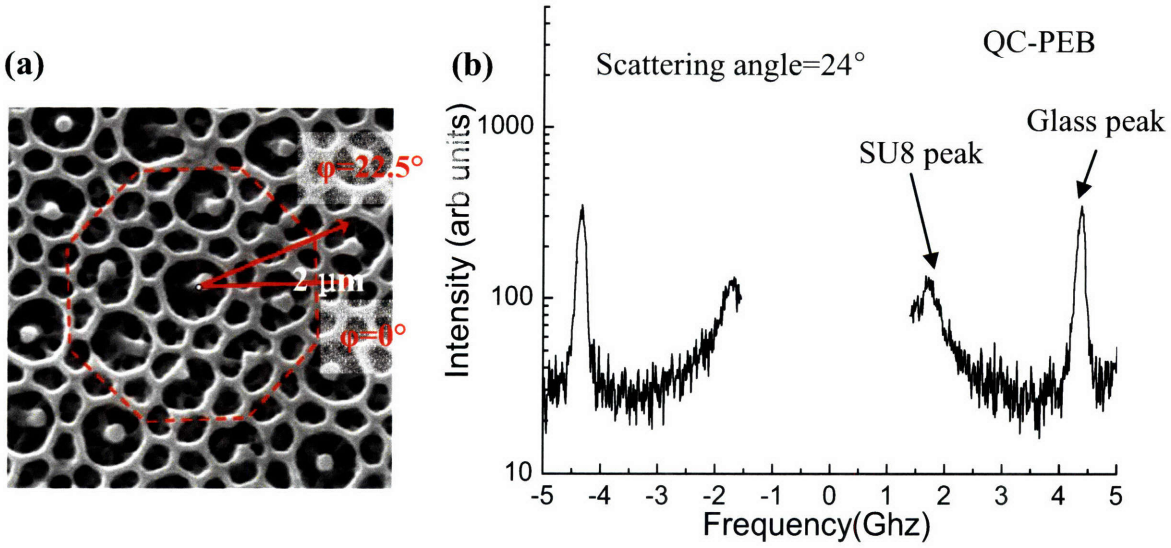

Figure 5-4. (a) BLS measurements were conducted with six different orientations of an azimuthal angle (φ) in plane from 0 (on a mirror axis) to 22.5° counter-clockwise at a fixed wave vector, k. (b) BLS spectrum taken at 24 ° for the k scattering angle (k = 4.9 μm^{-1}) and 0° orientation shows peaks from SU8 QC structure (at f =1.79 GHz) and from glass (at f = 4.52 GHz).

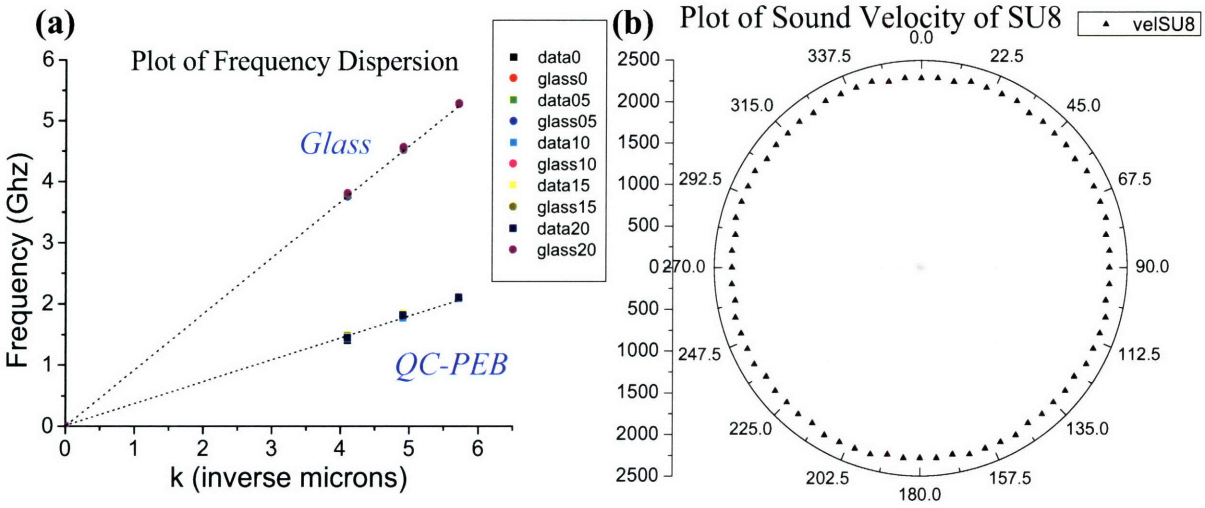

Figure 5-5. (a) Plot of frequency dispersion measured in six different orientations in plane (0°, 5°, 10°, 15°, 20° and 22.5°) at three different scattering angles (20°, 24° and 28°), which provide sufficient information for all directions associated with 8-fold rotational symmetry. The slopes represent the sound velocity in glass (upper line) and in SU8 QC PEB film (lower line): the average sound velocity in SU8 QC PEB film is 2300 m/s. (b) Azimuthal plot of sound velocity of SU8 QC PEB film. With the proportional relationship between the sound velocity and the modulus, this plot shows the isotropy of the in-plane modulus in the SU8 QC structure. Using the measurements from 6 directions, the other values are replicated by applying rotational symmetry.

In order to minimize undesired light scattering from refractive index variations in the sample, in our BLS measurements the SU8 QC PEB film was infiltrated with an index matching phenylmethyl silicone fluid with refractive index, n=1.62 (at 532 nm), density ρ=1.097 g/cm^3, and longitudinal speed of sound c_L=2030 m/s.[28] The refractive index of SU8 epoxy is n_{epoxy}=1.62 (at 532 nm), while its density and sound velocities are ρ_{epoxy}=1.19 g/cm^3, c_{L_epoxy}=2860 m/s and c_{t_epoxy}=1800 m/s, respectively. By experimentally varying the scattering angle, the frequency dispersion shown in Figure 5-5(a) was obtained for a multitude of azimuthal angles, and from the slope of the frequency dispersion we calculated an average longitudinal speed of sound c_L of 2300 m/s for the SU8 QC structure. The data for the speed of sound in a range of in-plane directions (azimuthal angles from 0 to 22.5°). were plotted in a radial graph (Fig. 5-5(b)) showing *the isotropy of the in-plane modulus* of SU8 QC structure from the relationship between the speed of sound and the modulus $c_L = \sqrt{\frac{K}{\rho}}$. From this relationship, the corresponding effective bulk modulus (K_{eff}) of the SU8-fluid structure from the calculated speed of sound (2300 m/s) is 6.07 GPa, assuming an effective density of SU8-air structure of 1.148 x 10 g/cm^3 based on a 45% porosity ($\rho_{eff} = \rho_{SU8} \cdot f_{SU8} + \rho_{fluid} \cdot f_{fluid}$). Using the relationship between bulk modulus and

elastic modulus, $K = \frac{E}{3 \cdot (1 - 2\nu)}$, we can extract out the effective elastic modulus of the SU8-fluid QC structure. Using a Poisson's ratio of 0.22 for pure and bulk epoxy SU8[29], we estimated the effective Poisson's ratio of the SU8-fluid QC structure as 0.35 based on a simple volume averaging, $\nu_{eff} = \nu_{SU8} \cdot f_{SU8} + \nu_{fluid} \cdot f_{fluid}$. Thus, the resulting effective E of QC film is 5.60 GPa.

To analyze the large strain mechanical behavior of 3D octagonal QC SU8 films, we conducted microtensile testing of the freestanding SU8 films using an MTS nano-UTM instrument. Besides the SU8 QC bicontinuous samples of interest (produced via 2D QC phase mask lithography), we also tested uniformly crosslinked homogenenous SU8 films (produced by a flood exposure of spun coated SU8 films to a 365 nm mercury lamp with a dose of 0.6 J/cm^2)*. In order to facilitate mounting the samples for microtensile testing, both the QC structured and the uniform SU8 thin films were first released from their respective substrates. The unstructured SU8 films (5.5 μm thick) were peeled by a razor blade from glass substrates. The QC SU8 films (4 μm thick with a thin solid bottom SU8 buffer layer of 1.5 μm thickness) were fabricated on top of water-soluble (NaCl) substrates, and then soaked in water dissolving the substrates for

* Note: the crosslink density with exposure of the UV lamp will likely be different than with other laser wavelength and exposure doses.

floating off the SU8 films.

Uniaxial tensile testing was performed with the load direction in the plane of the film to measure the in-plane E in 3D octagonal QC SU8 samples. We note that the orientation of the QC films before the test is not important, given that the in-plane E of the film is isotropic at low strains as confirmed in BLS (however, the sample orientation is important after the film deforms plastically).

Figure 5-6 shows the experimentally determined engineering stress-strain curves for the unstructured SU8 films (Uniform, black curves) and for the 3D SU8 QC films with post-exposure bake (PEB) only (QC PEB, red curves) obtained at a strain rate of

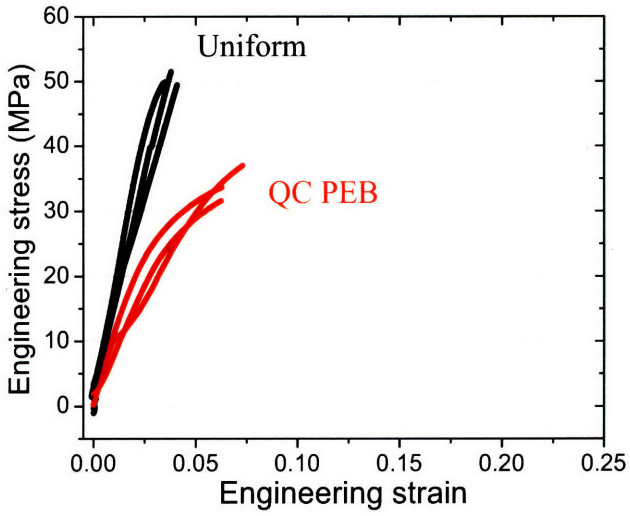

Figure 5-6. Stress-strain curves of freestanding polymer films from the micro-tensile testing. Black curves: Uniform SU8 5.5 μm-thick films. The three nearly linear curves show brittle fracture with elastic properties having average E = 1.72±0.27 GPa and toughness = 0.96±0.10 MPa. Red curves: SU8 octagonal QC films of polymer-air composite have average E = 0.85±0.13 GPa and toughness = 0.98±0.56 MPa.

$1x10^{-4}$/s. For the unstructured films, an average E of 1.72±0.27 GPa is obtained from the slope of the stress-strain curve, and a toughness (T) of 0.96±0.10 MPa from the area under the curve with the strain at fracture of ~ 0.04 (Fig. 5-6). This elastic modulus agrees very well with the value of 1.65 GPa we measured from dynamic mechanical analysis (DMA) using the Q800 DMA, TA instrument (shown in Fig. 5-7). From DMA we also estimated the glass transition temperature of unstructured SU8 films to be around 200 °C.

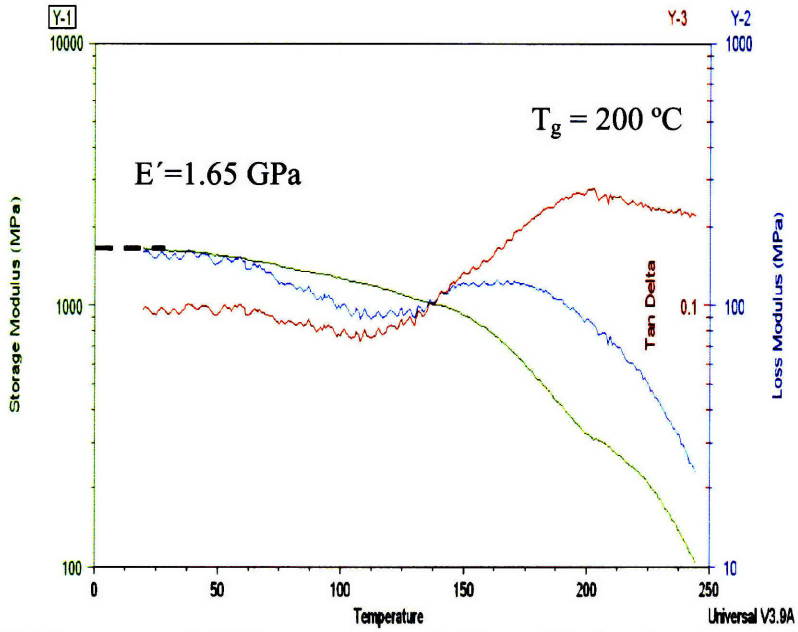

Figure 5-7. DMA curve of SU8 unstructured film with heating rate of 3 °C/min at frequency 1 Hz. The storage modulus is 1.65 GPa at room temperature (green curve) and the glass transition temperature is about 200 °C from the peak of tan delta (brown curve). Multiple DMA scans were conducted and values are similar with a narrow range.

From the data shown in Figure 5-6, the E of the QC polymer-air composite films is 0.85±0.13 GPa and a toughness is 0.98±0.56 MPa. Young's modulus decreases by a

factor of about half and the toughness stays at the same level due to an increased deformation of the QC film. The specific elastic modulus (elastic modulus / relative density (0.55)) of the QC structure is 1.54 GPa and the specific toughness is 1.78 MPa compared to the values of uniform films, 1.72 GPa and 0.96 MPa. For QC structured films, the specific elastic modulus is similar while the specific toughness is much higher than the uniform films. Thus the QC structured films are affirmed to be beneficial in terms of toughness and energy absorption per unit mass compared to the unstructured films. Furthermore, we observed high plastic deformation of struts on submicron scales in the SEM micrographs.

	Unstructured	QC PEB
The specific elastic modulus (GPa)	1.72±0.27	1.54±0.24
The specific Toughness (MPa)	0.96±0.10	1.78±1.01

Table 5-1. The specific elastic modulus (GPa) and the specific toughness (MPa) with consideration of relative density from the stress-strain curves of SU8 unstructured (Unstructured) and QC films (QC PEB). The QC SU8 films, air-polymer composite, has similar E but much higher T compared to unstructured solid films. Thus, the QC polymer-air films are favorable for mechanical applications with light weight.

5.5 Hardbaking Effect

For the typical fabrication of structures from SU8 photoresist, a hardbaking step

is normally conducted between 150-200 °C for a few minutes to remove any remaining solvents and for further crosslinking the structure. As a consequence of hardbaking, a homogeneous, bulk epoxy film will experience an increase in the crosslink density and thus an increase of the T_g, which can lead to an increased E and a much smaller strain to fracture and thus smaller fracture toughness, compared to the sample of pre-hardbacking.[30]

In order to investigate the effect of hardbaking on the mechanical properties of our QC SU8 films with a structure on the submicron length scale, we prepared samples by taking some of the 3D QC films after developing and drying, and further exposing them to UV using a 365 nm mercury lamp for 3 minutes, followed by hardbaking at 180 °C for 10 minutes. This treatment should result in a uniform crosslink density over the entire film. The hardbaked (HB) QC films were then mechanically characterized via BLS measurements and microtensile testing.

Figure 5-8 shows two BLS spectra together, one from an SU8 QC film with PEB only (graph in red) and the other from an SU8 QC film that underwent both PEB and HB (in blue). It is observed that hardbaking leads to an increase of the frequency of the phonon peaks for epoxy-fluid composites, which represents an increase in the SU8 elastic modulus. From BLS measurements at three scattering angles and six different

orientations, a 2950m/s longitudinal speed of sound, c_L, was obtained for SU8 QC PEB+HB structures, see Figure 5-9(a). The set of sound velocities of QC PEB+HB film (blue circles) and that of QC PEB films (black squares) was plotted together in the radial graph in Figure 5-9(b) suggesting an isotropic velocity within 5% variation. The effective bulk modulus (K) of SU8 QC HB structure is calculated as 10.0 GPa from the averaged sound velocity, and using the same effective density of epoxy-fluid composite as previously, the effective elastic modulus of QC film with hardbaking is found to be 9.24 GPa. These measurements confirm that hardbaking leads to an increased stiffness of the structured film.

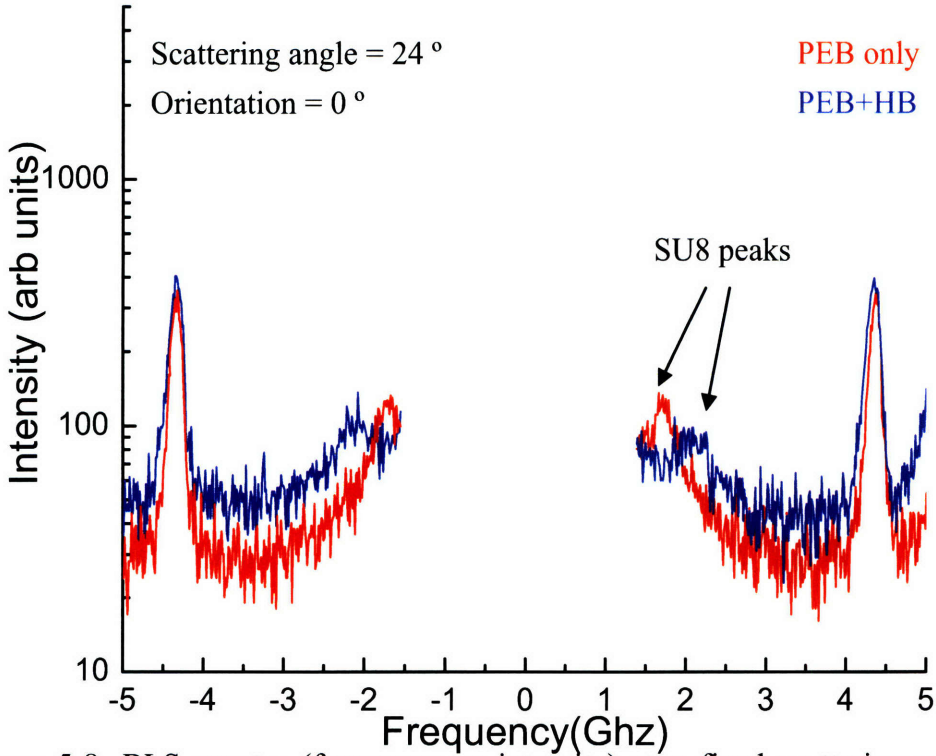

Figure 5-8. BLS spectra (frequency vs intensity) at a fixed scattering angle and an orientation show phonon peaks from SU8 QC structures shift from 1.79 GHz (PEB only, red) to 2.18 GHz (PEB+HB, blue). This shows the increase in the elastic modulus by hardbaking SU8 QC film.

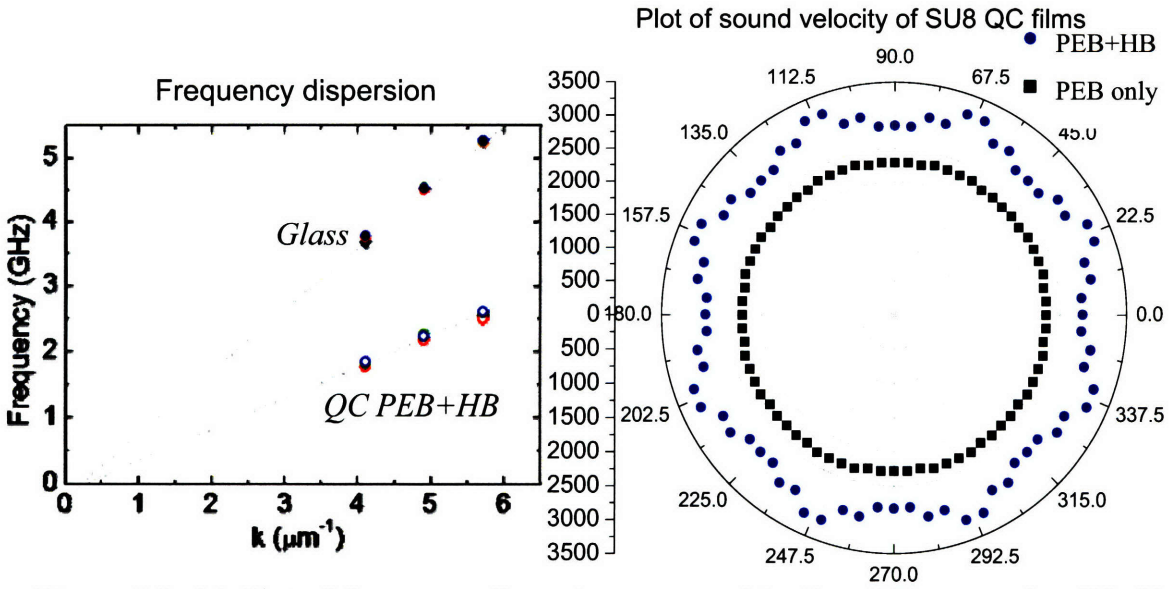

Figure 5-9. (a) Plot of frequency dispersion measured in five different angles (0°, 5°, 10°, 15° and 20°), which provide sufficient information for all directions associated with 8-fold rotational symmetry. The slopes represent the sound velocity in glass (upper) and in SU8 QC hardbaked film (lower): the average sound velocity in SU8 QC HB film is 2950 m/s. (b) Plot of sound velocity of SU8 QC PEB film (black) and SU8 QC PEB+HB film (blue). The average velocity of SU8 QC PEB film is 2300 m/s and the velocity of SU8 QC PEB+HB film is 2950 m/s. The associated bulk moduli for QC film without hardbaking and with hardbaking are 6.07 GPa and 10.0 GPa, respectively.

Further, uniaxial microtensile testing was then conducted on the 3D octagonal QC PEB+HB films. The resulting data is shown in Figure 5-10 corresponding to the engineering stress-strain curves for the unstructured SU8 films (Uniform, black curves), for 3D QC SU8 films with post-exposure bake only (QC PEB, red curves) and for 3D QC SU8 films with PEB and HB (QC PEB+HB, blue curves), all tested at a strain rate of $1x10^{-4}$/s.

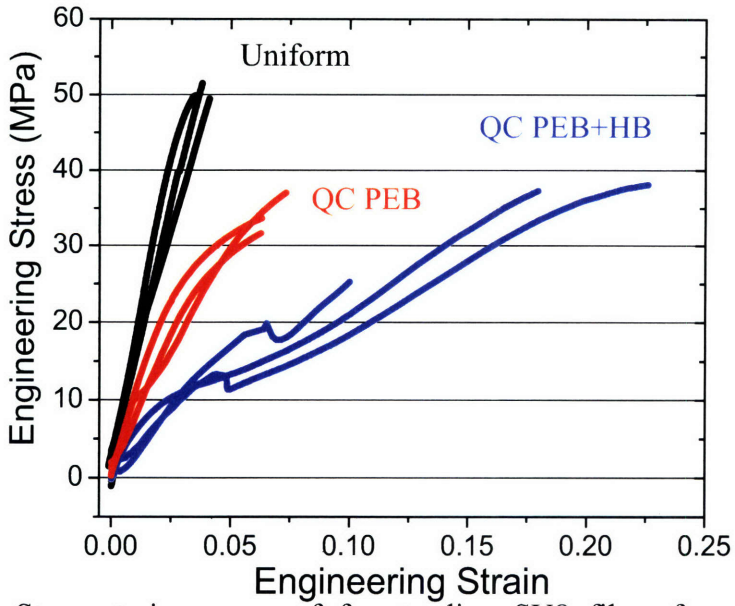

Figure 5-10. Stress-strain curves of freestanding SU8 films from the microtensile testing. Black curves represent the mechanical behavior of SU8 unstructured films. SU8 octagonal QC PEB films in red curves have E = 0.85±0.13 GPa and toughness = 0.98±0.56 MPa. SU8 octagonal QC PEB+HB films have E = 0.41±0.11 GPa and toughness = 2.92±1.52 MPa.

The results from microtensile testing on QC PEB+HB films show the decrease in the elastic modulus by a factor of two from QC PEB films. We speculate that baking at high temperature and cooling in the air might cause large thermal stress due to the difference in thermal-expansion coefficients between the SU8 film (α_{SU8_xy}=100 ppm/°C for and α_{SU8_yz} = 250 ppm/°C)[31] and the NaCl substrate (α_{NaCl} = 40 ppm/°C). This thermal stress induces the initiation of cracks either in the thin SU8 buffer layer or in the SU8 QC film. Another possibility is for the residual stress to lead to bending or buckling relatively thin struts so that the elastic modulus of the whole film might decrease for initial small strain under an applied tensile force in the testing. On the other hand, since

BLS spectroscopy measures the averaged overall sound velocity in the QC structured film, small regions of defects, cracks or deformation should not affect the BLS data. This length scale dependence explains why hardbaking seems to lead to opposite elastic modulus variations in SU8 QC films from BLS measurements vs. microtensile measurements.

5.6 Morphological Characterization after Fracture

In order to understand the higher toughness of the QC structure on the submicron scale compared to the unstructured SU8 films, we characterized the deformation of the QC films (PEB and PEB+HB) via SEM for plan-view in Figure 5-11 and side-view in Figure 5-12 of the unstructured and QC films after fracture.

The plan-view images of the fracture surfaces in Figure 5-11 show unusual crack propagation. As shown in Figure 5-11(a) and 5-11(b), crack propagation tended to be perpendicular to the loading direction through the fracture, path does not follow a straight line as observed in crystalline polymer/air networks[32] due to the absence of translational order in QC samples. We also observed in Figure 5-11(c) that one propagating crack from the fracture surface stopped inside the structure, and near this crack end a new crack formed and propagated. We speculate that a part of the

deformation energy is dissipated by crack propagation, and that the remaining energy is used for creating and propagating a new crack. Thus, as a result, more energy is absorbed in the 3D QC SU8 film than in the case of an unstructured film.

As expected, the unstructured SU8 films fail by brittle fracture, as shown in the side-view SEM of Figure 5-12(a) and 12(b). By comparison, the 3D nanostructured QC SU8 films composed of ~100nm-diameter struts exhibit a significant degree of plastic deformation (e.g. see Figure 5-12(e)). Stretched struts B in the deformed regions demonstrate the elongations of about 330 % in Figure 5-12(e) compared to undeformed struts A. The plastic deformation of the struts of the 3D SU8 QC films should allow more energy absorption than in the case of a brittle fracture in the unstructured SU8 films. However, the total global macroscopic strain at fracture remains only 8~10 % for our QC samples unlike the much higher observed local microscopic deformation. This could be a consequence of the small diameter of struts. We measured the diameters of the undeformed struts in a range of 100-400nm, and after loading under the tensile stress, these struts become stretched, thinned and finally disconnected, which inhibits further deformation.

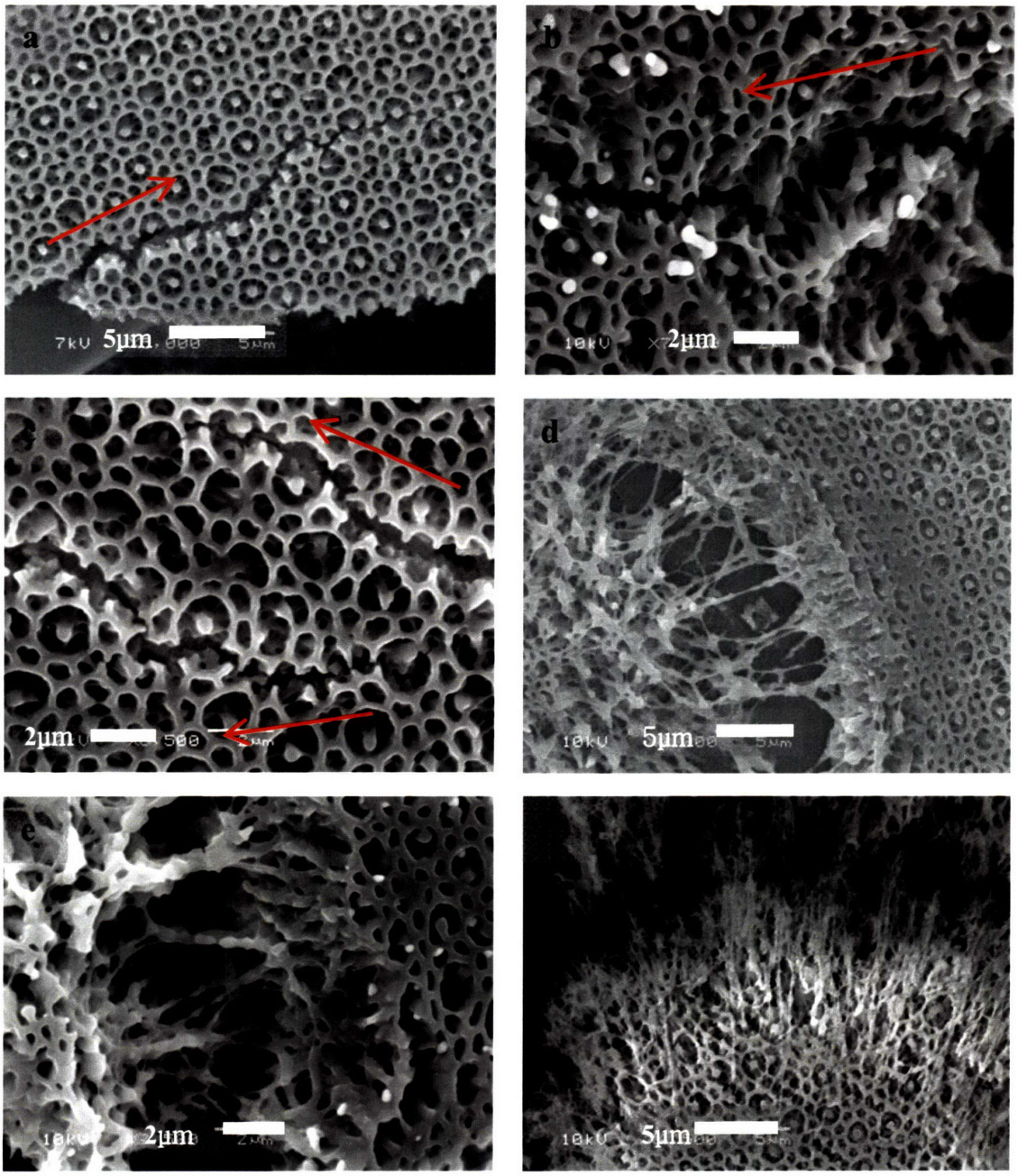

Figure 5-11. SEM plan-view micrographs of fracture surfaces in (a-e) SU8 QC PEB+HB films deformed by microtensile testing and (f) QC PEB only deformed by peel test. Red arrows show the direction of crack propagation. (a-b) Crack propagation from the fracture surface with the absence of translational symmetry, (c) Crack stoppage (upper) with the propagation direction by red arrows from the fracture surface and initiation of another crack (down) near the stopped crack. (d-f) Substantial plastic deformation of thin struts in the structure: (d) and (e) deformed by tensile testing and (f) deformed by complicated force from sticky tape peeling.

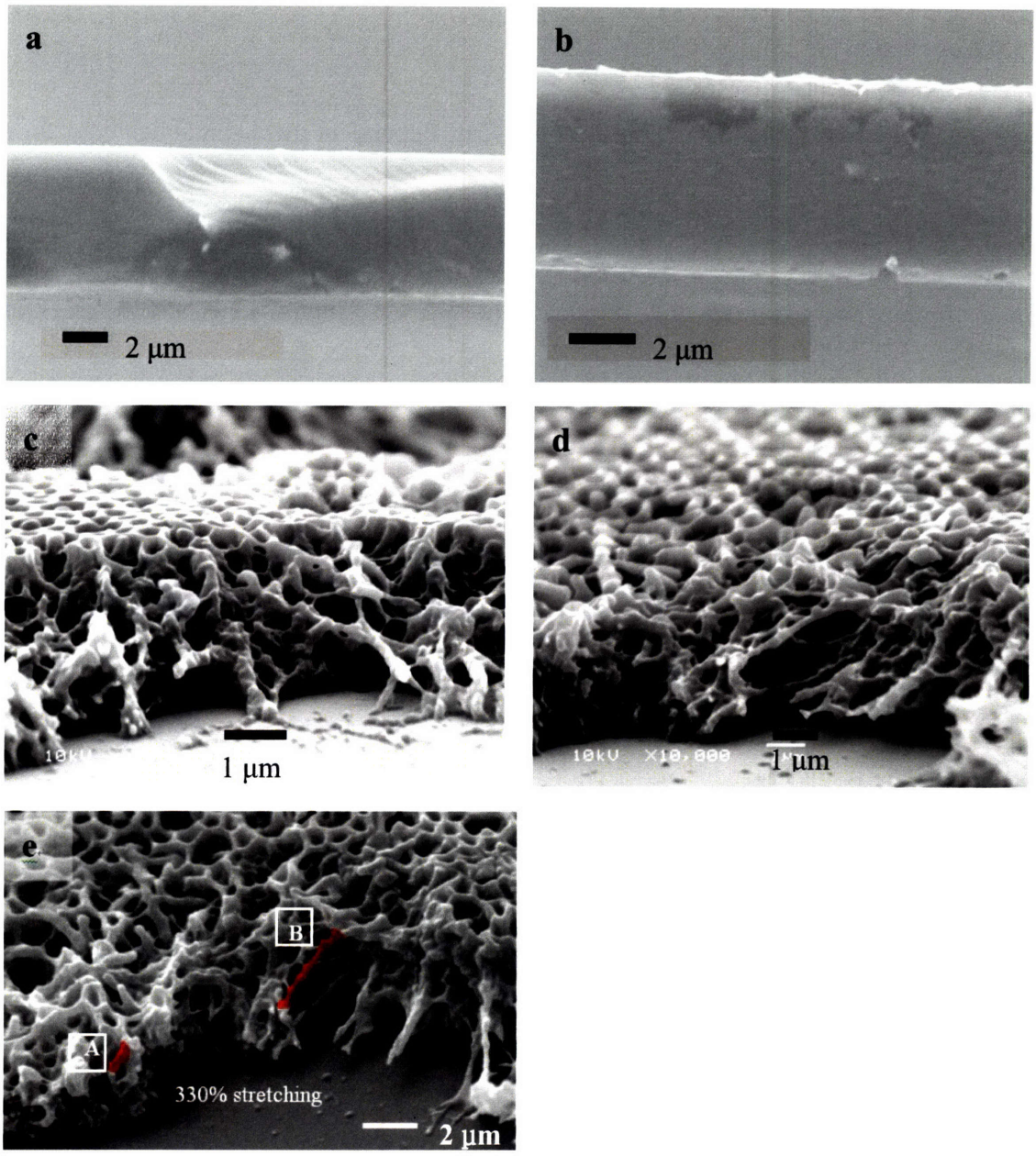

Figure 5-12. SEM micrographs of the side-view of fracture surfaces in SU8 thin films by tensile testing. (a-b) Fracture surfaces of unstructured SU8 films. The surfaces show brittle fracture with no significant plastic deformation. (c-e) Fracture surfaces of SU8 QC PEB+HB films exhibiting elongated struts comprising the pattern. Comparing struts A and B from (e), the elongated strut B is longer than stretched strut A by 330 %. This quantitative extension ratio represents the large deformation takes place under the deformation in microscopic ranges. The delamination between the structured film and thin solid buffer layer is observed in (d-e).

5.7 Conclusion

In chapter 4, we discovered a length scale dependent mechanical behavior for the SU8 epoxy polymer.[21] Inspired by the novel mechanical behavior of 3D periodic microframe, we explored the influence of 3D QC microframe structures. Crack propagation and very large microscopic plastic deformation (up to 300%) were evident in both QC PEB and QC PEB+HB films. BLS measurements on the 3D nanostructured SU8 QC network films confirmed the isotropy of the in-plane elastic modulus. BLS data demonstrated that hardbaking makes SU8 QC film stiffer in terms of elastic modulus from the longitudinal sound velocity, as expected. However in microtensile testing, the elastic modulus drops for the hardbaked 3D QC structures because there could be the initiation of cracks in the SU8 layers and the bending or buckling of the structural units due to the thermal stress.

5.8 References

1. Shechtman, D., Blech, I., Gratias, D. and Cahn, J. W., "Metallic Phase with Long-Range Orientational Order and No Translational Symmetry", *Phys. Rev. Lett.* **53**, 1951-1953 (1984).
2. Levine, D. and Steinhardt, P. J., "Quasicrystals - a New Class of Ordered Structures", *Phys. Rev. Lett.* **53**, 2477-2480 (1984).
3. Gorkhali, S. P., Qi, J. and Crawford, G. P., "Switchable quasi-crystal structures with five-, seven-, and ninefold symmetries", *J. Opt. Soc. Am. B-Opt. Phys.* **23**, 149-158 (2006).

4. Mancinelli, C., Jenks, C. J., Thiel, P. A. and Gellman, A. J., "Tribological properties of a B2-type Al-Pd-Mn quasicrystal approximant", *J. Mater. Res.* **18**, 1447-1456 (2003).
5. Park, J. Y., Ogletree, D. F., Salmeron, M., Ribeiro, R. A., Canfield, P. C., Jenks, C. J. and Thiel, P. A., "High frictional anisotropy of periodic and aperiodic directions on a quasicrystal surface", *Science* **309**, 1354-1356 (2005).
6. Reibold, M., Belger, A., Mukhopadhyay, N. K., Gille, P. and Paufler, P., "The impact of nanoindentation at room temperature upon the real structure of decagonal AlCoNi quasicrystals", *Phys. Status Solidi A-Appl. Mat.* **202**, 2267-2276 (2005).
7. Heggen, M., Feuerbacher, M., Schall, P., Klein, H., Fisher, I. R., Canfield, P. C. and Urban, K., "Plasticity of icosahedral Zn-Mg-Dy single quasicrystals", *Mater. Sci. Eng. A-Struct. Mater. Prop. Microstruct. Process.* **294**, 781-785 (2000).
8. Shield, J. E., Campbell, J. A. and Sordelet, D. J., "Mechanical properties of Al-Cu-Fe-based quasicrystalline coatings", *J. Mater. Sci. Lett.* **16**, 2019-2021 (1997).
9. Schreuer, J., Steurer, W., Lograsso, T. A. and Wu, D., "Elastic properties of icosahedral i-Cd84Yb16 and hexagonal h-Cd51Yb14", *Philos. Mag. Lett.* **84**, 643-653 (2004).
10. Gauthier, R. C. and Ivanov, A., "Production of quasi-crystal template patterns using a dual beam multiple exposure technique", *Opt. Express* **12**, 990-1003 (2004).
11. Notomi, M., Suzuki, H., Tamamura, T. and Edagawa, K., "Lasing action due to the two-dimensional quasiperiodicity of photonic quasicrystals with a Penrose lattice", *Phys. Rev. Lett.* **92** (2004).
12. Wang, X., Ng, C. Y., Tam, W. Y., Chan, C. T. and Sheng, P., "Large-area two-dimensional mesoscale quasi-crystals", *Adv. Mater.* **15**, 1526-+ (2003).
13. Zoorob, M. E., Charlton, M. D. B., Parker, G. J., Baumberg, J. J. and Netti, M. C., "Complete photonic bandgaps in 12-fold symmetric quasicrystals", *Nature* **404**, 740-743 (2000).
14. Wang, X., Xu, J., Lee, J. C. W., Pang, Y. K., Tam, W. Y., Chan, C. T. and Sheng, P., "Realization of optical periodic quasicrystals using holographic lithography", *Appl. Phys. Lett.* **88**, 051901 (2006).
15. Kaliteevski, M. A., Brand, S., Abram, R. A., Krauss, T. F., de la Rue, R. M. and Millar, P., "Two-dimensional Penrose-tiled photonic quasicrystals: diffraction of light and fractal density of modes", *J. Mod. Opt.* **47**, 1771-1778 (2000).
16. Man, W. N., Megens, M., Steinhardt, P. J. and Chaikin, P. M., "Experimental

measurement of the photonic properties of icosahedral quasicrystals", *Nature* **436**, 993-996 (2005).

17. Ledermann, A., Cademartiri, L., Hermatschweiler, M., Toninelli, C., Ozin, G. A., Wiersma, D. S., Wegener, M. and Von Freymann, G., "Three-dimensional silicon inverse photonic quasicrystals for infrared wavelengths", *Nat. Mater.* **5**, 942-945 (2006).
18. Bita, I., Choi, T., Walsh, M. E., Smith, H. I. and Thomas, E. L., "Large Area 3D nanostructures with Octagonal Quaasicrystalline Symmetry via Phase Mask Lithography", *Adv. Mater.* **19**, 1403-1407 (2007).
19. Jeon, S., Park, J. U., Cirelli, R., Yang, S., Heitzman, C. E., Braun, P. V., Kenis, P. J. A. and Rogers, J. A., "Fabricating complex three-dimensional nanostructures with high-resolution conformable phase masks", *Proc. Natl. Acad. Sci. U. S. A.* **101**, 12428-12433 (2004).
20. Fava, D., Fan, Y. S., Kumacheva, E., Winnik, M. A. and Shinozaki, D. M., "Order versus disorder: Effect of structure on the mechanical properties of polymer material", *Macromolecules* **39**, 1665-1669 (2006).
21. Jang, J.-H., Ullal, C. K., Choi, T., Lemieux, M. C., Tsukruk, V. V. and Thomas, E. L., "3D Polymer Microframes That Exploit Length-Scale Dependent Mechanical Behavior." *Adv. Mater.* **18**, 2123-2127 (2006).
22. Xia, Y. N. and Whitesides, G. M., "Soft lithography", *Annu. Rev. Mater. Sci.* **28**, 153-184 (1998).
23. Bita, I., *Breaking symmetries in ordered materials : spin polarized light transport in magnetized noncentrosymmetric 1D photonic crystals, and photonic gaps and fabrication of quasiperiodic structured materials from interference lithography.* Ph. D. thesis, Dept. of Materials Science and Engineering., Massachusetts Institute of Technology., (Cambridge, 2006).
24. Wang, N., Chen, H. and Kuo, K. H., "Two-Dimensional Quasi-Crystal with Eightfold Rotational Symmetry", *Phys. Rev. Lett.* **59**, 1010-1013 (1987).
25. Li, L. F., "New formulation of the Fourier modal method for crossed surface-relief gratings", *J. Opt. Soc. Am. A-Opt. Image Sci. Vis.* **14**, 2758-2767 (1997).
26. Christensen, R. M., "Sufficient Symmetry Conditions for Isotropy of the Elastic-Moduli Tensor", *J. Appl. Mech.-Trans. ASME* **54**, 772-777 (1987).
27. Gong, P., Hu, C. Z., Zhou, X., Miao, L. and Wang, X., "Nonlinear elasticities of octagonal and dodecagonal quasicrystals", *Phys. Lett. A* **356**, 168-173 (2006).
28. Gorishnyy, T., Ullal, C. K., Maldovan, M., Fytas, G. and Thomas, E. L., "Hypersonic phononic crystals", *Phys. Rev. Lett.* **94** (2005).

29. Luo, C., Schneider, T. W., White, R. C., Currie, J. and Paranjape, M., "A simple deflection-testing method to determine Poisson's ratio for MEMS applications", *J. Micromech. Microeng.* **13**, 129-133 (2003).
30. Van der Sanden, M. C. M. and Meijer, H. E. H., "Deformation and Toughness of Polymeric Systems: 3. Influence of Crosslink Density", *Polymer* **34**, 5063-5072 (1993).
31. Feng, R. and Farris, R. J., "Influence of processing conditions on the thermal and mechanical properties of SU8 negative photoresist coatings", *J. Micromech. Microeng.* **13**, 80-88 (2003).
32. Jang, J. H., Ullal, C. K., Choi, T. Y., Lemieux, M. C., Tsukruk, V. V. and Thomas, E. L., "3D polymer microframes that exploit length-scale-dependent mechanical behavior", *Adv. Mater.* **18**, 2123-2127 (2006).

Chapter 6. Summary and Future Work

In this last chapter, we will outline what are the main achievements presented in this thesis, and finish with a suggested list of potential future areas for investigation.

6.1 Summary and Conclusion

In this thesis, lightweight nano-network structures in polymer-air films have been fabricated and investigated for their structural and mechanical properties. The ability to rationally fabricate submicron scale periodic and quasiperiodic patterns and to evaluate their properties opens up a range of applications for microtrusses, photonic crystals, phononic crystals, microfluidics, biomimetic lenses and so on. The main focus of this thesis is on the mechanical behavior of a microtruss or a microframe depending on the connectivity of lattice-patterned and beam-connected structures on the submicron scale.

Fabrication via holographic interference lithography (IL) and quasicrystalline phase mask lithography (QCPML) were implemented for periodic and quasiperiodic polymer-air structures. A 2D hexagonal lattice of air-cylinders was made via three-beam interference lithography. A 3D periodic microframe, 3- $R\bar{3}m$ structure was produced via four-beam interference lithography. To create, for the first time, 3D

quasicrystalline nanostructures, we utilized a two dimensional quasiperiodic phase mask.

In order to quantitatively analyze the mechanical properties of these structures, three different mechanical characterization techniques were applied. Atomic force microscopy with its nanometer scale resolution was adopted to conduct force measurements for probing local elastic properties of the sample. As a second method, the microtensile tester enabled us to evaluate the effect of the submicron scale structure on the elastic and plastic properties of the polymer films as a whole. Brillouin light scattering was used to measure the sound velocity in the structured films and the elastic properties.

6.1.1 Small Strain Behavior: Modulus

Having nanometer scale displacements of AFM nanoindentation, we measured the out-of-plane elastic modulus of structured films as a small-strain property. We observed the spatial distribution of the elastic modulus templated by the light intensity distribution from three-beam interference in 2D hexagonal air-cylinder and SU8 polymers by AFM nanoindentation. The location-dependent elastic modulus can be employed to open possibilities for a purposeful design in photopatterned polymeric materials to guide where to deform through less stiff regions.

Brillouin light scattering apparatus allowed us to evalute the phonon properties in the structured films and the following mechanical properties. BLS spectroscopy of the sound velocity at high frequency in bicontinuous polymer-air films measured the bulk modulus of the 3D quasicrystalline (QC) films with post-exposure bake (PEB) only or with PEB + hardbaking (HB). The BLS measurements confirmed the isotropy of in-plane elastic modulus with the octagonal symmetry of the structures.

6.1.2 Large Strain Behavior: Plasticity

Applying large strain by tension, shear or compression, the large plastic deformation (up to 300 % strain) of 200nm-diameter struts comprising 3D periodic and quasiperiodic microframes was discovered. Unlike the brittle behavior in the bulk glassy polymer, the hundred-nanometer length scale of 3D microframes makes thin struts plastic under applied forces, which induces films to become tougher and more energy absorbing. However, even though some struts plastically deforms tremendously, the overall film exhibits brittle fracture of $\varepsilon_f \sim$ 8-10 %, which may result from the localization by the small dimension of the struts. Figure 6-1 demonstrates how the localization takes place in the 3D periodic microframe, described in chapter 4. A representative volume element of 3D periodic microframe deforms under tension (Fig. 6-1(a)) and under shear (Fig. 6-1(b)). Stretching the structure reduces the diameter of

thin struts and further thinning and breaking of the struts localize the deformation near a crack and result in overall brittle fracture.

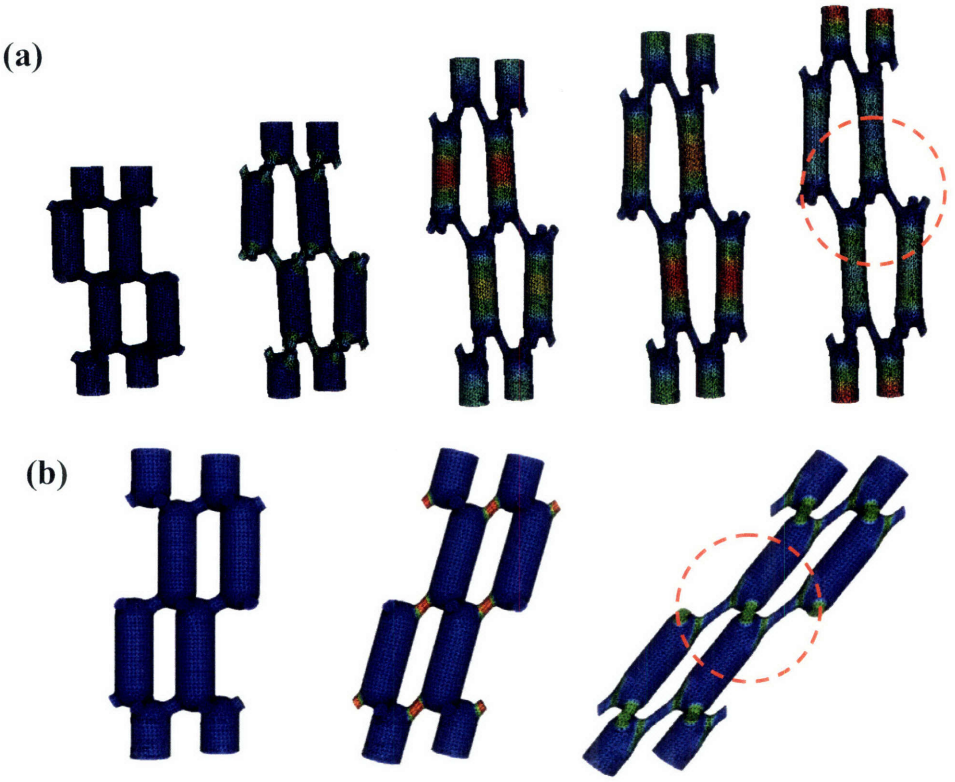

Figure 6-1. (a) The deformation under a tension of a Representative Volume Element (RVE) of the 3D periodic microframe by 3D micromechanical model. (b) The deformation under a shear of an RVE by 3D micromechanical model. Dashed circles in each figure show the size reduction of thin struts by elongation. The thinning and break of the struts might cause the localization of deformation and macroscopic brittle behavior. In strut deformation, red indicates materials deforming and blue indicates material not deforming. Modeling done by Dr. Lifeng Wang in Professor Mary C. Boyce group in mechanical engineering at MIT.

6.1.3 Large Strain Behavior: Crack Propagation

Another large strain behavior, the crack propagation was investigated in 3D periodic and quasiperiodic structures. The symmetry of periodically patterned films

determines the preferred direction of crack propagation and following brittle fracture. However, octagonal QC structured films do not exhibit preferred directions of crack propagation. We suggest that the absence of translational symmetry in the quasicrystalline films generates difficulty in crack propagation, which might give rise higher stress for deformation.

6.2 Future work and Suggestions

6.2.1 Other Materials

We have explored only SU8 polymer as a scaffold material for the nanostructures in this thesis with its thermal and mechanical stability and well known processing conditions from the MEMS community. It is of interest to investigate the same structures of different materials such as elastomeric materials or photoetchable glass. Poly(dimethyl siloxane) (PDMS) or fluoropolymers are good examples to start with as elastomers by infiltrating monomers into the SU8 template. Porous elastomers are interesting with their low glass transition temperatures for AFM nanoindentation and dynamic tensile testing. Continuing from chapter 4, additional types of microframe materials other than photoresists can be made by infiltration of these templates with, for example, a sol gel to create polymer-ceramic composites, or after a suitable etch, air-ceramic structures. Alternatively, photoetchable glasses may in the future be directly

patterned to create microframes. The advantages of photoetchable glasses are transparency, high Young's modulus (~ 80 GPa) and good thermal and electrical insulation for electronic and mechanical devices with high stiffness and strength rather than toughness.

6.2.2 Fabrication of a 3D microtruss

By utilizing IL and QCPML, we have created 2D and 3D microframes which behave bending-dominated deformation and have less than the required connectivity for stretch-dominated structures (6 struts per node in 2D and 12 struts per node in 3D). We have not yet succeeded to make microtrusses with a 12 connectivity in 3D. It is difficult to create a 3D microtruss by IL because of the required beam conditions to generate certain space groups from the level set technique.[1, 2] In order to utilize PML for a microtruss, we ought to be able to model what structures we can make from a 2D patterned mask. It is definitely needed to do modeling as a design guide for 2D phase masks to desired 3D microtrusses.

6.2.3 Fabrication of 2D Quasiperiodic Structures

We have fabricated 2D octagonal-patterned PDMS phase masks in chapter 5 to create 3D octagonal quasiperiodic structures. By using PDMS quasiperiodic phase mask, we are able to make a chrome mask and then fabricate 2D connected octagonal

quasiperiodic films via conventional photolithography using the chrome mask. The 2D quasiperiodic patterns in polymer films should be interesting to fabricate, analyze and compare mechanical, photonic and phononic results with other 2D periodic structures.

6.2.4 Phase Mask Lithography of Quasiperiodic Structures

For systematic fabrication and analysis of desirable 3D quasicrystals, the theoretical modeling such as prediction of the near field intensity pattern for a given quasiperiodic transparent mask is essential. This should help design a mask for a certain targeted structure for a special application. The modeling would need a lot of work since the pattern of the mask is not periodic.

When we fabricate the 2D octagonal QC structures in positive photoresist layer for producing PDMS phase masks, changing the exposure dose allows to readily vary the volume (fill) fraction of the resulting 2D quasiperiodic structures. Figure 6-2(a) and (b) show 2D quasiperiodic PDMS phase masks with different volume fractions of 60% and 70%, respectively. The small difference in volume fraction gives rise to the same symmetry but different structure in the resultant 3D QC structures as shown in Figure 6-2(c) and (d). It should be interesting to study theoretically and experimentally how the structure and fill fraction of 2D phase masks make an effect on the resultant 3D QC structures.

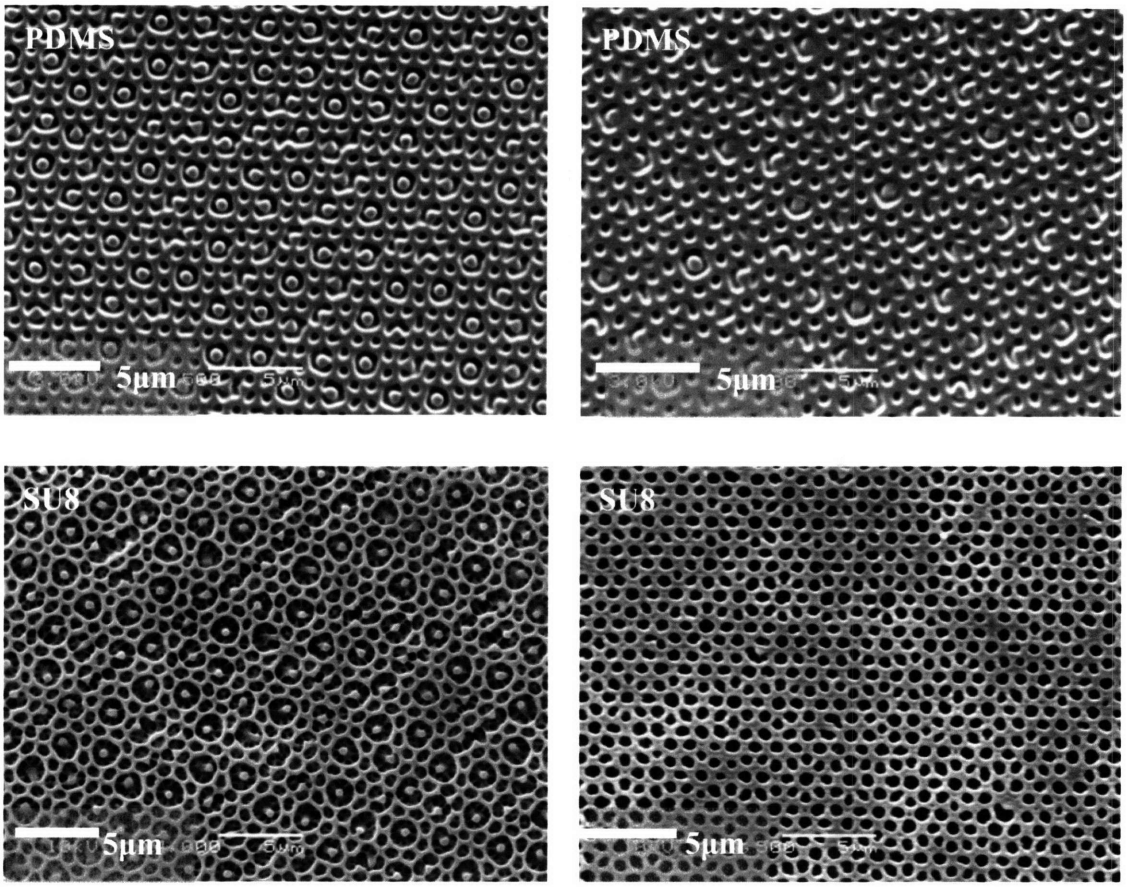

Figure 6-2. (a) 2D quasiperiodic PDMS phase mask with 60% volume fraction. (b) 2D quasiperiodic PDMS phase mask with 70% volume fraction. (c) 3D octagonal QC structure fabricated via quasicrystalline phase mask lithography (QCPML) using PDMS phase mask shown in (a). (d) 3D QC structure with a different type of octagonal symmetry fabricated via QCPML using a different PDMS phase mask shown in (b).

6.2.5 Phase Mask Lithography of Periodic Structures

In a preliminary effort to make another 3D microstructure via PML, we have fabricated a 2D square-patterned phase mask in PDMS with 800nm spacing and 350 nm height ($\Delta\varphi=0.89\pi$) by Lloyd's mirror interference lithography (Fig. 6-3(a-b)). The resulting structure from 2D square PML is body-centered tetragonal structure as shown in Figure 6-3(c-d). From examining Figure 6-3(c) and (d), the fabricated SU8 structure

and the simulated unit cell look similar. The optimization of the method with 2D square masks is not trivial experimentally. Moreover, the mechanical studies on this structure should be worth to investigate and the comparison with 3D quasicrystals would be very appealing for design issues for various mechanical applications. Its photonic band gap properties are also interesting to study.

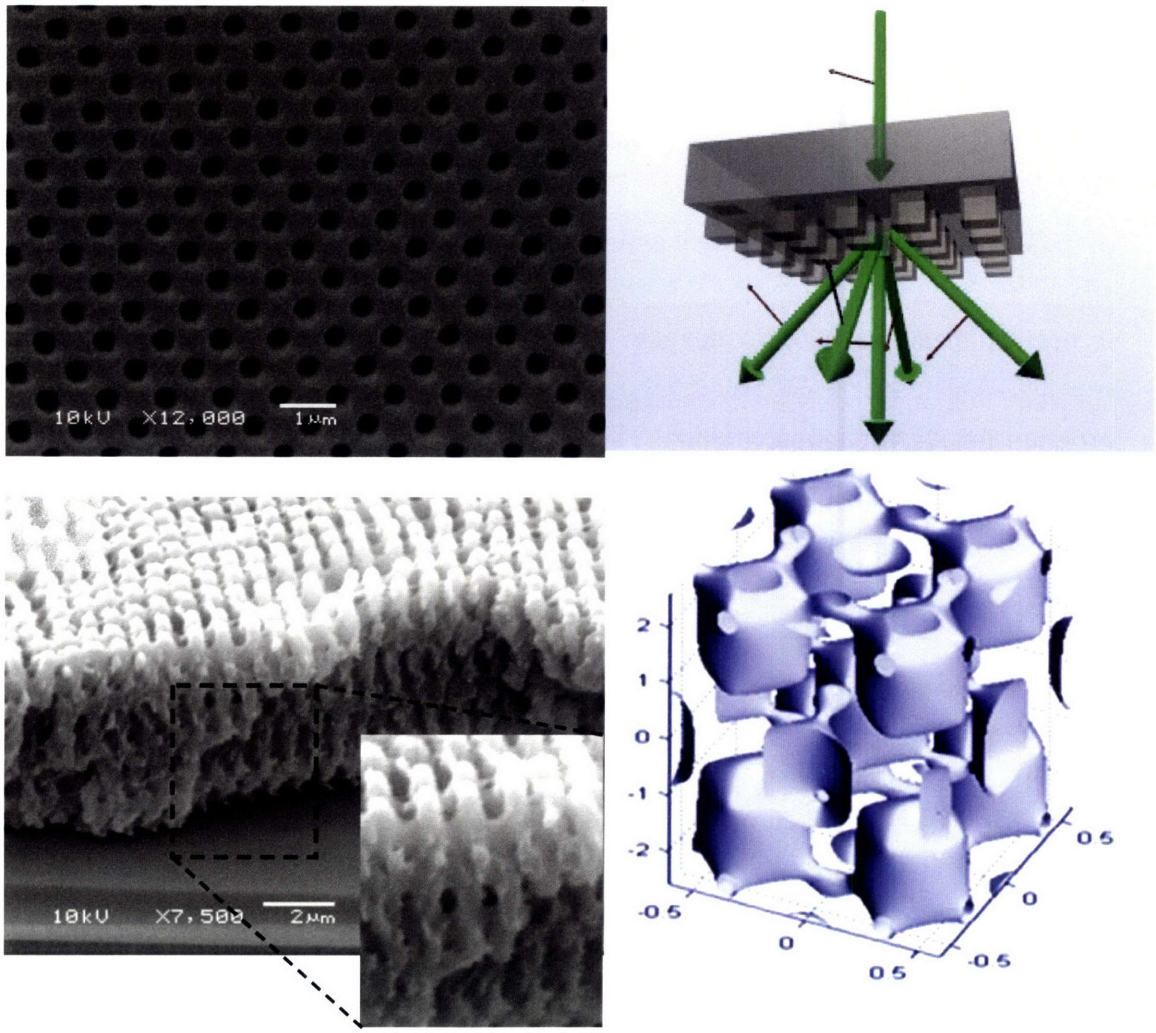

Figure 6-3. (a) 2D square air-cylinder patterned PDMS phase mask. Courtesy of Dr. Ji-Hyun Jang. (b) A schematic of a square phase mask with one-beam exposure and diffracted beams through the mask. Black arrows indicate polarizations of beams. (c) SEM micrograph of fabricated SU8 structure from square-patterned phase mask lithography. Inset: enlarged area for comparison to (d). (d) A unit cell of body-centered tetragonal structure from the simulation from the 2D square phase mask. Courtesy of Cheong Yang Koh (DMSE, MIT) for (b) and (d).

6.2.6 AFM Nanoindentation on 3D Microstructures

In chapter 4, we investigated the mechanical behavior of a 3D microframe using "the sticky tape". This clearly is not sufficient for quantitative evaluation of the

mechanical properties. We attempted AFM force measurements for elastic modulus on the 3D structure with different types of indenting tips. Because the Hertzian assumption of the usual analytic model, which assumes indentation of a flat and half-infinite surface, is not satisfied, we need to develop a new analytic (or FEM) model and software program for AFM nanoindentation. The further investigation should be able to involve the mechanical behavior of the 'entire structure' such as bending, buckling, and flexing.

6.3 References

1. Maldovan, M. and Thomas, E. L., "Photonic crystals: six connected dielectric networks with simple cubic symmetry". *J. Opt. Soc. Am. B-Opt. Phys.* **22**, 466-473 (2005).
2. Maldovan, M. and Thomas, E. L., "Diamond-structured photonic crystals". *Nat. Mater.* **3**, 593-600 (2004).

Chapter 7. Appendix

In this appendix, I will explain the details of theories and background which have not been discussed in the previous chapters.

7.1 Scaling Models for the Lattice-structured Materials from Gibson-Ashby Model in Section 2.1

7.1.1 Bending-dominated Structures[1, 2]

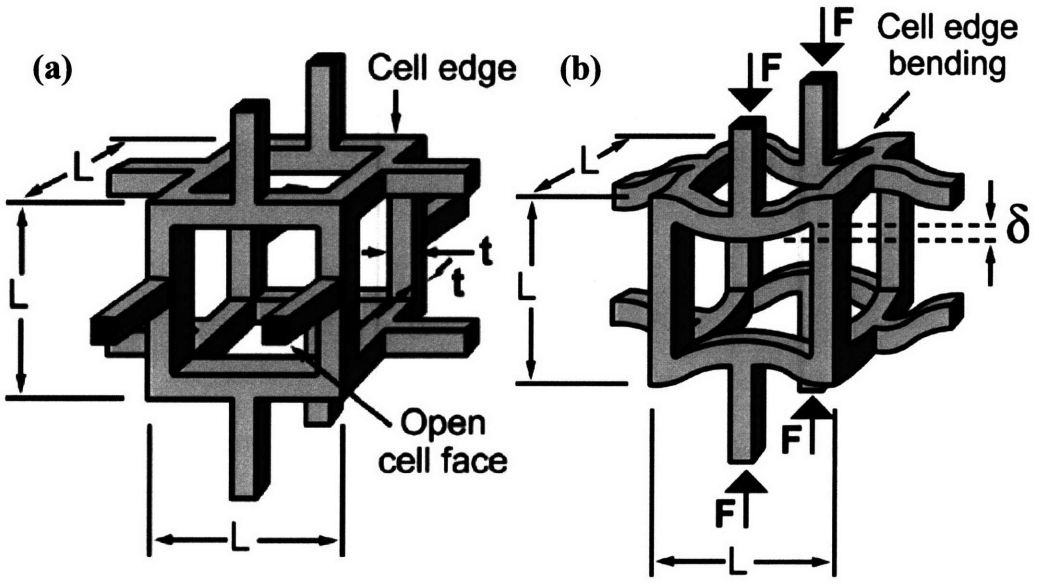

Figure 7-1. (a) A cubic model for the bending-dominated structure with open cells used for analyzing elastic modulus and fracture toughness of 3D microstructures with relative density. (b) When a low-connectivity structure is loaded with compressive force, the cell edges bend, giving a low modulus. For small strain linear elastic modulus deformed by cell-edge bending, calculating the relative elastic modulus is applied same for compression and tension .[2]

It is useful to develop simple algebraic expressions relating mechanical properties of periodic structures to those of the homogeneous bulk material. Thus we

seek to find scaling relations in terms of strut diameter and cell lattice parameter with quantities such as density, modulus and yield strength, etc.

An analytic scaling model for the bending-dominated structure with open cells in Figure 7-1 above, can be developed. The density of the open cell foam is ρ, The density of the solid material is ρ_s, t is the thickness of cell edge and L is the cell size. Since $\rho = \frac{mass}{volume}$, the density of the cell is described as $\rho = \frac{\rho_s \cdot t^2 L \cdot (n)}{L^3}$, where n is the number of struts per cell. Thus, the relative density ($\tilde{\rho}$) of the open cell compared to the solid becomes $\frac{\rho}{\rho_s} \propto \frac{t^2}{L^2}$. The second moment of area, I, is a property explaining a resistance to the bending or deflection and is is related to the dimensions t by $I \propto t^4$.

Young's modulus for the open cell is calculated from the linear-elastic deflection of a beam of length L loaded by a load F. Force F is proportional to the stress multiplied by the loading area, $F \propto \sigma L^2$ on the cell edges, where σ is stress. Deflection, δ, by this force is given from standard beam theory by $\delta \propto \frac{FL^3}{E_s I}$, where I is the second moment of area, of the cell edge of square cross-section, $t \times t$, $I = \frac{t^4}{12}$. Strain as a whole is defined as $\varepsilon = \frac{\Delta length}{original \cdot length} \propto \frac{2\delta}{L}$ since the deflections occur from the upper face and the lower face. The elastic modulus is stress/strain, $E = \frac{\sigma}{\varepsilon}$, stress is derived from the force and strain is given from the deflection and the equation

for elastic modulus appears as

$$E = \frac{\sigma}{\varepsilon_{cell}} = \frac{F/L^2}{2\cdot\delta/L} \propto \frac{(F/L^2)}{(2\cdot(FL^3/E_sI)/L)} = \frac{E_sI}{2L^4} = \frac{E_s(t^4/12)}{2L^4}.$$

Therefore, the relative elastic modulus is $\tilde{E} = \frac{E}{E_s} \propto \left(\frac{t}{L}\right)^4 \propto \left(\frac{\rho}{\rho_s}\right)^2$. (7-1)

For small strain linear elastic modulus deformed by cell-edge bending, this relationship is also applicable to the tensile forces for the bending-dominated structures.

Plastic collapse occurs when the moment by the force F exceeds the plastic moment of the cell beams, where the plastic moment is defined as making deformation from elastic to plastic. For analyzing the relationship between the yield strength and the relative density using fully plastic moment, M_f is firstly defined as $M_f = \sigma_{y,s} \cdot \frac{t^3}{4}$, where $\sigma_{y,s}$ is yield strength of the solid. As another relationship, the plastic moment of the cell foam is proportional to force and length of the cell edge: $M_p \propto FL \propto (\sigma_{pl} L^2) \cdot L$.

From the two plastic moment equations, $M_f = M_p \propto (\sigma_{pl} L^2) \cdot L \propto \sigma_{y,s} \cdot \frac{t^3}{4}$, we extract the scaling relationship of plastic and yield strength $\frac{\sigma_{pl}}{\sigma_{y,s}} \propto \frac{t^3}{L^3} \propto \left(\frac{\tilde{\rho}}{\rho_s}\right)^{\frac{3}{2}}$. (7-2)

Thus, the relative plastic strength of the open cell is proportional to the relative density to the scaling exponent, 3/2.

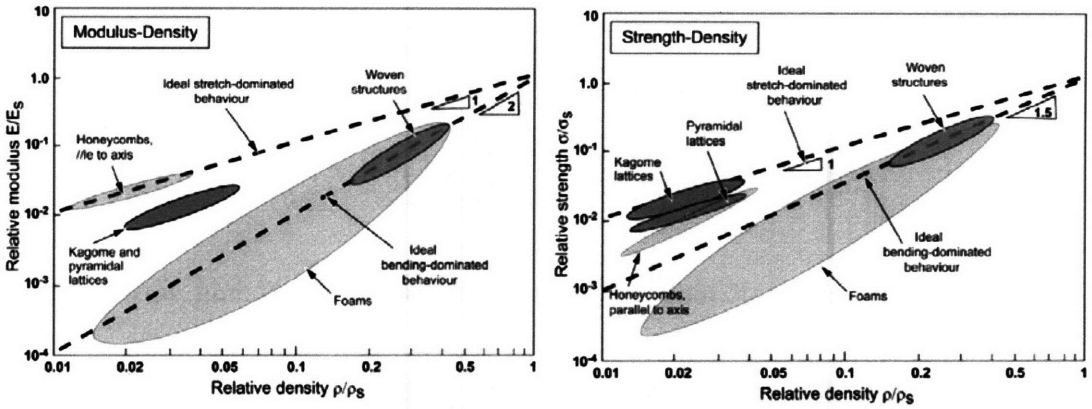

Figure 7-2. (a) Plot of relative modulus against relative density for cellular structure with different topologies on logarithmic scales. The bending dominated behavior has a slope of 2 and the stretch-dominated a slope of 1. (b) Plot of relative initial collapse strength against relative density for cellular structure with different topologies on logarithmic scales. The bending dominated behavior has a slope of 1.5 and the stretch-dominated a slope of 1.

7.1.2 Stretch-dominated Structures

Considering the tensile loading of the stretch-dominated structure shown in Figure 7-3, the structure first responds by elastic stretching of the struts since it does not bend. Due to the cubic symmetry of the structure, on average, one-third of its struts carry tension when the structure is loaded in simple tension in one direction, regardless of the loading direction, $\frac{\tilde{E}}{E_s} = \frac{1}{3}\frac{\tilde{\rho}}{\rho_s}$. (7-3)

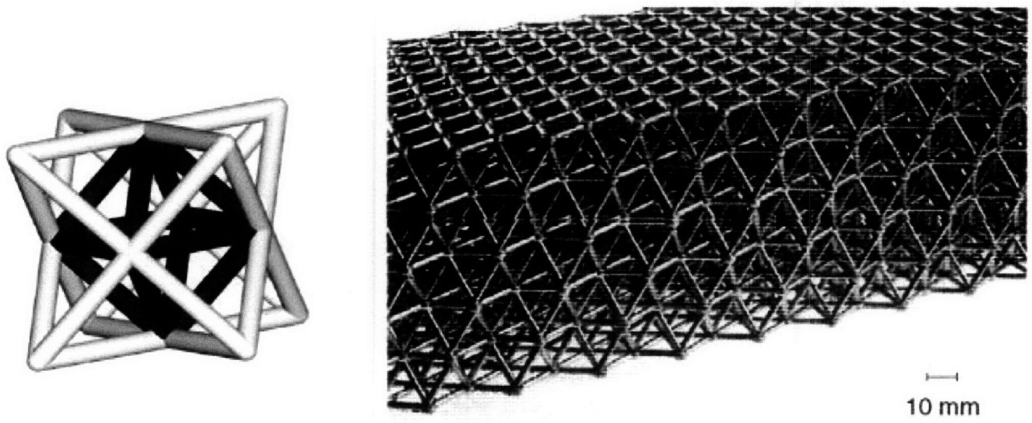

Figure 7-3. A unit structure of octet-truss lattice material with Maxwell's stability criterion (M) > 0 (left). Photograph of the octet-truss lattice material made from a casting aluminum alloy (Right).[1]

When the elastic limit is reached and the struts behave plastically in the plastic regime, the collapse stress also has the same correlation with the elastic modulus since the strut with the lowest collapse load determines the strength of the structure overall:

$$\frac{\sigma_{pl}}{\sigma_{y,s}} = \frac{1}{3}\frac{\rho}{\rho_s}. \tag{7-4}$$

When a lattice structure is made of a ceramic or other brittle material, it will collapse with struts starting to break. Following the same argument from above we anticipate a collapse stress σ_{cl} that scales as $\frac{\sigma_{cl}}{\sigma_{cl,s}} \propto \frac{\rho}{\rho_s}$. (7-5)

7.2 How to Make π Shift Phase Mask in Section 2.3.

Consider light passing through a transparent mask and diffracted orders of the beam at the interface[3] as depicted in Figure 7-4.

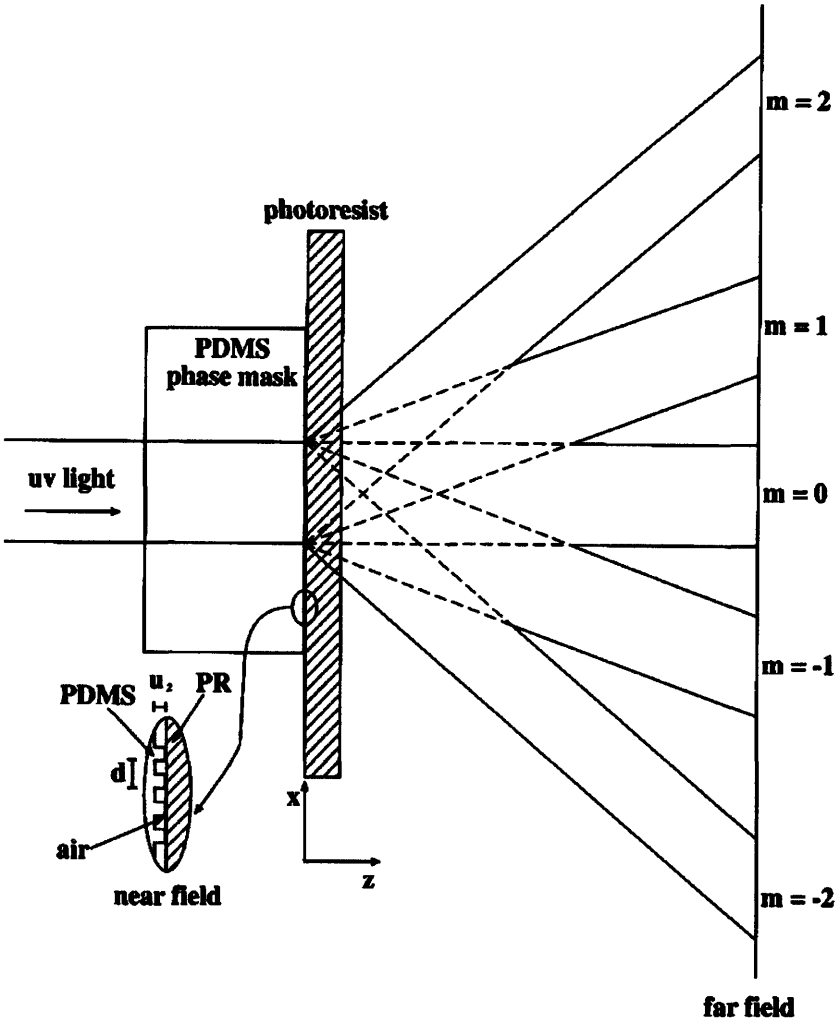

Figure 7-4. Geometry of an elastomeric phase mask, the photoresist, the light for exposure and qualitative definition of near field and far field. Schematic adapted from the journal paper of Rogers et al.[3]

From Figure 7-5, the refractive index is given as n_1 and the height as u_1 of the mask and those of air gap as n_2 and u_2, respectively. The phase, ϕ, of light with wavelength λ that emerges from the mask is related to the relief of the surface of the mask, $\Delta u = u_2$, and to the difference between mask's index of refraction and that of the

surroundings, $\Delta n = n_2 - n_1$, by Eq. (7-6).

$$\Delta\phi = \frac{2\pi}{\lambda}\Delta n \Delta u \tag{7-6}$$

The phase of light in the mask (ray 1) is $\phi_1 = \frac{2\pi}{\lambda} n_1(u_1 + u_2)$ and the phase of light crossing the air gap (ray 2) is $\phi_2 = \frac{2\pi}{\lambda}(n_1 u_1 + n_2 u_2)$. Thus, the phase difference is

$$\phi_2 - \phi_1 = \frac{2\pi}{\lambda}(n_1 u_1 + n_2 u_2 - n_1 u_1 - n_1 u_2) = \frac{2\pi}{\lambda}\Delta n u_2 . \tag{7-7}$$

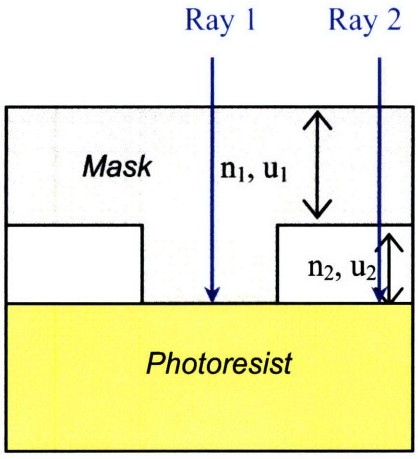

Figure 7-5. Enlarged image of cross-section of an elastomeric phase mask (light grey), a photoresist layer (light yellow) and in-between air gaps (white), showing the indices of refraction (n_1 and n_2), and the dimensions of the mask and air gaps (u_1 and u_2).

In order to make the phase shift equal to π, $\Delta\phi = \pi = \frac{2\pi}{\lambda}\Delta n u_2$, the height of the mask should be $u_2 = \frac{\lambda}{2\Delta n}$ as a design guide (for PDMS-air and λ=355nm, u_2= 395 nm). When the phase shift is π, the electric field undergoes abrupt changes in sign at the edges of the pattern in the mask, where the phase shift occurs. This change in sign generates the contrast of a structure in the photoresist with masks that manipulate only the phase of light.[3]

7.3 Gold Calibration of an Indenting Tip for AFM Nanoindentation in Section 2.4.

In AFM nanoindentation, measuring the radius of curvature of the indenting tip is essential to analyze the mechanical data as discussed in chapter 2-4. Before conducting force measurements, the dimension of the tip needs to be calibrated using gold nanoparticles.

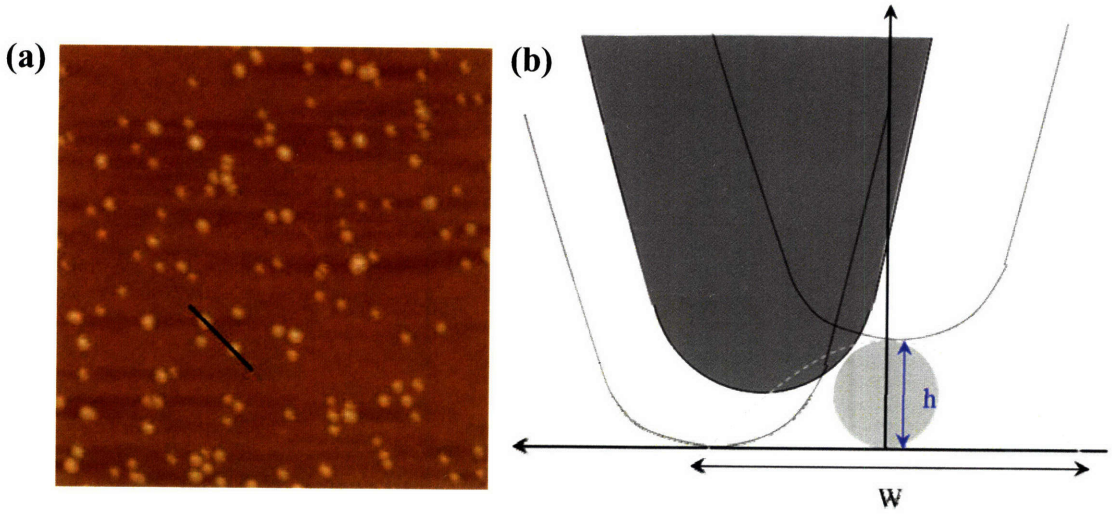

Figure 7-6. (a) AFM micrograph (1x1 μm^2) of gold nanoparticles and the black line utilized for measuring the height (h) and width (W) of a gold nanoparticle in the cross-sectional analysis. (b) Schematic sketch for tip radius evaluation with spherical estimation of tip-scanning the gold nanoparticle.

At first, a tip scans across the surface of gold nanoparticles adhered to the silicone substrate as shown in Figure 7-6 (a). In the Section analysis of the scan, we measure a width, W, and a height, h, in Figure 7-6 (b)[4] of the spherical gold nanoparticle. When a tip has a radius of curvature equal to R, in first approximation the profile of the tip and the particle is correlated[5, 6] by the relation $R = \frac{W^2}{8h}$.

7.4 References

1. Ashby, M. F., *Cellular Ceramics* (eds. Scheffler, M. andColombo, I. P.) (Wiley-VCH, 2005).
2. Gibson, L. J. and Ashby, M. F., *Cellular Solids: Structure and Properties* (Cambridge University Press, Cambridge, 1997).
3. Rogers, J. A., Paul, K. E., Jackman, R. J. and Whitesides, G. M., "Generating similar to 90 nanometer features using near-field contact-mode photolithography with an elastomeric phase mask". J. Vac. Sci. Technol. B **16**, 59-68 (1998).
4. Shulha, H., Kovalev, A., Myshkin, N. and Tsukruk, V. V., "Some aspects of AFM nanomechanical probing of surface polymer films". Eur. Polym. J. **40**, 949-956 (2004).
5. Bonanni, B. and Cannistraro, S., "Gold Nanoparticles on Modified Glass Surface as Height Calibration Standard for Atomic Force Microscopy Operating in Contact and Tapping Mode". J. of Nanotech. Online **1**, 1-14 (2005).
6. Vesenka, J., Manne, S., Giberson, R., Marsh, T. and Henderson, E., "Colloidal Gold Particles as an Incompressible Atomic-Force Microscope Imaging Standard for Assessing the Compressibility of Biomolecules". Biophys. J. **65**, 992-997 (1993).